



The
University
Of
Sheffield.

Simulation of lattice matched InAs/GaAs_{0.09}Sb_{0.91} Type II Superlattice Photodetectors

By:

Elizabeth Stark

A thesis submitted in partial fulfilment of the requirements for the degree of
Doctor of Philosophy

Submission Date

24th June 2021

Contents

Acknowledgements.....	5
List of publications	5
Abstract	7
List of symbols	9
1 Introduction.....	11
1.1 Quantum wells and superlattices.....	12
1.2 Photodiode Characteristics.....	18
1.3 Photodiodes significant in literature.....	19
1.4 Summary	27
1.5 Motivation.....	27
1.6 Thesis overview.....	28
2 Background theory.....	33
2.1 Wavefunctions and wavefunction overlap.....	33
2.2 Periodic boundaries.....	34
2.3 K.p theory.....	35
2.4 Optical absorption.....	37
2.5 Current density simulations.....	39
2.6 Temperature and bandgap relationship.....	42
2.7 PN and PIN photodiodes.....	43
2.8 Dark current in photodiodes.....	45
2.9 Barrier photodiodes current density behaviours.....	47
2.10 Infrared radiation.....	47
2.11 Summary	48
References.....	50
3 Simulation details and experimental methods.....	51
3.1 Nextnano++ superlattice structure definition	51
3.2 Nextnano++ current simulations.....	52
3.3 Optical calculations.....	54
3.4 Sample fabrication.....	55
3.5 Dark current measurements.....	60
3.6 Blackbody photoresponse measurements.....	61
References.....	64
4 Design of lattice-matched InAs/GaAs _{0.09} Sb _{0.91} type II superlattice photodetectors.....	65
4.1 Introduction.....	65
4.2 Model details and verification.....	66
4.3 Simulated Results.....	69

	4.4 Discussion.....	77
	4.5 Conclusions.....	79
	References.....	79
5	Temperature dependence of InAs/GaAs _{0.09} Sb _{0.91} superlattice cutoff wavelength and absorption coefficient simulations.....	81
	5.1 Introduction.....	81
	5.2 Model Validation.....	81
	5.3 Temperature dependence of cutoff wavelength simulation	83
	5.4 Conclusions.....	94
	Reference.....	95
6	Temperature dependence of bandgap and current density simulations.....	97
	6.1 Introduction.....	97
	6.2 Current density model validation.....	98
	6.3 Current density results.....	105
	6.4 Comparing InAs/GaAsSb superlattices with the same cutoff wavelength at 77 K.....	111
	6.5 Conclusion.....	117
	References.....	118
7	Fabrication and blackbody response of InAs/GaAsSb superlattice	119
	7.1 Introduction.....	119
	7.2 Wafer details.....	120
	7.3 XRD simulations of wafer SF1625	124
	7.4 Low Temperature current voltage measurements	126
	7.5 Blackbody emitter photoresponse	129
	7.6 Conclusion.....	132
	References.....	134
8	Conclusions and future plans	135
	8.1 Conclusions.....	135
	8.2 Future plans.....	137
	References.....	140
	Appendix A- The parameters used in nextnano++ simulations.....	143
	Appendix B- The parameter script used in nextnano++ simulations	144

Acknowledgements

I would like to express my thanks to Prof. Chee Hing Tan for supervising and supporting me throughout my PhD. I truly appreciate your advice and guidance throughout my studies. I would also like to thank Prof. Jo Shien Ng and all the members of the advance detector centre group past and present, especially Dr Vladimir Shylak, Dr Leh Woon Lim and Mr Jonathan Taylor-Mew for their help and advice on the fabrication of the samples in this thesis. Special thanks is given to Dr Jon Petticrew for reading the many drafts of this thesis and helping this dyslexic's writing make sense to other people.

I would like to express my gratitude to Chris Maxey from Leonardo for giving this work industrial relevance, and funding this project. A studentship from the EPSRC and CASE funding has also been gratefully received.

This work would not have been possible without the National III-V Centre, with a special thanks to Dr. Edmund Clarke and Dr Pallavi Patil for growing the wafers in this thesis, and also Dr. Rob Airy and Saurabh Kumar for fabrication advice and training.

I also need to express thanks to Dr Stefan Biner and the rest of the team at nextnano for their help and advice on the simulations in this thesis.

My final thanks are to my friends, family for their support during my PhD and the members of 5th Sheffield Guide Unit for keeping me grounded.

List of Publications

Poster presentations:

E. Stark, B. White, and C. H. Tan, "Evaluation of cut-off wavelength of lattice matched InAs/GaAs_{0.09}Sb_{0.91} type II superlattices" poster presentation *UK compound semiconductors conference*, Sheffield, UK, July 2019.

Journal Presentation:

E. Stark, and C. H. Tan "An evaluation of the cut-off wavelength of lattice matched InAs/GaAs_{0.09}Sb_{0.91} type II superlattices in the MWIR, LWIR, and VWIR." manuscript in preparation for submission."

Abstract

Type II superlattices (T2SL) are important as an alternative to Mercury cadmium telluride (MCT) photodetectors. MCTs offer some of the best performance figures, but are restricted in use due to cost, and the phasing out of Mercury containing products in the EU from 2017. T2SLs have several advantages over MCTs including cheaper lattice matched substrates, less sensitive structure composition and reduced auger recombination. InAs/GaAs_{0.09}Sb_{0.91} T2SLs are lattice matched, resulting in photodiodes grown with fewer defects in the crystal structure. In this thesis the cutoff wavelength, absorption coefficient and current-density of InAs/GaAs_{0.09}Sb_{0.91} superlattices were simulated using the program nextnano++. Models were used first were validated by benchmarking against published results. Simulations of a wide range of T2SL structures were performed to identify the design parameters that controls the cutoff wavelengths, absorption coefficients and dark current densities. This offers the opportunity to choose the best structure for the desired wavelengths before growth and fabrication, which incurred high cost.

Simulations showed, nextnano++ could produce excellent agreement to measured cutoff wavelengths (λ_c) of InAs/GaAs_{0.09}Sb_{0.91} T2SLs in the mid wavelength infrared (MWIR), long wavelength Infrared (LWIR) and very long wavelength infrared (VLWIR). The InAs/GaAs_{0.09}Sb_{0.91} T2SLs simulations achieved the LWIR and VLWIR ranges with superlattice quantum well (InAs) thickness between 12 -20 monolayers (MLs). The simulations indicated the cutoff wavelength of the superlattice had a greater dependence on the thickness of the InAs well. For example using a fixed 7 ML InAs as the quantum well, changing the GaAsSb barrier thickness from 7 to 20 ML, only resulted in λ_c changing from 4.64 to 4.7 μm at 77 K. On the other hand, for a fixed 7 ML of GaAsSb barrier, changing the InAs well from 7 to 20 ML shifted λ_c from 4.64 to 10.5 μm at 77 K. Simulations of absorption coefficient for InAs/GaAs_{0.09}Sb_{0.91} T2SLs at multiple temperatures showed that more symmetrical superlattice periods had higher absorption coefficients at all the temperatures simulated.

The temperature dependence of λ_c and absorption coefficients was simulated in a wide range of T2SL designs. The results show stronger temperature dependence of these parameters when the thickness of InAs is changed. The change in λ_c is stronger in designs with a longer λ_c . For instance in a VLWIR design with 20ML InAs/20 ML GaAsSb λ_c increases from 18.5 μm at 77 K to 35.0 μm at 300 K. In a MWIR design with 7 ML InAs/7 ML GaAsSb λ_c only increases marginally from 4.6 to 5.7 μm over the same temperature range. When different designs with similar cutoff wavelengths are compared, the temperature dependence behaviours are similar. However, T2SL designs with a more symmetrical design shows higher absorption coefficients across all

temperatures simulated. A 16ML InAs/10 ML GaAsSb T2SL show higher absorption coefficients than a 20 ML InAs/7 ML GaAsSb T2SL, although they have similar λ_c . The temperature dependence of dark current was also investigated.

Finally an LWIR InAs/GaAs_{0.09}Sb_{0.91} PIN structure with a superlattice i-region and bulk p and n-regions to act as barriers was fabricated. Simulations suggested the sample had a cutoff wavelength at 9.5 μm whereas the photo response from the blackbody emitter indicated that the peak photoresponse signal is at 9-11 μm .

List of symbols

A - holes concentrations	$i_{n\ total}$ - total device noise
A_D - device area	$I(phot)$ - is the photocurrent of the device
α - absorption coefficient	IPA- isopropyl alcohol
α_g – Varshni bandgap equation empirical constant	J_n - electron current density
b- Wien's displacement constant (2.898×10^{-3} m K).	k_b -Boltzmann's constant
β_g – Varshni bandgap equation empirical constant	λ – Wavelength
D- Electron carrier concentration	λ_c – Cut-off Wavelength
c - Speed of light in a vacuum (3×10^8 ms ⁻¹)	L_A - hole minority carrier diffusion length
CBIRD-Complimentary barrier infrared photodiode	L_D - electron minority carrier diffusion length
CB-Conduction band	LH- Light hole band
D*- Specific detectivity	L_w - Width of the quantum well
D_A - hole diffusion coefficient	LWIR - Long Wavelength Infrared
D_D - electron diffusion coefficient	m^* -charge carrier Effective mass
E - applied electric field (Vcm ⁻¹)	m is the mass of the particle
E1 -first energy level in conduction band	MCT –Mercury Cadmium Telluride
ϵ - dielectric constant	ML- Monolayers
E_g - bandgap	μ_n - mobility of electrons
E_{photon} - photon energy	MWIR- Mid-wavelength Infrared
E_n - Quantum confinement energy	η – Quantum efficiency
E_{th} – Threshold energy	n - Carrier density
Δf - change in bandwidth	η_f -ideality factor,
FPA- focal plane array	n_p - Primary quantum number
G_{rad} -electron generation rate	n_i - intrinsic carrier concentration
h - Planck's constant (6.626×10^{-34} Js)	n_0 - equilibrium electron carrier density
\hbar - reduced Planck's constant (1.0546×10^{-34} Js)	Δn – non-equilibrium electron carrier densities
\hat{H} - Hamiltonian operator	N_D^+ - donor ionisation concentration
HH -heavy hole band	N_A^- - acceptor ionisation concentration
I_0 -saturation current,	N_D, N_A -impurity concentrations for donors and acceptors
	P- Probability
	p -momentum of the particle

p_0 - equilibrium hole carrier density
 p (*optical*)- incoming light optical power
 ψ -wavefunction
 q - electron charge,
 Q -incident photon flux
 QDIP-Quantum dot infrared photodetectors
 QE- Quantum efficiency
 r - Reflectivity
 R_s is the contact resistance,
 R - is the measured responsivity
 R_{max} -maximum theoretical responsivity
 R_0A - Resistance area product at 0V
 σ - Stefan-Boltzmann constant
 (5.6704x10⁻⁸ Wm⁻²K⁻⁴)
 SWIR- Short Wavelength Infrared

T -is the temperature.
 T_{BB} -Blackbody temperature
 T2SL - Type II Superlattice
 τ_{A1} –auger mechanism 1 carrier lifetime
 τ_{A1}^i –intrinsic material lifetime auger
 mechanism 1
 τ_{A7} –auger 7 mechanism carrier lifetime
 τ_{A7}^i –intrinsic material auger lifetime
 mechanism 7
 ϕ_B – Total background photon flux
 ϕ -electrostatic potential
 $u_{n,k}(x)$ -periodicity of the crystal
 V - potential
 VLWIR - Very Long Wavelength Infrared
 U_{srh} - total recombination rate

1 Introduction

Photodetectors are often made from semiconductor material. They convert light into electrical current, referred to as photocurrent. This is achieved by taking advantage of the photoelectric effect. Light is made of particles, called photons, which have discrete energy (E_{photon}) of,

$$E_{\text{photon}} = \frac{hc}{\lambda} \quad (1.1)$$

where h is Planck's constant (6.626×10^{-34} Js), c is the speed of light in a vacuum (3×10^8 ms⁻¹), and λ is the wavelength of the light. A photocurrent is induced when electrons in the valence band are excited by the light into the conduction band. The bandgap, E_g , of the material is the energy difference between the highest occupied energy state in the valence band and the lowest unoccupied energy state in the conduction band. The E_g for semiconductors is smaller than the E_g for insulators and larger than the E_g of metals. The wavelength of light a photodetector responds to depends on E_g . Only photons with energy greater than E_g can excite an electron from the valence band into the conduction band. E_g corresponds to the high cutoff wavelength, λ_c represents the longest wavelength that can be absorbed and is defined by,

$$\lambda_c = \frac{hc}{E_g} . \quad (1.2)$$

The bandgaps of semiconductors are smaller than insulators and larger than metals. Semiconductor bandgaps are small enough that a single infrared photon can give carriers enough energy to promote the carrier into the conduction band. Binary semiconductor compounds are commonly made from a group III element and a group V element. The smallest bulk binary III-V material is InSb is 0.18 eV [1] this corresponds to a cutoff wavelength of 6.89 μm which is just inside the long wavelength infrared (LWIR) range. This means that photodiodes operating in the longer wavelength range need to be made from non-binary semiconductors or use nano structures to create smaller bandgap photodiodes. Pure semiconductors are called intrinsic, adding impurities (dopants) to semiconductors change the electrical properties. Semiconductors with dopants are called extrinsic semiconductors. Photodiodes can operate at several different wavelengths of light which is dictated by the material the semiconductor is made from, the dopants added to the material and any nanostructures that are included. Photodiodes are typically categorised by their operating wavelengths as seen in Table 1.1.

Table 1.1: The operating wavelength regions for optical detectors and the common applications

Operating Wavelengths (μm)	Name	Abbreviation	Common application
1-3	Short Wavelength Infrared	SWIR	Long distance communications [2]
3-5	Mid-wavelength Infrared	MWIR	Medical sensing, gas and chemical detection [3,4]
6-14	Long Wavelength Infrared	LWIR	Thermal imaging, gas detection [5]
>14	Very Long Wavelength Infrared	VLWIR	Spectroscopy, thermal imaging, astronomy [6]

Short Wavelength Infrared (SWIR) photodiodes are mainly used in long distance optical communications [2]. Mid-Wavelength Infrared (MWIR) photodiodes have many applications such as: gas and chemical detection [3], and uses in medical sensing [4]. Long Wavelength Infrared (LWIR) photodiodes have many uses including, gas detection, spectroscopy, and thermal imaging. LWIR is particularly suited to thermal imaging of humans and animals due to the strong water peak between 8-9 μm [7,8]. The Very Long Wavelength Infrared (VLWIR) can be used for many of the same uses as the other wavelength ranges. The VLWIR has further uses in astronomy [6], where signals from distant galaxies are shifted into VLWIR due to the Doppler effect of the expanding universe. Water has strong absorption peaks in VLWIR at 15 μm , 20 μm [7], which correspond to the rotation of hydrogen around the oxygen molecule [8]. Hence VLWIR can be used to measure water vapour in planetary atmospheres [9].

1.1 Quantum Wells and Superlattices

As the longest cutoff wavelength for bulk binary III-V semiconductors is 6.89 μm non bulk structures are used to achieve longer wavelengths. Quantum wells are heterostructures made from a smaller E_g material, the well material, surrounded by a larger E_g semiconductor material, the barrier material. QW infrared photodiodes (QWIPs) were first reported in 1987 [10]. One of the most common uses of QWIPs is in focal plane arrays (FPAs) for use in thermal imaging [11]. A quantum well detector has a quantum confinement in one direction.

This confinement causes the quantum well to have discrete energy levels, as depicted in Figure 1.1. The transitions between the discrete energy levels fall into 2 main categories intraband and interband transitions. Intraband transitions are transitions between energy levels inside the same band (e.g. inside the conduction band) while interband transitions are transitions between energy levels in different bands (e.g. transitions from the valence band to the conduction band) shown in Figure 1.1.

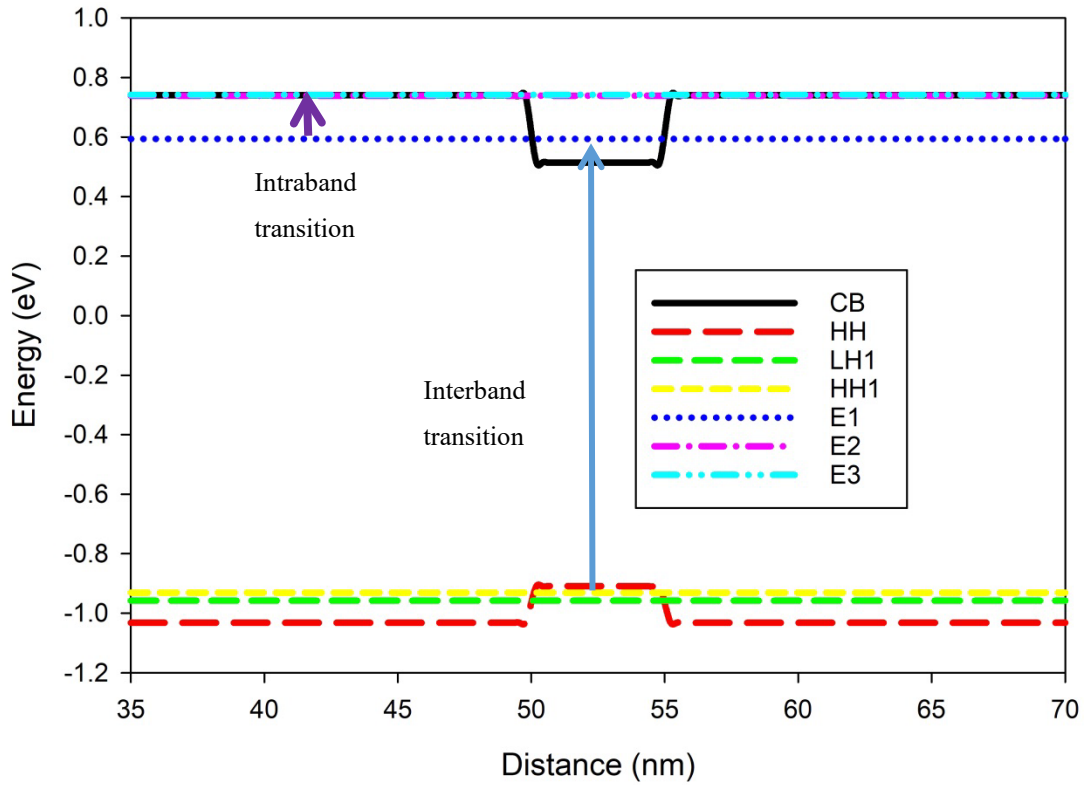


Figure 1.1: A Band structure diagram for a Quantum Well. The red dashed line shows the valence band and the black solid line shows the conduction band. The blue arrow depicts an interband transition which is a transition between energy levels in different bands. The purple arrow depicts an intraband transition, which is a transition between energy levels inside the same band, e.g. inside the conduction band.

The energies of the electrons in a quantum well with infinite barriers can be approximated using the quantum confinement energy, E_n , equation below,

$$E_n = \frac{\hbar^2}{2m^*} \left(\frac{n_p \pi}{L_w} \right)^2 \quad (1.3)$$

where m^* is the effective mass of the charge carrier, L_w is the width of the quantum well, n_p is the primary quantum number and \hbar is the reduced Planck's constant (1.0546×10^{-34} Js). There are fixed energy levels in finite quantum wells. If the well is widened the energy levels decrease thus the quantum well energy levels can be engineered by adjusting the thickness of the materials.

Wavefunctions are equations used to describe the state of the electron in the well. The square of the wavefunction gives the probability of the position of an electron in a specific energy level. Figure 1.2 depicts two multi quantum well structures. Figure 1.2(a) shows the squared wavefunctions for the first three heavy hole and the first two electron energy levels inside a structure with large barriers isolating the wells. Figure 1.2 (b) shows the first three heavy hole and

the first three electron energy levels and squared wavefunctions for a structure with narrow barriers. The squared wavefunctions have been shifted to line up with the energy of the corresponding energy level. For the structure with large barriers (figure 1.2 (a)) the electron energy levels are very spread out and the heavy hole energy levels are very distinct and separate. From the square wavefunctions it can be seen that the wavefunctions do not leak through the barriers to affect each other. Whereas for the structure with small barriers (figure 1.2(b)) the wavefunctions decay into the neighbouring wells affecting the energy levels, leading the structure to act as a superlattice rather than isolated quantum wells. The wavefunctions for the holes behave similarly, as the wells can be thought of as barriers for the holes. The hole energy levels are also very close together and are acting like a small band of levels at a similar energy or a miniband.

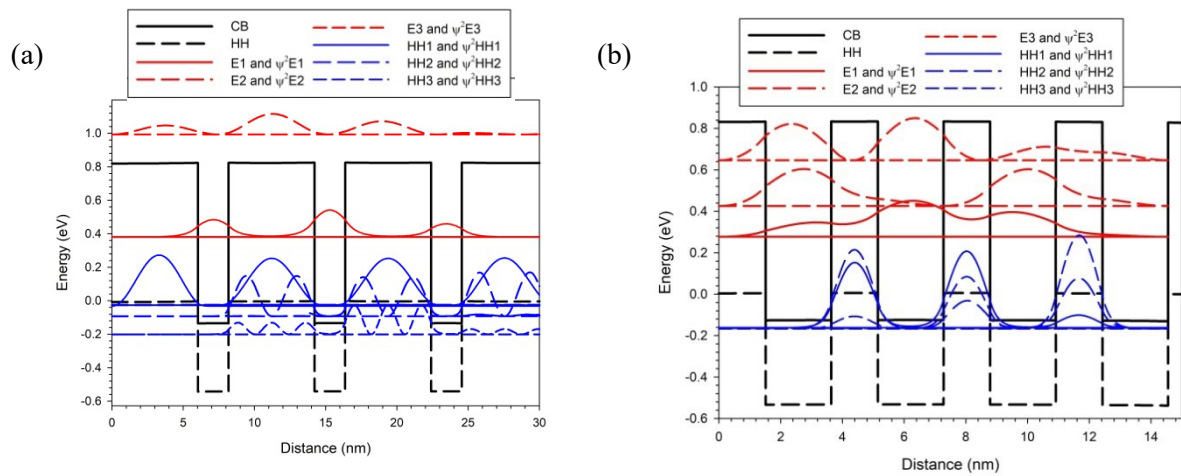


Figure 1.2: The hole squared wavefunctions (HH1, HH2, HH3, HH4) and the electron squared wavefunctions (E1, E2, E3), plotted with the band edges for the conduction, and heavy hole bands (CB, HH), for (1.2 (a)) a multiple quantum well structure with 7 ML wells and 20 ML barriers, and (1.2 (b)) A multiple quantum well structure with 7 ML wells and 5 ML barriers.

Superlattices are quantum wells with thin barriers and repeated many times. The layers in superlattices are thin enough that the wavefunctions leak through the barrier enabling interactions between neighbouring wells as seen in figure 1.2. These interactions lead to the creation of minibands, minibands are made up of many energy levels that are close together combining to form one large “band” of energies. The interband transition between the minibands determines the E_g of the photodiode.

Typical superlattices, have between 50 to 200 quantum wells [12,13], however recently larger structures have been grown with over 300 periods [14]. In this thesis a superlattice period is defined as the combined thickness of the well and the barrier together. The key difference between isolated quantum wells and superlattices is the barrier width between the quantum wells.

There are 3 types of superlattice Type I, Type II and Type III. Type I superlattices contain a small E_g material like InAs (E_g 0.35 eV [15]) and a much larger E_g material like AlSb (E_g 1.62 eV [15]). The holes and electrons are confined to the smaller E_g material. This means the E_g of the superlattice strongly depends on the E_g of the well material. For example in an InAs/AlSb superlattice the smallest energy transition is inside InAs.

Type II superlattices (T2SL) are made in two different band geometries, staggered and misaligned. Both forms of T2SL depend on the well and barrier materials widths for its E_g . This is due to the top of the valence band and the bottom of the conduction band being in different material layers. In misaligned T2SL, the separation is caused by the valence band in the well material being lower than the conduction band in the barrier material. This leaves a gap in the bandgap geometries which can be seen in Figure 1.3 (type II misaligned). Whereas in staggered T2SL the top of the valence band in the well material is above the top of the conduction band in the other material causing an overlap seen in Figure 1.3 (type II staggered). The separation of the valence and conduction bands into opposite layers also separates the electrons and holes. This results in the T2SL E_g being sensitive to the thickness of both the well and barrier layers, this means that E_g can be tailored by altering the width of the wells or/and barriers in the superlattice [13]. The E_g can be small depending on the superlattice, meaning that T2SL photodiodes are useful for long wavelength photodiodes as the energy of these transitions are small.

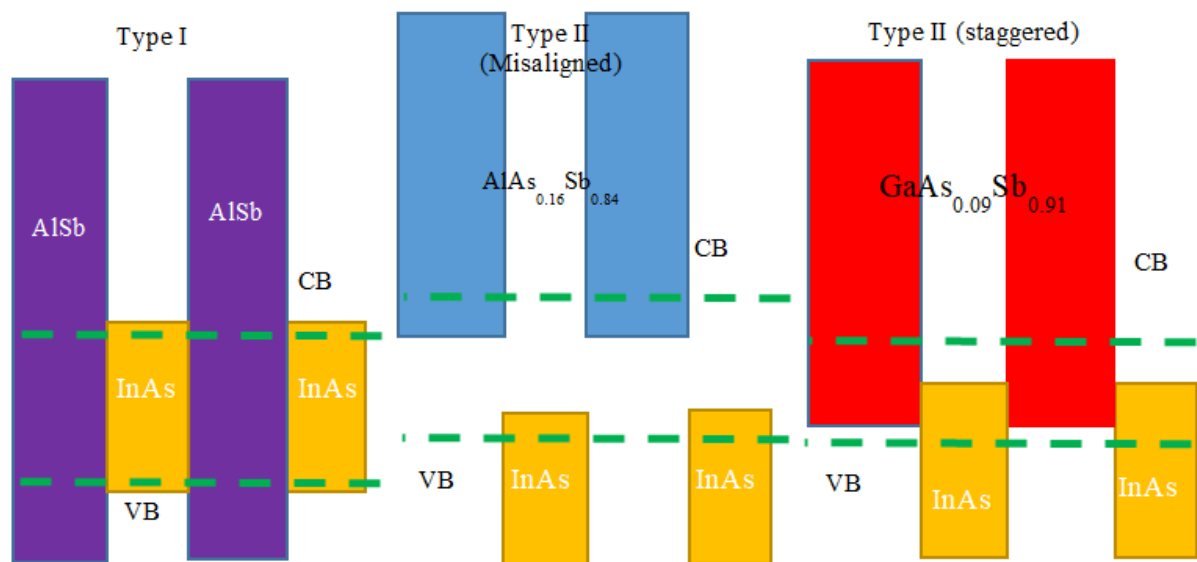


Figure 1.3: The Band structures for the three main types of superlattice. The green lines represent the effective conduction band (CB) and the effective valence band (VB). In Type I the electrons and holes are both confined in the well material (InAs). In both type II bandgap alignments the electrons and holes are spatially separated, electrons are confined in the well material (InAs) while the holes are confined in the barrier material (AlAs_{0.16}Sb_{0.84} and GaAs_{0.09}Sb_{0.91})

The final type of superlattices is Type III, which will only be briefly mentioned as they cannot be formed by III-V compounds. These structures are formed using a semiconductor like CdTe and a semiconductor that behaves like a semimetal (HgTe). Semimetals have no E_g , the conduction band and valence band are touching or have an overlap.

1.1.1 Auger recombination

An attractive characteristic of T2SL is the theoretical suppression of Auger recombination. Auger recombination takes place when conduction band electrons recombine with holes in the valence band. The energy released from this recombination is given to an electron (or hole) which is then promoted to a higher electronic state. The energy is released as a phonon and the electron returns into a lower energy state. Auger recombination has strong dependencies on both E_g and temperature. It is expected to be significant in small E_g devices such as LWIR and VLWIR photodiodes, as the smaller E_g means the energy needed for Auger recombination to occur is also smaller. In T2SL the spatial separation of the holes and electrons suppresses Auger recombination mechanism 1 (Figure 1.4 (a)) as momentum is not conserved, reducing the probability of occurring. In strained T2SL the differing lattice constants cause a split in the degeneracy of the light hole band and the heavy hole band, which suppresses Auger mechanism 7 (Figure 1.4 b) as it uses both hole bands. In the absence of generation-recombination and diffusion currents, Auger recombination is one of the main contributors to dark currents [16]. By separating the hole bands the Auger 7 mechanism has a higher activation energy, reducing the probability of occurring [17]. The Auger 1 mechanism determines the carrier lifetime for narrow E_g materials. Carrier recombination lifetime represents the average time between a carrier being generated and the carrier recombination. A structure with longer carrier recombination lifetimes is desirable, longer carrier lifetime means there is less generation-recombination dark current. Auger 1 recombination for an electron is seen in Figure 1.4 (a), Auger 1 recombination is dominant in n-type material. Auger 7 recombination is dominant in p-type material, the mechanism is seen in Figure 1.4 (b).

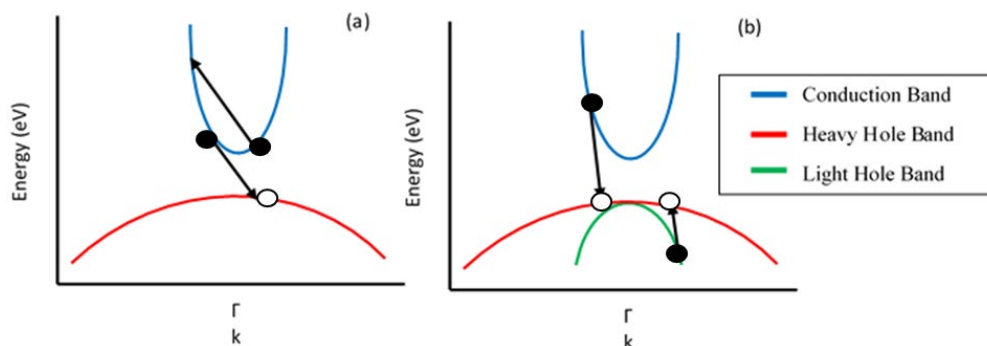


Figure 1.4: Diagrams of Auger 1 (a), and Auger 7 (b) recombination mechanisms. The holes are represented by the white circles and the electrons are depicted by the black circle

1.1.2 Superlattice photodiodes in literature

Since they were first introduced in 1977 [18], T2SL photodiodes have been gaining interest, as an alternative to Mercury Cadmium Telluride (MCT) detectors. There are increasing restrictions on the uses of mercury and cadmium in products used and sold in the EU [19], due to their environmental effects [20]. So finding material systems that are potentially equivalent or better than MCT for photodetectors is increasingly important.

InAs/GaSb superlattices are seen as a promising alternative to MCT detectors [21,22]. InAs/GaSb T2SL structures are lattice mismatched to GaSb. The strained superlattices can achieve a wide range of E_g due to the engineering of the type II band alignment. A thin layer of InSb is often grown at the InAs/GaSb interfaces to help balance the strain of the superlattice [23]. InAs/GaInSb is another lattice mismatched system. The lattice mismatching causes the suppression of Auger recombination and tunnelling currents. This suppression results in improvements in the Auger limited minority carrier lifetimes [22]. InAs/GaInSb superlattices E_g can be engineered for the LWIR and VLWIR, the early results for InAs/GaInSb is T2SL were in the LWIR. One of the first reported results was in 1996, this device achieved a quantum efficiency of 20 % at 7 μm [24]. Modelling of VLWIR on structures with InAs/Ga_{0.9}In_{0.1}Sb and InAs/Ga_{0.75}In_{0.25}Sb showed that higher Indium content was favourable [25]. The InAs/Ga_{0.75}In_{0.25}Sb superlattice had a carrier lifetime of 140 ns compared to 5 ns seconds for a superlattice of InAs/ Ga_{0.9}In_{0.1}Sb. This is due to the larger strain in InAs/Ga_{0.75}In_{0.25}Sb causing a larger splitting between the heavy hole and light hole valence band.

1.1.3 MCT comparisons to superlattices

MCT is the most developed photodiode material for the LWIR and the one which III-V photodiodes are compared against. The first MCT photodiodes were developed in 1962 [26,27], the large detection range of MCT, 0.2 μm to 25 μm , led to MCT photodiodes being common, and commercially available [28]. One disadvantage to MCT photodetectors is the high level of precision needed in MCT growth. A small fluctuation in the composition of a MCT photodiode has a larger change in the cutoff wavelength than a similar fluctuation in the composition of a T2SL photodiode [29]. This issue is particularly significant in VLWIR detectors. A further disadvantage is the strict management controls required, due to the toxic nature of MCT processing, making it unsuitable for large-scale manufacturing. Manufacturing, and operation, are also limited to low temperatures as mercury dissociates at room temperature. (250 K is considered high operating temperature for MCT [30].)

1.2 Photodiode characteristics

There are several different characteristics that can be used to analyse the quality of photodiodes. This section contains explanations of the different photodiode characteristics and how those properties are calculated.

1.2.1 Quantum efficiency

Quantum efficiency (QE) is used as an indicator of photodiode quality. The definition of QE used in this work is the fraction of incoming photons that are converted into detected signal. QE (η) is defined by the equation,

$$\eta = \frac{R_{esp}}{R_{max}} \quad (1.4)$$

where R_{esp} is the measured responsivity and R_{max} is maximum theoretical responsivity. Responsivity compares the amount of electrical current a detector outputs compared to the optical power that is input. Responsivity has the units AW^{-1} and is defined as,

$$R_{esp} = \frac{I(pht)}{p(optical)} \quad (1.5)$$

where $I(pht)$ is the photocurrent of the device and $p(optical)$ is the optical power of the incoming light. The maximum responsivity has the units AW^{-1} , and is defined as,

$$R_{max} = \frac{\lambda}{1.24(\mu\text{m } \text{WA}^{-1})} \quad (1.6)$$

where λ is the wavelength of the incoming light in micrometres.

Figure 1.6 shows the QE of a MCT photodiode (the solid line) compared superlattice structures shown by the symbols [13,31, 43]. InAs/GaAsSb superlattices are represented by the stars, InAs/GaSb the circles and InAs/InAsSb are represented by the squares. As can be seen in Figure 1.6 several of the superlattice photodiodes achieve performance within 10 % of the MCT QE. However, further research is needed to further improve superlattice photodiodes quantum efficiency to challenge the more mature MCT material system.

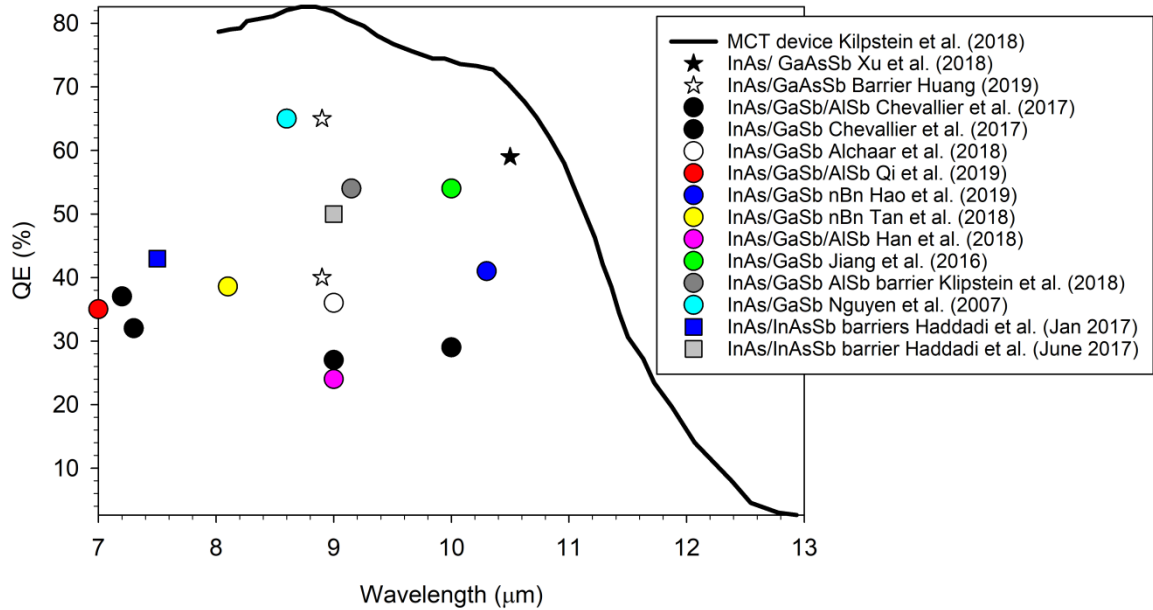


Figure 1.5 The Quantum efficiency of a LWIR MCT photodiode plotted against Wavelength in comparison to LWIR III-V T2SL photodiodes [13, 31-43]

1.3 Photodiodes significant in literature

1.3.1 Rule 07

Rule 07 is an extrapolated rule, created in 2007, predicting the behaviour of MCT photodiodes [44,45]. Figure 1.7 shows dark current predictions of rule 07 compared to different superlattice dark currents. The graph includes InAs/GaSb photodiodes [13,32,36,37,38,46,47,48], InAs/GaAsSb T2SL photodiodes [32] and structures containing barriers [31,34,39,43,49]. There are several superlattice photodiodes with current densities less than MCT, many of these structures (depicted by a square symbol) include barriers in the design. Barriers reduce charge carrier flow in one direction. This will be expanded on later in section 1.4.5. Several of lower current density photodiodes are InAs/GaAsSb superlattice structures which will be investigated further in the results chapters in this thesis.

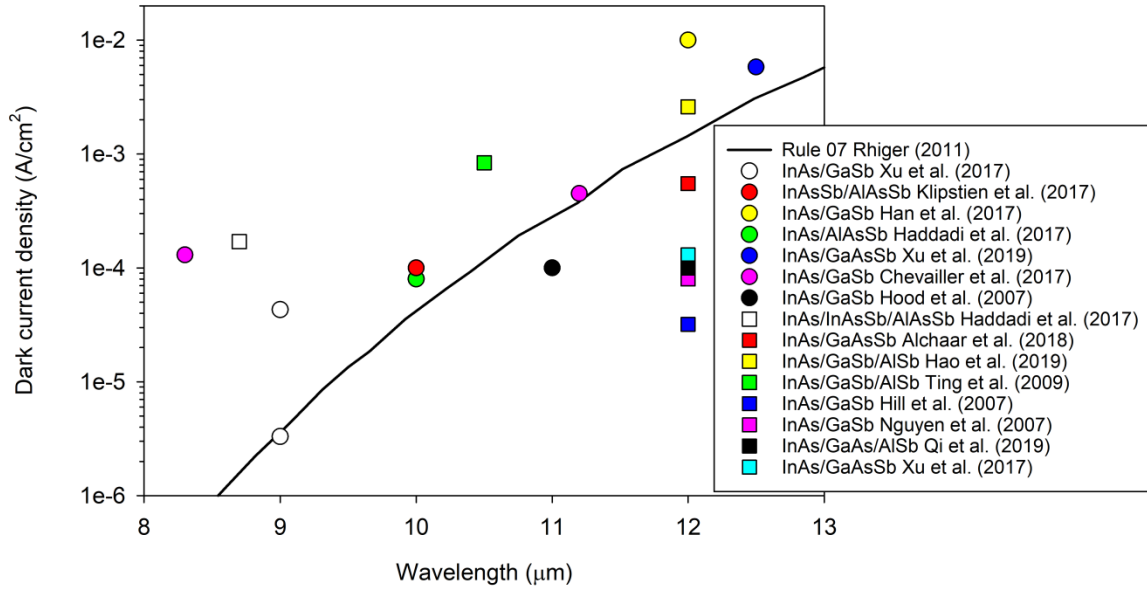


Figure 1.6: Dark current density Rule 07 plotted against Wavelength for comparison to T2SLs III-V dark current density [13, 31, 32, 34,36-38,40,42-49]

1.3.2 InAs/GaSb superlattice photodiodes

InAs/GaSb superlattices are one of the most common T2SL photodiode structures. The InAs/GaSb superlattice system is a strained superlattice due to the materials' different lattice constants. Strained superlattices have the benefit of suppressing the Auger mechanisms as described section 1.1.1. Experimental evidence of the theoretical Auger recombination suppression has not been demonstrated, though this could be due to the poor quality of current photodiodes [50]. The strained superlattice leads to a wide range of E_g . Significant InAs/GaSb superlattices photodiode papers are summarised in Table 1.2.

Table 1.2: Summary table of key InAs/GaSb papers and their key properties at 77 K

Paper	Bias (mV)	Wavelength (μm)	Dark Current density (Acm^{-2})	Quantum efficiency (%)	Responsivity (AW^{-1})	Resistance Area (Ωcm^2)	Detectivity ($\text{cm}\cdot\text{Hz}^{1/2}\text{W}^{-1}$)	Reference
A	0	15 18	1.1×10^{-6}	66 45				[41]
B	110	12						[51]
C	0	14.5	5×10^{-7}	41				[52]
D		8.1			3.95			[39]
E	-50 +100	7.3 10.5					4.5×10^{10} 1.3×10^{10}	[34]
F	20	8.5	9.9×10^{-6}		1.5	1.4×10^4		[53]

Paper A which is summarised in Table 1.2 reports one of the best QE for VLWIR photodiodes. For comparison a typically reported QE is about 35 % [54] and the value reported in paper A is nearly double. The QE was measured at 15 μm , but the cutoff wavelength of the device is 21 μm this causes the responsivity to be high and gives a larger than typical QE. The current density for the device is $1.1\times 10^{-6}\text{ Acm}^{-2}$ at 77 K and at 0 V this is higher than expected for a structure with a barrier included. The structure of the device was 17 ML InAs/8 ML GaSb. The structure has a 1.6 ML InSb interface between the InAs and GaSb layers to balance the strain in the superlattice. Balancing strain reduces defects such as dislocations in the material, improving the crystal quality.

The photodiode in row B of Table 1.2 has a 17 ML InAs/7 ML GaSb superlattice structure similar to paper A. The QE quoted at 12 μm is lower than the paper in row A. This is mostly due to the structure not having any interface between the InAs and GaSb layers to balance the strain in the structures, but is higher than expected for the LWIR.

The paper listed in C of Table 1.2 lists a very low current density for the LWIR. The paper has a dual colour photodiode operating in the LWIR and the VLWIR [52] suggests that the lower than typical current density is partly due to the very high crystal growth quality of the superlattice.

The device in row D of Table 1.2 is a PIBN design, the structure of this device can be seen in Table 1.3. The barrier (B) region in PIBN is an M barrier; M barriers are explained in section 1.3.5.2. The importance of this structure is the operating temperature, 110 K, which is 30 K higher than typical LWIR measurements, and room temperature operation is a key target for

LWIR photodetectors. The responsivity reported of this device is at 80 K and is also high for InAs/GaSb superlattices devices.

Table 1.3: The design details of the wafer in the D of Table 1.2[39]

	Thickness (nm)	Doping (cm⁻³)	Superlattice period (ML)
P-region	600	1x10 ¹⁸	8/11 InAs/GaSb
I region	2200	p doped 1x10 ¹⁵	13/8 InAs/GaSb
B (barrier) region	500	2x10 ¹⁵	18/3/5/3 InAs/GaSb/AlSb/GaSb
N-region	500	2x10 ¹⁸	18/3/5/3 InAs/GaSb/AlSb/GaSb

The paper summarised in row E of Table 1.2 is about a dual colour detector that reacts in the LWIR and the VLWIR. The LWIR part of the device has an absorption region of 2 μm and a period of 11 ML InAs/7 ML GaSb. Whereas the VLWIR section of the device has a superlattice structure of 13 ML InAs/7 ML GaSb. This paper is of note as it has one of the best directivities for this material structure, most likely due to the small size of the photodiode (12x12 μm^2) and the polishing wet etch. The polishing etch used in the fabrication of the photodiode helps smooth the surface of the photodiode reducing the surface leakage of the photodiode, which improves the dark current of the photodiode. Specific detectivity (D^*) is calculated from the responsivity and the noise of a detector. Noise is a signal that masks the photocurrent and determines the minimum measurable signal of the device. It is an indicator of the signal to noise ratio of the detector calculating the amount of power input into the detector against the internal noise.

The equation for specific detectivity is,

$$D^* = \frac{R_{max}\sqrt{(A_D)\Delta f}}{i_{n\ total}} \quad (1.7)$$

where R_{max} is the maximum responsivity, (A_D) is the area of the device, Δf is the change in bandwidth (the range of frequencies the measurements covered), $i_{n\ total}$ is the total noise of the device.

The paper in row F of Table 1.2 has a complimentary barrier structure with an electron barrier of the same superlattice material system but a different period of the structure. Complimentary barrier structures are explained in section 1.3.5.3. This paper has a good resistance product area at 0 V (R_0A) for this material system and the LWIR.

1.3.3 InAs/GaAsSb superlattices

InAs/GaAsSb is a lattice matched material system that can potentially produce photodiodes grown with fewer defects, such as dislocations. Dislocations are caused by bonds breaking when lattice mismatched materials are grown on one another. As illustrated in Figure 1.8 the lattice constant varies depending on the semiconductor material, which affects the E_g . Fabrication of high quality photodiodes requires grown wafers to have high crystal quality. Therefore where possible lattice matched material systems are preferable to achieve the highest quality semiconductor crystal.

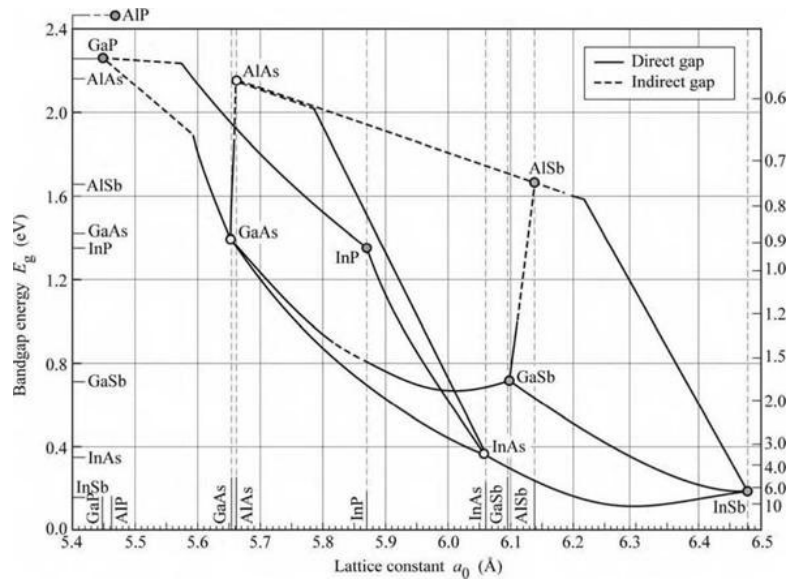


Figure 1.7: A Graph of the E_g of III-V semiconductors against the lattice constant [55].

InAs/GaAsSb superlattices have been gaining interest even though the absorption coefficient is typically lower than InAs/GaSb superlattices [56]. The absorption coefficient depends on the overlap of the squared wavefunctions of the 2 energy levels undergoing a transition. The larger the overlap the greater the probability a transition between the two energy levels will occur. Wavefunction overlap is not as large in lattice matched systems compared to strained superlattices, as thicker superlattice is needed to achieve the same effective E_g . Thicker superlattice layers means there is a smaller wavefunction overlap as a larger proportion of the wavefunctions are confined within the respective barrier or well.

Despite the smaller wavefunction overlap, high QE has been achieved in InAs/GaAsSb superlattice LWIR photodiodes. An example of this high QE is a structure with a buffer layer of a very different refractive index, made from highly doped InAs [33]. This caused the photodiode to act similar to a resonant cavity causing the absorption coefficient of the sample to increase, thus increasing the QE. At 77 K the device achieved a QE of 65% at 8.9 μm . The device had a 7.28 μm thick absorption region, which would be difficult with a strained superlattice [33]. For

comparison a typical QE for LWIR photodiodes is 36 % at 9 μm at 80 K [57]. A good dark current density for a InAs/GaAsSb with no barriers was $6.05 \times 10^{-5} \text{ Acm}^{-2}$ at -30 mV with a structure of 14 ML InAs/7 ML GaAsSb [58]

1.3.4 InAs/ InAsSb superlattice photodiodes

InAs/InAsSb superlattice structures gained interest due to the lack of Ga. “Ga free” structures were proposed as a way to remove the issue of the natural p type doping caused by defects in Ga based structures [59]. The absorption coefficient for InAs/InAsSb superlattices is 1500 cm^{-1} at 8.2 μm which is lower than other superlattice systems for the same E_g , for example the theoretical absorption coefficient for InAs/InGaSb is 2000 cm^{-1} at the same wavelength [60].

Table 1.4: Summary table of key InAs/InAsSb papers and their properties at 77 K

Paper	Wavelength (μm)	Responsivity (AW^{-1})	Current density (Acm^{-2})	Detectivity ($\text{cm} \cdot \text{Hz}^{1/2} \text{W}^{-1}$)	Bias (mV)	Paper
F	Cut-off 13.2		6.3×10^{-6}		0	[61]
G	12.8	4.8			-300	[62]
H	7.5			5.4×10^{10}		[63]

The device summarised in row F of Table 1.4 is one of the better InAs/InAsSb dark current densities. This is due to the structure having a 300 nm barrier of 8 ML $\text{AlAs}_{0.09}\text{Sb}_{0.91}$ / 9 ML GaSb, the barrier blocks the flow of carriers reducing the dark currents. Another barrier including structure mentioned in row G of Table 1.4 has very good peak responsivity 4.8 AW^{-1} corresponding to a quantum efficiency of 46 % at -300 mV.

The paper reported in row H of Table 1.4 is of note as it has a higher detectivity than other superlattice structures previously mentioned. This structure has a superlattice period of 28 ML InAs/12 ML $\text{InAs}_{0.65}\text{Sb}_{0.35}$.

1.3.5 Barrier Superlattice structures

Barrier including photodiodes have been steadily gaining interest since it was demonstrated in the early 2000's [64]. The nBn structure suppresses the dark current in the infrared photodetectors due to the E_g engineering [64]. There are several forms of barrier structures, some include large E_g structures to block carrier movement in both directions. Others contain complimentary barriers which only block one form of charge carrier from flowing in one direction.

1.3.5.1 nBn designs

Unibarrier structures such as nBn were proposed to decrease both tunnelling currents and thermal generation currents which are often a problem for narrowband structures. Thermal generation

current is initiated by the thermal energy from the devices surroundings exciting carriers into the conduction band. The bandgap structure of an nBn photodiode is depicted in Figure 1.9, the large barrier in the conduction band block electron flow in both directions reducing the dark current of the device. The barrier is designed to stop the formation of depleted regions in the active layers of the structure thus suppressing generation recombination contributions to the dark current. The first nBn structures was proposed in 1997 [65], and the first nBn structure was grown and reported in 2006 [64,66].

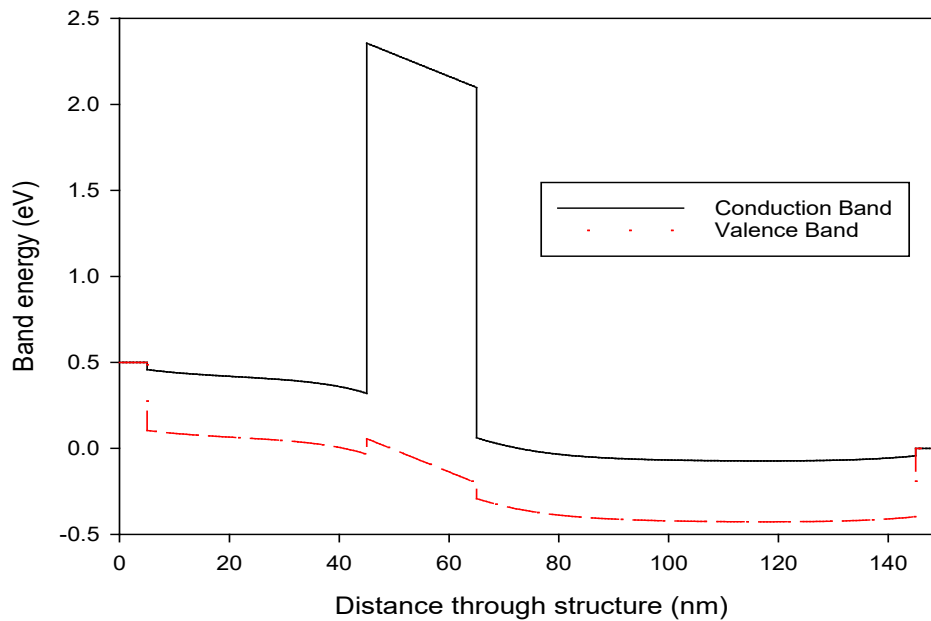


Figure 1.8: The band structure of an nBn photodiode

These early encouraging results have increased interest in the use of barriers to control the dark current in photodiodes. An InAsSb/AlAsSb FPA with QE of 40 % at 9 μm comparative with MCT was reported in 2017 [67]. Another paper from the same group reported a dark current within 10 % of MCT performance [31]. A very high quantum efficiency of 65 % at 8.9 μm was reported in [70], for a structure of 800 periods with an absorption region made up of 22 ML InAs/9 ML GaAsSb.

1.3.5.2 *W and M designs*

Another common barrier design is the so-called W or M structure, first proposed in 2006 [68]. These are superlattices which contain a large E_g material, such as AlSb, inserted into the barrier of the superlattice period blocking carrier flow in both directions. Figure 1.10 shows the band gaps of the M structure superlattice and demonstrates why it's called M structure.

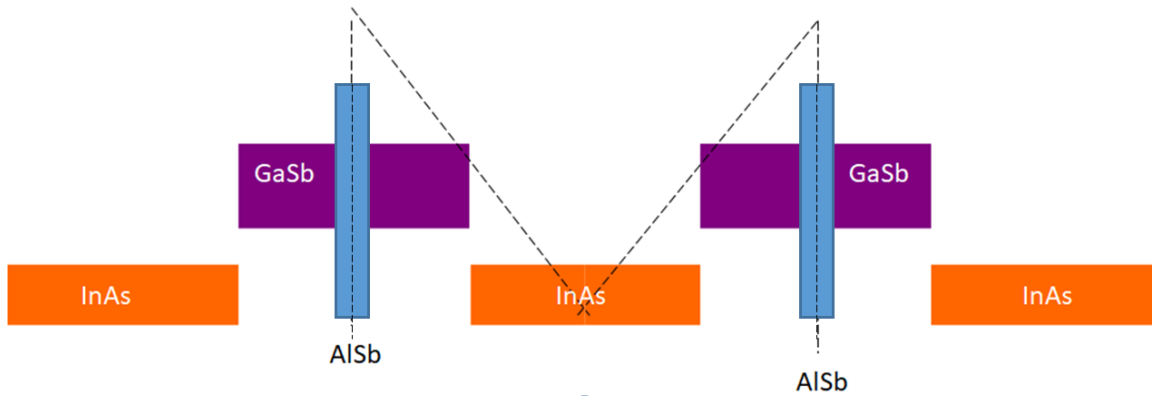


Figure 1.9: The band energy diagram of an InAs/GaSb/AlSb to demonstrate the band structure of an M-structure superlattice

The barrier material thickness is typically 5 ML thick [61]. An InAs/GaSb superlattice was reported with a good responsivity of 3.95 AW^{-1} at $8.1 \mu\text{m}$ at 80 K. The structure was mentioned in section 1.3.2, it has an InAs/GaSb absorption regions and the barrier “m” region contains a superlattice consisting of 18 ML InAs/3 ML GaSb/5 ML AlSb/3 ML GaSb [39]. Results reported in 2008 showed an InAs/GaSb structure with the same barrier region achieved a 20 % QE at $14.58 \mu\text{m}$ [69]. This result is important as the paper reported a dark current density of 4.92 mAcm^{-2} and a R_0A of $1.32 \Omega\text{cm}^2$ which approaches the performance of MCT photodiodes ($1 \Omega\text{cm}^2$ at 78 K) [44].

1.3.5.3 CBIRD structures

Complimentary barrier infrared detector (CBIRD) builds on unibarrier designs and were proposed in 2009 [87]. The design has a barrier to block holes flow in one direction and a barrier to block electron carriers in the other direction. This makes the CBIRD design an attractive option for the long wavelength superlattice designs as it has been shown to reduce dark currents [53,70]. Commonly each barrier is made from a different period of the same superlattice system. The different period gives the superlattice a different E_g , if the E_g is larger than the absorption region it will act as a barrier.

A long wavelength CBIRD structure with a cutoff wavelength of $10 \mu\text{m}$ was presented in 2012 [49]. The structure had an 80 period electron barrier 7 ML InAs/7 ML GaSb which is a variation on the absorption region superlattice (14 ML InAs/ 7 ML GaSb). A CBIRD had a good R_0A of $1.4 \times 10^4 \Omega\text{cm}^2$ and a dark current density less than $1 \times 10^{-5} \text{ Acm}^{-2}$ at 0.18 V which is acceptable for a LWIR photodiode.

1.4 Summary

In this chapter some basic theory for T2SL was discussed. A literature review for different T2SL structures were explored and compared to the common commercial material system MCT. The literature review showed that InAs/GaAs_{0.09}Sb_{0.91} superlattice photodiodes were capable of achieving quantum efficiency within 10 % of the rule of prediction for MCT photodiodes. The InAs/ GaAs_{0.09}Sb_{0.91} devices that manage to achieve this contain barriers and mechanisms to increase the efficiency such as a resonant cavity. In terms of dark current, several InAs/GaSb T2SL structures were able to achieve dark currents lower than MCT. The lower dark currents were due to barriers included in the superlattice structure or high quality crystal growth.

The material system in this work is InAs/GaAs_{0.09}Sb_{0.91}, the review showed the best quantum efficiency to be 65 % in the LWIR with 30 % being a typical result. A typical dark current for a InAs/GaAs_{0.09}Sb_{0.91} T2SL with no barrier included in the structure's design is $6.05 \times 10^{-5} \text{ A cm}^{-2}$ at -30 mV for a 14 ML InAs/7 ML GaAs_{0.09}Sb_{0.91} period. These are the values that will be targets in this thesis.

1.5 Motivation

There are several points of motivation for this work:

- Detectors in the long wavelength and very long wavelength infrared (LWIR, VLWIR) region have many crucial uses including thermal imaging, gas detection, spectroscopy and astronomy [5,6].
- A key motivation for the investigation of type II superlattices for LWIR and VLWIR detectors is the increasing restrictions on detectors containing Mercury Cadmium Telluride. Therefore there is a noticeable need to find equivalent alternative material systems for LWIR and VLWIR.
- Type II superlattice structures offer the advantage of bandgap engineering, generating the ability to design a photodetector that responds to the wavelength of interest. Type II superlattices also have the potential advantage of reduced dark current due to the suppression of Auger recombination.
- Superlattices made from InAs/GaAs_{0.09}Sb_{0.91} are lattice matched, this reduces the number of defects in the crystal structure, which can in turn improve the detector quality.
- Growing and fabricating superlattices photodiodes are expensive so designing and modelling a device beforehand is greatly advantageous.

1.6 Thesis overview

1.6.1 Chapter 2

This chapter discusses and explains the background theory of superlattices and photodiodes. The theory behind the simulation's calculations is also discussed and explained.

1.6.2 Chapter 3

This chapter explains the procedures and methods used in the nextnano++ simulations, how physical photodiode samples are fabricated and how the current density is measured.

1.6.3 Chapter 4

In this chapter simulations of bandgap and cutoff wavelength of superlattices in nextnano++ were verified against literature results. It also simulates InAs/GaAs_{0.09}Sb_{0.91} superlattices over the range of several structures demonstrating the range of cutoff wavelengths available. Absorption of the InAs/GaAs_{0.09}Sb_{0.91} superlattices at 77 K were also simulated and discussed.

1.6.4 Chapter 5

Chapter 5 builds on the results of chapter 4 to extend the absorption and cutoff wavelength simulations to a range of temperatures for 77 K to 300 K. The temperature dependence of different superlattice periods is also discussed.

1.6.5 Chapter 6

This chapter validates the nextnano++ current-density simulations against literature results. Simulations in this chapter explore the current-density of InAs/GaAs_{0.09}Sb_{0.91} superlattices PIN photodiodes. The effect the structure of the superlattice periods has on the current density of the structure.

1.6.6 Chapter 7

Chapter 7 shows the measured current density and blackbody response of a fabricated LWIR structure with barriers in the p and n-regions.

1.6.7 Chapter 8

Chapter 8 summarises the overall findings in this thesis and draws conclusions. Directions for further work based on the findings from this work are also suggested.

References

- ¹ B. G. Streetman, *Solid state electronic devices*, 6th ed., [International ed.]. Upper Saddle River, N.J.: Upper Saddle River, N.J. : Pearson/Prentice Hall, 2006, 2006.
- ² Marc P. Hansen and Douglas S. Malchow, "Overview of SWIR detectors, cameras, and applications," *Proc of SPIE* . vol. 6939, 2008.
- ³ J. Hodgkinson, J. Hodgkinson, and R. P. Tatam, "Optical gas sensing: a review," *Meas. Sci. Technol.*, vol. 24, no. 1, pp. 012004–012004–59, 2013.
- ⁴ J. Wojtas, J. Wojtas, Z. Bielecki, T. Stacewicz, J. Mikołajczyk, and M. Nowakowski, "Ultrasensitive laser spectroscopy for breath analysis," *Opto-Electron. Rev.*, vol. 20(1), pp. 26–39, 2012.
- ⁵ P. C. Klipstein *et al.*, "Type II superlattice technology for LWIR detectors," *Proc.of SPIE*. vol. 9819, pp. 98190T-98190T–10, 2016, doi: 10.1117/12.2222776.
- ⁶ G. H. Rieke, "Infrared detector arrays for astronomy," *Annu. Rev. Astron. Astrophys.*, vol. 45, no. 1, pp. 77–115, 2007.
- ⁷ W. M. Irvine and J. B. Pollack, "Infrared optical properties of water and ice spheres," *Icarus*, vol. 8, pp. 324-360, 1968.
- ⁸ E. Pickwell and V. P. Wallace, "Biomedical applications of terahertz technology," *J Phys D Appl Phys*, vol. 39, p. R301, 2006.
- ⁹ A. Jdidi, N. Sfina, S. A.-B. Nassrallah, M. Saïd, and J. L. Lazzari, "A multi-color quantum well photodetector for mid- and long-wavelength infrared detection," *Semicond Sci Technol*, vol. 26, p. 125019, 2011.
- ¹⁰ B. F. Levine, K. K. Choi, C. G. Bethea, J. Walker, and R. J. Malik, "New 10 μm infrared detector using intersubband absorption in resonant tunneling GaAlAs superlattices," *Appl. Phys. Lett.*, vol. 50, no. 16, pp. 1092–1094, 1987.
- ¹¹ S. D. Gunapala *et al.*, "Long-wavelength 640 \times 486 GaAs/AlGaAs quantum well infrared photodetector snap-shot camera," *IEEE Trans. Electron Devices*, vol. 45, no. 9, pp. 1890–1895, 1998.
- ¹² S. Mou, J. V. Li, and S. L. Chuang, "Quantum Efficiency Analysis of InAs-GaSb Type-II Superlattice Photodiodes," *IEEE J. Quantum Electron.*, vol. 45, no. 6, pp. 737–743, 2009.
- ¹³ B.-M. Nguyen, D. Hoffman, Y. Wei, P.-Y. Delaunay, A. Hood, and M. Razeghi, "Very high quantum efficiency in type-II InAs/GaSb superlattice photodiode with cutoff of 12 μm ," *Appl. Phys. Lett.*, vol. 90, no. 23, p. 231108, 2007, doi: 10.1063/1.2746943.
- ¹⁴ C. Jin, F. Wang, Q. Xu, C. Yu, J. Chen, and L. He, "Beryllium compensation doped InGaAs/GaAsSb superlattice photodiodes," *J. Cryst. Growth*, vol. 477, pp. 100–103, 2017.
- ¹⁵ M. Anthony M. Fox, *Optical properties of solids*. Oxford: Oxford, 2001.
- ¹⁶ C. H. Grein, P. M. Young, and H. Ehrenreich, "Minority carrier lifetimes in ideal InGaSb/InAs superlattices," *Appl. Phys. Lett.*, vol. 61, pp. 2905-2907, 1992.
- ¹⁷ G. G. Zegrya and A. D. Andreev "Theory of the recombination of nonequilibrium carriers in type-II heterostructures" *JETP* vol. 82 (2), (1996).
- ¹⁸ G. A. Sai-Halasz, R. Tsu, and L. Esaki, "A new semiconductor superlattice," *Appl. Phys. Lett.*, vol. 30, no. 12, pp. 651–653, 1977, doi: 10.1063/1.89273.
- ¹⁹ European Commission (2018) [Online]. EU rules on mercury in action http://ec.europa.eu/chemical/mercury/index_en.htm 2018 doi: 10.2779/791147 [Accessed: 2021-2-03]
- ²⁰ Science for Environment Policy (2017) Tackling mercury pollution in the EU and worldwide. (Online) Available: <http://ec.europa.eu/science-environment-policy> [Accessed: 2021-2-03]
- ²¹ E. R. Youngdale, J. R. Meyer, C. A. Hoffman, F. J. Bartoli, C. H. Grein, P. M. Young, *et al.*, "Auger lifetime enhancement in InAs-Ga_{1-x}In_xSb superlattices," *Appl. Phys. Lett.*, vol. 64, pp. 3160-3162, 1994.
- ²² C. H. Grein, P. M. Young, M. E. Flatté, and H. Ehrenreich, "Long wavelength InAs/InGaSb infrared detectors: Optimization of carrier lifetimes," *J Appl Phys*, vol. 78, pp. 7143-7152, 1995.

- ²³ Y. Wei, W. Ma, Y. Zhang, J. Huang, Y. Cao, and K. Cui, "High Structural Quality of Type II InAs/GaSb Superlattice for Very Long Wavelength Infrared Detection by Interface Control," *IEEE J. Quantum Electron.*, vol. 48, pp. 512-515, 2012.
- ²⁴ J. L. Johnson, L. A. Samoska, A. C. Gossard, J. L. Merz, M. D. Jack, G. R. Chapman, *et al.*, "Electrical and optical properties of infrared photodiodes using the InAs/Ga_{1-x}In_xSb superlattice in heterojunctions with GaSb," *J Appl Phys*, vol. 80, pp. 1116-1127, 1996.
- ²⁵ C. H. Grein, W. H. Lau, T. L. Harbert, and M. E. Flatte, "Modeling of very long infrared wavelength InAs/GaInSb strained layer superlattice detectors" *Proc. Of SPIE* vol. 4795:, 2002.
- ²⁶ P. W. Kruse, M. D. Blue, J. H. Garfunkel, and W. D. Saur, "Long wavelength photoeffects in mercury selenide, mercury telluride, and mercury telluride-cadmium telluride," *Infrared Phys*, vol. 2, pp. 53-60, 1962/01/01/ 1962.
- ²⁷ A. N. Kohn and J. J. Schlickman, "1-2 micron (Hg, Cd)Te photodetectors," *IEEE Trans Electron Devices*, vol. 16, pp. 885-890, 1969.
- ²⁸ T. labs. (2017) HgCdTe Multi-Junction Photovoltaic Detector with TEC, 10.6 μm, 1 mm² Active Area. (Online) Available: https://www.thorlabs.com/images/tabimages/MCT_PV_Detector_Sample.pdf [Accessed: 2021-04-01]
- ²⁹ G. J. H. Brown, S.; Szmulowicz, F.; Mahalingam, K.; Haugan, H.; Wei, Y.; Gin, A.; Razeghi, M., "Type-II Superlattice Photodiodes: an Alternative for VLWIR Detection.," *Proc. of SPIE*, vol. 5074, pp. 191- 198, 2003.
- ³⁰ P. Madejczyk, W. Gawron, A. Piotrowski, K. Kłos, J. Rutkowski, and A. Rogalski, "Improvement in performance of high-operating temperature HgCdTe photodiodes," *Infrared Phys Technol*, vol. 54, pp. 310-315, 2011/05/01/ 2011.
- ³¹ P. C. Klipstein *et al.*, "Type II Superlattice Infrared Detector Technology at SCD," *J. Electron. Mater.*, vol. 47, no. 10, pp. 5725–5729, 2018, doi: 10.1007/s11664-018-6527-8.
- ³² Z. Xu, J. Chen, F. Wang, Y. Zhou, and L. He, "High performance InAs/GaAsSb superlattice long wavelength infrared photo-detectors grown on InAs substrates," *Semicond. Sci. Technol.*, vol. 32, no. 5, p. 55011, 2017, doi: 10.1088/1361-6641/aa6377.
- ³³ M. Huang, J. Chen, Y. Zhou, Z. Xu, and L. He, "light-harvesting for high quantum efficiency in InAs-based InAs/ GaAsSb type-II superlattices long wavelength infrared photodiodes," *Appl. Phys. Lett.*, vol. 114, p. 141102, 2019.
- ³⁴ R. Chevallier, A. Haddadi, and M. Razeghi, "Toward realization of small-sized dual-band long-wavelength infrared photodetectors based on InAs/GaSb/AlSb/AlSb type-II superlattices," *Solid State Electron*, vol. 136, pp. 55-54, 2017/10/01/2017.
- ³⁵ R. Chevallier, A. Haddadi, and M. Razeghi, "Dark current reduction in microjunction-based double electron barrier type-II InAs/InAsSb superlattice long-wavelength infrared photodetectors," *Sci Rep*, vol. 7, no. 1, pp. 12617–6, 2017, doi: 10.1038/s41598-017-13016-9.
- ³⁶ R. Alchaar, J. B. Rodriguez, L. Höglund, S. Naureen, and P. Christol, "Characterization of an InAs/GaSb type-II superlattice barrier photodetector operating in the LWIR domain," *AIP Adv.*, vol. 9, no. 5, p. 055012, May 2019, doi: 10.1063/1.5094703.
- ³⁷ T.-T. Qi *et al.*, "Growth and characterization of type-II superlattice photodiodes with cutoff wavelength of 12 μm on 4-in. wafer," *Opt. Quantum Electron.*, vol. 51, no. 9, pp. 1–8, 2019, doi: 10.1007/s11082-019-1988-4.
- ³⁸ Hao *et al.*, "InAs/GaSb superlattice photodetector with cutoff wavelength around 12 μm based on an Al-free nBn structure grown by MOCVD," *Semicond. Sci. Technol.*, vol. 34, no. 6, p. 65013, 2019, doi: 10.1088/1361-6641/ab2006.
- ³⁹ B.-S. Tan, C.-J. Zhang, W.-H. Zhou, X.-J. Yang, G.-W. Wang, Y.-T. Li, *et al.*, "The 640 × 512 LWIR type-II superlattice detectors operating at 110 K," *Infrared Phys Technol* vol. 89, pp. 168-173, 2018/03/01/ 2018.
- ⁴⁰ X. Han *et al.*, "Very long wavelength infrared focal plane arrays with 50% cutoff wavelength based on type-II InAs/GaSb superlattice," *Chin. Phys. B*, vol. 26, no. 1, p. 18505, 2017, doi: 10.1088/1674-1056/26/1/018505.

- ⁴¹ D. Jiang *et al.*, “Very high quantum efficiency in InAs/GaSb superlattice for very long wavelength detection with cutoff of 21 μm ,” *Appl. Phys. Lett.*, vol. 108, no. 12, p. 121110, 2016, doi: 10.1063/1.4944849.
- ⁴² A. Haddadi, A. Dehzangi, S. Adhikary, R. Chevallier, and M. Razeghi, “Background-limited long wavelength infrared InAs/InAs_{1-x}Sb_x type-II superlattice-based photodetectors operating at 110 K,” *APL Mater.*, vol. 5, no. 3, pp. 035502-035502-5, 2017, doi: 10.1063/1.4975619.
- ⁴³ A. Haddadi, A. Dehzangi, R. Chevallier, S. Adhikary, and M. Razeghi, “Bias-selectable nBn dual-band long-/very long-wavelength infrared photodetectors based on InAs/InAs_{1-x}Sb_x/AlAs_{1-x}Sb_x type-II superlattices,” *Sci. Rep.*, vol. 7, no. 1, pp. 1-7, 2017,
- ⁴⁴ W. E. Tennant, D. Lee, M. Zandian, E. Piquette, and M. Carmody, “MBE HgCdTe Technology: A Very General Solution to IR Detection, Described by ‘Rule 07’, a Very Convenient Heuristic,” *J. Electron. Mater.*, vol. 37, no. 9, pp. 1406-1410, 2008,
- ⁴⁵ W. E. Tennant, “‘Rule 07’ Revisited: Still a Good Heuristic Predictor of p/n HgCdTe Photodiode Performance?,” *J. Electron. Mater.*, vol. 39, no. 7, pp. 1030-1035, 2010, doi: 10.1007/s11664-010-1084-9.
- ⁴⁶ Z. Xu *et al.*, “MBE growth and characterization of type-II InAs/GaSb superlattices LWIR materials and photodetectors with barrier structures,” *J. Cryst. Growth*, vol. 477, pp. 277-282, 2017, doi: 10.1016/j.jcrysgro.2017.03.041.
- ⁴⁷ A. Hood *et al.*, “Near bulk-limited ROA of long-wavelength infrared type-II InAs/GaSb superlattice photodiodes with polyimide surface passivation,” *Appl. Phys. Lett.*, vol. 90, no. 23, p. 233513, 2007, doi: 10.1063/1.2747172.
- ⁴⁸ C. J. Hill, J. V. Li, J. M. Mumolo, and S. D. Gunapala, “MBE grown type-II MWIR and LWIR superlattice photodiodes,” *Infrared Phys. Technol.*, vol. 50, no. 2-3, pp. 187-190, 2007,
- ⁴⁹ D.Z.Y. Ting *et al.* “A high performance long wavelength superlattice complementary barrier infrared detector,” *Appl. Phys. Lett.*, vol. 95 p.023508, (2009)
- ⁵⁰ A. Rogalski, M. Kopytko, and P. Martyniuk, “InAs/GaSb type-II superlattice infrared detectors: three decades of development,” May 2017, vol. 10177, doi: 10.1117/12.2272817.
- ⁵¹ Y. Wei, A. Gin, M. Razeghi, and G. J. Brown, “Advanced InAs/GaSb superlattice photovoltaic detectors for very long wavelength infrared applications,” *Appl. Phys. Lett.*, vol. 80, no. 18, pp. 3262-3264, 2002, doi: 10.1063/1.1476395.
- ⁵² Y. Zhang *et al.*, “Narrow-band long-/very-long wavelength two-color type-II InAs/GaSb superlattice photodetector by changing the bias polarity,” *Appl. Phys. Lett.*, vol. 100, no. 17, pp. 173511-173511-4, 2012, doi: 10.1063/1.4707162.
- ⁵³ D. Z.-Y. Ting *et al.*, “Antimonide superlattice complementary barrier infrared detector (CBIRD),” *Proc. Int. Conf. Quantum Struct. Infrared Photodetector QSIP 2010*, vol. 54, no. 3, pp. 267-272, May 2011, doi: 10.1016/j.infrared.2010.12
- ⁵⁴ H. Mohseni, M. Razeghi, G. J. Brown, and Y. S. Park, “High-performance InAs/GaSb superlattice photodiodes for the very long wavelength infrared range,” *Appl. Phys. Lett.*, vol. 78, no. 15, pp. 2107-2109, 2001, doi: 10.1063/1.1362179.
- ⁵⁵ E. F. Schubert, Gessmann, T. and Kim, J. K. , *Light emitting diodes*. Wiley Online Library: Wiley, 2005.
- ⁵⁶ D. H. Chow, R. H. Miles, J. R. Söderström, and T. C. McGill, “Growth and characterization of InAs/Ga_{1-x}In_xSb strained-layer superlattices,” *Appl. Phys. Lett.*, vol. 56, no. 15, pp. 1418-1420, Apr. 1990, doi: 10.1063/1.102486.
- ⁵⁷ M. Huang, J. Chen, J. Xu, F. Wang, Z. Xu, and L. He, "ICP etching for InAs-based InAs/GaAsSb superlattice long wavelength infrared detectors," *Infrared Phys Technol*, vol. 90, pp. 110-114, 2018/05/01/ 2018.
- ⁵⁸ F. Wang, J. Chen, Z. Xu, Y. Zhou, and L. He, "InAs-based InAs/GaAsSb type-II superlattices: Growth and characterization," *J. Cryst. Growth*, vol. 416, pp. 130-133, 2015/04/15/ 2015.
- ⁵⁹ S. P. Svensson, D. Donetsky, D. Wang, H. Hier, F. J. Crowne, and G. Belenky, "Growth of type II strained layer superlattice, bulk InAs and GaSb materials for minority lifetime characterization," *J. Cryst. Growth*, vol. 334, pp. 103-107, 11/01/ 2011.

-
- ⁶⁰ C. H. Grein, M. E. Flatte and H. Ehrenreich, "Comparison of ideal InAs-InAs_{1-x}Sb_x and InAs-In_xGa_{1-x}Sb superlattice IR detectors," in *Proc.of the Third International Symposium on Long Wavelength Infrared Detectors and Arrays: Physics and Applications III*, pp. 211-18, 1995.
- ⁶¹ H. S. Kim, O. O. Cellek, Z.-Y. Lin, Z.-Y. He, X.-H. Zhao, S. Liu, *et al.*, "Long-wave infrared nBn photodetectors based on InAs/InAsSb type-II superlattices," *Appl. Phys. Lett* vol. 101, p. 161114, 2012.
- ⁶² A. M. Hoang, G. Chen, R.Chevallier, A. Haddadi, and M. Razeghi, "High performance photodiodes based in InAs/InAsSb type-II superlattice for very long wavelength infrared detection," *Appl. Phys. Lett* vol. 104, p. 251105, 2014.
- ⁶³ D. H. Wu, A. Dehzangi, Y. Y. Zhang, and M. Razeghi, "Demonstration of long wavelength infrared type-II InAs/InAs_{1-x}Sb_x superlattices photodiodes on GaSb substrate grown by metalorganic chemical vapor deposition," *Appl. Phys. Lett* vol. 112, p. 241103, 2018.
- ⁶⁴ Maimon, S, and Wicks, G. W. "NBn Detector, an Infrared Detector with Reduced Dark Current and Higher Operating Temperature." *Appl. Phys. Lett.*, 89.15 (2006): 151109.
- ⁶⁵ G.H. Avetisyan, V.B. Kulikov, V.P. Kotov, I.D. Zalevsky, P.V. Bulaev, A.A. Padalitsa, V.A. Gorbylev "Infrared photodetectors based on narrow-gap A_{III}B_V semiconductor materials grown by LP-MOCVD" *Proc.SPIE*, vol. 3200 (1997).
- ⁶⁶ Philip Klipstein. "'XBN' Barrier Photodetectors for High Sensitivity and High Operating Temperature Infrared Sensors," *Proc.SPIE*, Vol. 6940, 2008.
- ⁶⁷ P. C. Klipstein *et al.*, "Development and Production of Array Barrier Detectors at SCD," *J. Electron. Mater.*, vol. 46, no. 9, pp. 5386–5393, 2017, doi: 10.1007/s11664-017-5590-x.
- ⁶⁸ Rogalski, A, and Martyniuk, P. "InAs/GaInSb Superlattices as a Promising Material System for Third Generation Infrared Detectors." *Infrared Phys Technol*, 48.1 pp. 39-52 (2006)
- ⁶⁹ D. Hoffman *et al.*, "The effect of doping the M-barrier in very long-wave type-II InAs/GaSb heterodiodes," *Appl. Phys. Lett.*, vol. 93, no. 3, pp. 031107-031107–3, 2008, doi: 10.1063/1.2963980.
- ⁷⁰ David Z. Ting *et al.*, "Antimonide type-II superlattice barrier infrared detectors," *Proc.SPIE*, May 2017, vol. 10177, doi: 10.1117/12.2266263..02

2 Background Theory

Building on the theories introduced in the previous chapter, this chapter explores the basic background theory for superlattice photodiodes in more detail. The current mechanisms of photodiodes and other theories such as optical absorption are explored to highlight how these properties behave in real detectors before applying this to simulated detectors. The theory and settings used in the simulations for this thesis are also explored to better understand the theory and equations behind them.

2.1 *Wavefunctions and wavefunction overlap*

Wavefunctions are used to describe the state of the electron in a quantum well or superlattice. The form of a wavefunction (ψ) is seen below,

$$\psi(x, t) \tag{2.1}$$

where x is position and t is time. One important property of wavefunctions is that the wavefunction squared in given in equation (2.2) is the probability (P) of the carrier is at position x at time t . Figure 2.1 shows pictorially the probability of an electron in the first electron level being in the well or the barrier of the superlattice. CB is the conduction band, HH is the heavy hole band and E1 is the first energy level in the conduction band in the well.

$$|\psi(x, t)|^2 = P(x, t) \tag{2.2}$$

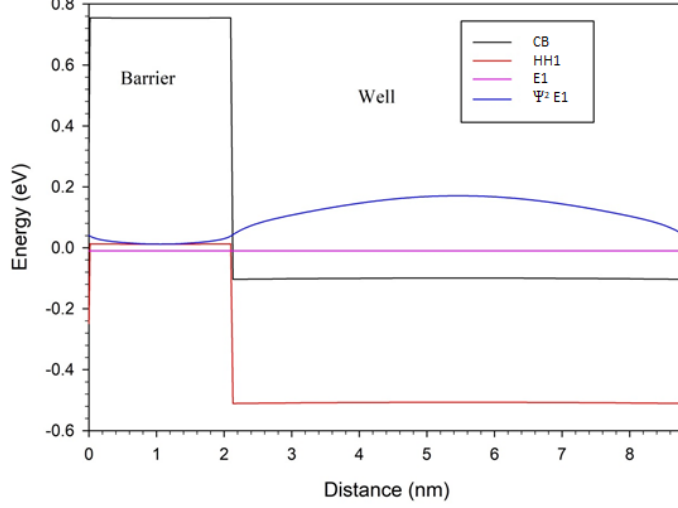


Figure 2.1: The ψ^2 for the first electron energy level, showing the probability of the position of an electron on that energy level

The wavefunctions are used in the Schrödinger equation and are used to find solutions to it. The Schrödinger equation is shown below,

$$\hat{H}\psi = \left(\frac{\hat{p}^2}{2m} + \hat{V} \right) \psi = \hat{E}\psi \quad (2.3)$$

where m is the mass of the particle, \hat{p} momentum of the particle, V is the potential, \hat{H} is the Hamiltonian and \hat{E} is energy. Periodic structures, such as superlattices, can use Bloch theorem to calculate the solutions to the Schrödinger equation for periodic structures. The equation for the Bloch function is written as

$$\psi_{n,k}(\hat{x}) = \exp^{i\hat{k}\cdot\hat{x}} u_{n,\hat{k}}(\hat{x}) \quad (2.4)$$

where ψ_{nk} is the wavefunction of energy level (n) at a certain value of k which is usually 0, \hat{x} is the position vector, i is imaginary, $u_{n,\hat{k}}(\hat{x})$ is the periodicity of the crystal and \hat{k} is crystal momentum vector.

2.2 Periodic Boundaries

The effective E_g and the wavefunctions of the T2SL in this work were calculated using the nextnano software [1]. To simulate infinite superlattice structures periodic boundaries were applied [2]. These structures were defined as one period of the superlattice with periodic boundaries. The period of the superlattice was defined as the combined width of the well and the

barrier. For a simple superlattice the period of the superlattice would be the width of the well and the barrier. Periodic boundary conditions allows for a simplification of the model by assuming a position in one period sees the same forces, energies etc as the same position in another period. A pictorial demonstration of periodic boundary conditions in a crystal structure is depicted in Figure 2.2 the grey square is the small repeating unit that periodic boundaries are applied to. The two size circles (pink and blue) represent two different atoms in the crystal structure with the arrow depicting the atom is equivalent to the other atom inside the repeating unit.

By applying periodic boundaries the speed of the E_g simulations has been dramatically sped up from 1-2 hours to 20 minutes. The computer used in this thesis had an i5-2500 CPU, with 4 cores and 16.0 GB of RAM, a higher specification computer will have shorter computational time.

The calculations use the standard 8 band $k \cdot p$ envelope function approximation. The parameters are taken from the paper by Vurgaftman [3].

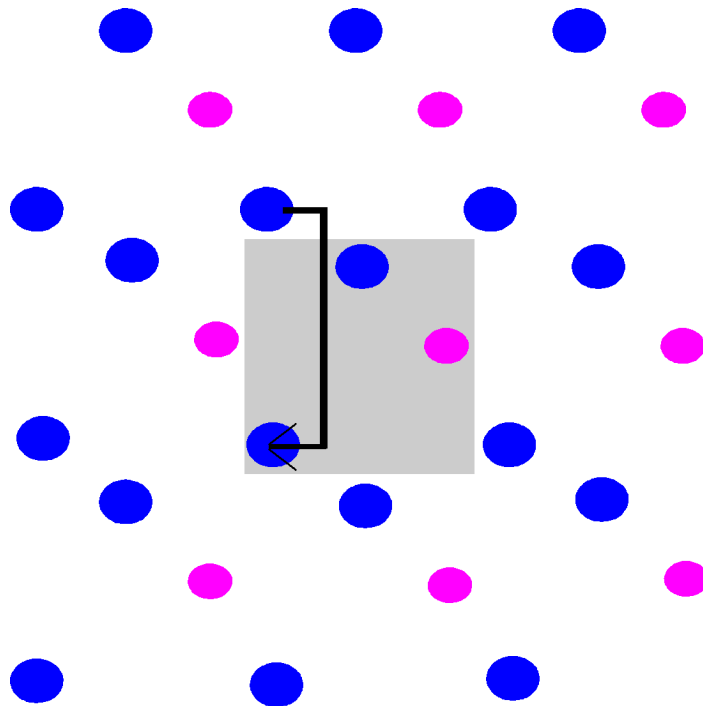


Figure 2.2: The pictorial diagram of the periodic boundaries in a crystal structure

2.3 $k.p.$ theory

6]. The $k.p$ model uses perturbation theory to solve the Schrödinger equation (2.5),

$$\hat{H}\psi_{nk}(\hat{x}) = \left[\frac{\hat{p}^2}{2m_0} + \hat{V}(\hat{x}) \right] \psi_{nk}(\hat{x}) = \hat{E}_n(\hat{k})\psi_{nk}(\hat{x})$$

(2.5)

where m_0 is the mass of the electron. Single band k.p theory combines substituting the Bloch functions (2.4) and the wavefunction (2.1) into the Schrödinger equation, (2.5), to give equation (2.6).

$$\hat{H}\psi_{nk}(\hat{x}) = \left[\frac{\hat{p}^2}{2m_0} + \hat{V}(\hat{x}) \right] \exp^{i\hat{k}\cdot\hat{x}} u_{n\hat{k}}(\hat{x}) \quad (2.6)$$

To calculate k.p, first order perturbation of (2.6) gives

$$\begin{aligned} \hat{H}\psi_{nk}(\hat{x}) &= \frac{1}{2m_0} \left(\hbar(\hat{k} \cdot \hat{p}) \exp^{i\hat{k}\cdot\hat{x}} u_{nk}(\hat{x}) + \hbar^2 \hat{k}^2 \exp^{i\hat{k}\cdot\hat{x}} u_{nk}(\hat{x}) + \exp^{i\hat{k}\cdot\hat{x}} u_{n\hat{k}}(\hat{x}) \hat{p}^2 \right. \\ &\quad \left. + \hbar \exp^{i\hat{k}\cdot\hat{x}} (\hat{k} \cdot \hat{p}) u_{nk}(\hat{x}) \right) + \hat{V} \exp^{i\hat{k}\cdot\hat{x}} u_{n\hat{k}}(\hat{x}) = \hat{E} \exp^{i\hat{k}\cdot\hat{x}} u_{n\hat{k}}(\hat{x}) \end{aligned} \quad (2.7)$$

which simplifies to

$$\left[\frac{\hat{p}^2}{2m_0} + \frac{\hbar \hat{k} \cdot \hat{p}}{m_0} + \frac{\hbar^2 \hat{k}^2}{2m_0} + \hat{V}(\hat{x}) \right] u_{n\hat{k}}(\hat{x}) = E_n(\hat{k}) u_{n\hat{k}}(\hat{x}) \quad (2.8)$$

The second term in Equation (2.8) is why this method of solving the Schrödinger equation is call k.p. theory.

In equation (2.8) $\frac{\hat{p}^2}{2m_0} + \hat{V}(\hat{x})$ corresponds to the free electron part of the Hamiltonian and $\frac{\hbar \hat{k} \cdot \hat{p}}{m_0} + \frac{\hbar^2 \hat{k}^2}{2m_0}$ corresponds to the k vector crystal dependent part of the Hamiltonian.

The second order perturbation of equation (2.8) between two bands n and n' gives:

$$\hat{E}_n(\hat{k}) = E_n(0) + \frac{\hbar^2 \hat{k}^2}{2m_0} + \frac{\hbar}{m_0} \hat{k} \cdot \hat{p}_{nn'} + \frac{\hbar^2}{m_0^2} \sum_{n \neq n'} \frac{|\hat{k} \cdot \hat{p}_{nn'}|^2}{E_n(0) - E_{n'}(0)} \quad (2.9)$$

where $E_n(0)$ is $E_n(k)$ at $k=0$, n is the band the equation is concerned with and n' is other bands accounted for in $\frac{\hbar^2}{m_0^2} \sum_{n \neq n'} \frac{|\hat{k} \cdot \hat{p}_{nn'}|^2}{E_n(0) - E_{n'}(0)}$.

A matrix is expanded from the equations to calculate multiple bands k.p theory. The most common type of k.p calculations used is 8 band k.p theory which is used in the simulations in this thesis. 8 band k.p theory creates an 8x8 matrix Hamiltonian as part of the Schrödinger equation. Including a larger matrix, more bands, improves the accuracy of the simulation, though this is a trade off with the simulation time and computational intensity.

2.3.1 Envelope function

The envelope function approximation allows for the calculation of E_g in finite superlattice structures accounting for changes in the structures due to applied bias. The envelope function can then be used to adapt the band structure calculations for nano structures. The calculations use constant bulk parameters, such as band offsets, and assume there is no band mixing, only varying the perturbation potential over the superlattice period. The perturbation potential of the envelope function only varies the Hamiltonian of the Schrödinger equation which is expressed as,

$$[\hat{H}_0 + \hat{V}(\hat{x})]\psi(\hat{x}) = \hat{E}\psi(\hat{x}) \quad (2.10)$$

where H_0 is the free electron part of the Hamiltonian, $V(x)$ is the potential energy.

In the envelope function approximation the Bloch functions ($\psi_{n,k_0}(\hat{x})$),

$$\psi_{n,\hat{k}}(\hat{x}) = e^{i\hat{k}\cdot\hat{x}}u_{n,\hat{k}}(\hat{x}) \quad (2.4) \text{ repeated}$$

are substituted into the wavefunction of the semiconductor to give,

$$\psi(\hat{x}) = F_n(\hat{k})u_{n,\hat{k}}(\hat{x}) \quad (2.11)$$

where F_n is the periodic component of the Bloch function, only applying the boundary conditions to an area defined by the envelope i.e. one period of the superlattice.

The effective mass of the carrier is extracted from the 8 k·p band calculation and this is used to calculate the 8 k·p eigenstates for the structure. These eigenstates are then used to calculate wavefunctions, energy levels and absorption coefficient of polarised light in a superlattice structure.

2.4 Optical absorption

Absorption depends on several parameters, the bandgap of the semiconductor; the thickness of the material absorbing the light; and the wavefunction overlap of the two wavefunctions included in the transition. If the wavefunction overlap is larger the absorption coefficient will be larger. The calculations of absorption coefficient in a superlattice are detailed in [7].

The absorption of a material can be quantified by its absorption coefficient. It is the power of light absorbed by the material per unit length. The Beer-Lambert law is used to describe how the absorption of light decreases as it moves through material, the optical intensity (I) of the light at distance (d) through the material can be defined as,

$$I_d = I_0 e^{-\alpha d} \quad (2.12)$$

where I_0 is the optical intensity at the surface, α is the absorption coefficient and d is the distance through the material. The Beer-Lambert law shows that larger absorption regions are preferable, to make sure the percentage of light absorbed is increased.

The absorption coefficient depends on the wavelength of light exposed to the material, as materials may absorb one wavelength but may not be able to absorb a longer wavelength. Absorption coefficient can be defined as,

$$\alpha = \frac{4\pi\kappa}{\lambda} \quad (2.13)$$

where λ is wavelength and κ is the extinction coefficient of the material. The extinction coefficient is the imaginary part of the complex refractive index of the material.

In a quantum well there are allowed transitions where the lowest interband transition is the bandgap. This causes the absorption coefficient of the quantum wells to have a step-like appearance as seen in Figure 2.3. Details on how nextnano++ handles this calculation will be covered in greater detail in chapter 3.

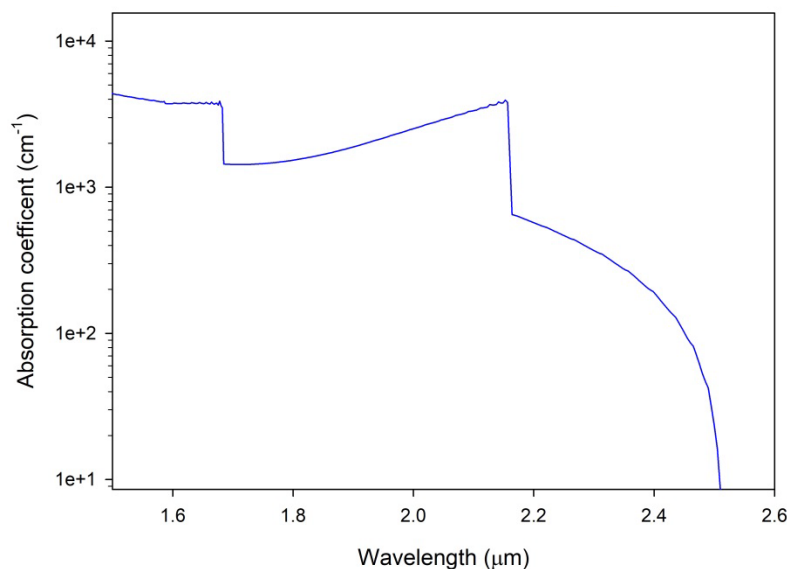


Figure 2.3: The absorption spectra for a simulated SWIR InGaAs/GaAsSb at room temperature

Absorption coefficient is affected by the wavefunction overlap between the two states involved the transition, which indicates the likelihood of the transition happening [8,9].The wavefunction

overlap the transition between the first heavy hole energy level (HH1) and the first electron energy level (E1) is defined as,

$$\text{Wavefunction overlap} = \int_{-\infty}^{\infty} \psi_{(E1)}^2(x) \psi_{(HH1)}^2(x) dx \quad (2.14)$$

where $\psi_{(E1)}^2$ is the squared wavefunction of the first electron level and $\psi_{(HH1)}^2$ is the squared wavefunction of the first heavy hole level. The larger the wavefunction overlap the larger the absorption coefficient, the transition will happen where the wavefunctions overlap to conserve momentum. For T2SL the overlap of wavefunctions is where they decay into the other material layer. This is a small area near the interface of the layers this is why the absorption for T2SL is lower than the T1SL as the transitions for T1SL can happen anywhere in the well material.

2.5 Current density simulations

Nextnano++ extracts the effective masses and E_g from the band structure model. The superlattice is then simplified by making superlattices act as “bulk” material with the same effective masses and E_g as the superlattice. E_g is extracted from the k·p data from nextnano++.

This means detector performance can be computed. The electron and hole transport through the device structure can be calculated by solving Poisson’s equation stated below

$$-\nabla \cdot \epsilon \nabla \phi = q(A - D + N_D^+ - N_A^-) \quad (2.15)$$

where ∇ is the laplace operator, ϵ is the dielectric constant, ϕ is the electrostatic potential and q is the charge of an electron. The density of electrons and holes are A and D respectively, while N_D^+ and N_A^- represent the ionisation concentrations of donors and acceptors. The electrons and holes that are mobile are treated as ideal fermi gases, they will not interact with each other. Then the charge carrier momentum is conserved by solving the continuity equations for electrons and holes. The electron current density (J_n) is defined as,

$$J_n = \frac{q}{4\pi^3} \int v \left[\frac{q\tau_k}{\hbar} \nabla \psi \cdot \nabla f \right] dk \quad (2.16)$$

where v is velocity, τ_k is the momentum relaxation time, f is the fermi distribution for electrons and the integral is for all the electron momentum vectors, a separate equivalent equation is used for the holes. The current density can then be used to calculate the net recombination rates.

$$\frac{\partial n}{\partial t} = \frac{1}{q} \nabla \cdot J_{pn} + (G_{rad} - U_{SRH}) \quad (2.17)$$

where the generation rate for electrons G_{rad} is and U_{srh} is the total recombination rate. J_{pn} is the contributions to the current caused by the drift current and the diffusion current. This is combined to thermionic emission ensuring a stable simulation. Using this, the photo generation rate is approximated as:

$$G_{rad} = (1 - r)Q\alpha(\lambda)e^{-\alpha(\lambda)\delta z} \quad (2.18)$$

where r is the reflectivity at the top surface of the device, Q is the incident light's photon flux, and α is the absorption coefficient at the wavelength of interest (λ). δz is the distance the light travels in the z direction, the direction the light is travelling in. For the nextnano++ simulations the generation rate is specified in the input file. No recombination mechanisms are considered in this equation.

Changing the minimum and maximum carrier density (n) values have a big effect on the current density. The carrier density is part of the drift and diffusion current equations (equations (2.19) and (2.20)). Limiting the range of allowed values for n makes it easier for the simulation to converge on the correct values of current density for the E_g of the structure. The drift-current equation is defined as,

$$J_n = qn_i\mu_n E \quad (2.19)$$

where n_i is the number of electrons per cubic centimetre. This number is calculated at each point in the structure and must fall inside a range of acceptable values in the nextnano++ simulations. The mobility of electrons is μ_n with units $\text{cm}^2\text{V}^{-1}\text{s}^{-1}$ and E is the applied electric field (Vcm^{-1}). Drift current is the movement of majority carriers in a region (electrons in the n-type region) as determined by the electric field. The operating bias conditions change which carriers contribute to the diffusion current density. In the forward bias, majority carriers diffuse towards the oppositely doped material. Under reverse bias, minority carriers diffuse to an area of high carrier concentration, i.e. electrons from the P region moving to the N region. The diffusion current density equation is expressed as,

$$J_{diff} = J_0 \left[\exp\left(\frac{qV}{k_b T}\right) - 1 \right] \quad (2.20)$$

where n_f is the ideality factor, J_0 is the saturation current, R_s is the contact resistance, k_b is Boltzmann's constant, and T is the temperature. In reverse bias the exponential is negligible; the saturation current is the only variable for the reverse bias diffusion current density. The saturation current (J_0) depends on the concentration of the acceptors and donors $N_{A,D}$, and is depicted as,

$$J_0 = q \left(\frac{D_D n_i^2}{L_D N_A} + \frac{D_A n_i^2}{L_A N_D} \right) \quad (2.21)$$

where L_D and L_A are the minority carrier diffusion lengths of the electron and holes respectively. D_D and D_A are the diffusion coefficients of the electrons and holes and the intrinsic carrier concentration is n_i .

2.5.1 Recombination and mobility

There are two mechanisms which contribute to the recombination current in the simulations in this thesis. They are:

- Schottky-Read-Hall recombination
- Auger Recombination

Schottky-Read-Hall recombination

Schottky-Read-Hall recombination covers recombination current caused by traps in the E_g of the semiconductor. Traps are intermediate energy levels inside the E_g introduced by defects, and thus a way to reduce this recombination is to use defect free materials. An electron in the conduction band is promoted to the trap, loses energy in the trap and relaxes down to its original state. The Schottky-Read-Hall recombination equation is,

$$R_{SRH} = \frac{A \cdot D - n_i^2}{\tau_A \cdot (D + D_1) + \tau_D \cdot (A + A_1)} \quad (2.22)$$

where n_i is the intrinsic density and A and D are the carrier concentrations for holes and electrons respectively. τ_A and τ_D are the scattering times the holes and electrons respectively. D_1 and A_1 are parameters for the recombination dependency on the energy level of the traps in the structure. The intrinsic density is given as a simulation parameter in the input file of nextnano++.

Auger recombination

Auger recombination is a three-body effect and therefore mainly occurs in regions of high carrier density. The equation for all auger recombination is given in equation (2.27). C_D and C_A are the auger recombination coefficients with the units (cm^6s^{-1}). These coefficients are material dependent parameters written in the nextnano++ database.

$$R_{Auger} = C_D D(A^2 - n_i^2) + C_A A(D^2 - n_i^2) \quad (2.23)$$

2.5.2 Poisson equation

The Poisson equation is used to describe the distribution of the electric field caused by a charged particle.

$$\nabla^2 \phi = \frac{-\rho(x)}{\epsilon_0} \quad (2.24)$$

where ϕ is electrostatic potential, ∇ is the laplace operator, $\rho(x)$ is charge density and ϵ_0 is permittivity of free space. The Poisson equation for a semiconductor for nano structures such as a quantum well can be written as

$$\hat{\nabla} \cdot [\epsilon(\hat{x}) \hat{\nabla} \phi(\hat{x})] = -\rho(\hat{x}) \quad (2.25)$$

Where $\phi(\hat{x})$ is the electrostatic potential, $\epsilon(\hat{x})$ and $\rho(\hat{x})$ are a position dielectric tensor and the charge density respectively. The charge density includes the hole density ($A(x)$), electron density ($D(x)$), ionized acceptors (N_A^-) and donors (N_D^+) and finally the density of fixed charges. The fixed charges have contributions from polarized charges and the surface and volume charges. The Poisson equation calculations require boundary conditions of the nanostructure to be set to find a unique solution to the Poisson equation. These boundary conditions are used at the interfaces of the contacts of the structure though the contacts are not included in the Poisson equation solution.

2.6 Temperature and bandgap relationship

Temperature affects the E_g of a material; this is an important parameter to consider as LWIR photodiode measurements are taken at low temperatures. The Varshni equation (2.29) which shows the relationship between E_g and temperature [10],

$$E_g(T) = E_g(0) - \frac{\alpha_g T^2}{\beta_g + T} \quad (2.26)$$

where $E_g(0)$ is E_g at 0 K and α_g and β_g are empirical constants for the material in question; α_g and β_g also change with the superlattice period. This means that one period design for a superlattice could be more dependent on temperature than another design. A high dependence on temperature would cause measurements of those samples to be more susceptible to fluctuations of temperature, especially if the wavelength of interest is close to the cutoff wavelength of the structure.

2.7 *PN and PIN photodiodes*

N junctions are the simplest form of photodiode. Photodiodes need a junction between oppositely charged regions; the n-type doped region has extra electrons compared to the number of bonds whilst the p-type doped region has a deficiency of electrons. When a bias is applied across the pn junction, a depletion region with high electric field at the interface of the two regions is formed. The depletion region is an area which has been depleted of its charge carriers by an applied electric field. When the photodiode is illuminated, photons are absorbed in the photodiode. The photons then excite electrons and if the energy is large enough they are promoted into the conduction band. The photo-generated carriers may diffuse to the depletion region of the junction, if they are generated outside the depletion region. When photons are absorbed within the depletion region the holes and electrons are separated by the electric field and accelerated through the depletion region to the oppositely charged region, producing an external current.

P-I-N doping is a common structure for photodiodes. In an ideal P-I-N photodiode, photons are absorbed in the intrinsic region of the photodiode (i-region) the generated electrons and holes diffuse towards the oppositely doped region. Applying a forward bias causes the depletion region width of the junction to reduce, because the forward bias causes majority carriers to move towards the oppositely charged material, this increases the diffusion current density. In the presence of reverse bias, the potential across the depletion region increases. Which increases the size of the depletion region and the diffusion current is caused by minority carriers diffusing towards the i-region. For example electrons in the p-region diffuse towards the i-region, then drift current happens in the i-region continuing the movement of electrons toward the n-region, depicted in Figure 2.4.

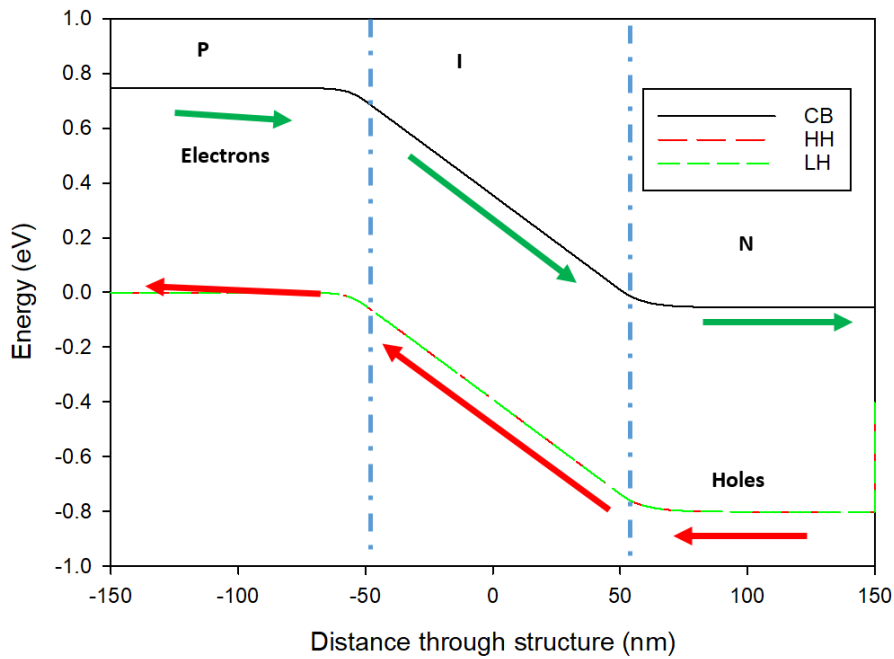


Figure 2.4: A diagram of the PIN structure band diagram and the flow of electrons and holes when reverse bias is applied.

The current-voltage characteristics of a photodiode change under illumination; this is shown in Figure 2.5, under illumination the reverse current of the photodiode increases. The reverse current increase under illumination is due to the incoming photons generating extra charge carriers and contributing to the drift current. The increase is largest for shorter wavelength light (red), as the energy of the incoming photons is larger and more of the carriers generated have enough energy to be promoted and contribute to the current, whereas the change in the forward current is much smaller.

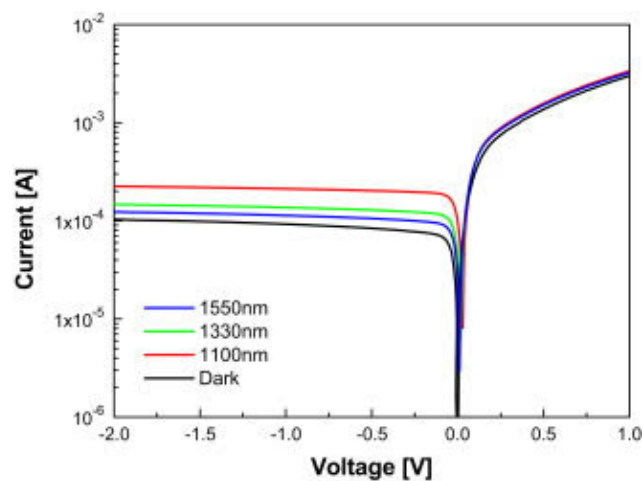


Figure 2.5: The current voltage results for an InAs PIN photodiode with bulk current characteristics under illumination at 3 different wavelengths

2.8 Dark current in photodiodes

The dark current of a photodiode is also a very important property for assessing the quality of a photodiode. Several of the dark current mechanisms depend on temperature similar to E_g . An ideal PIN photodiode has no depletion of carriers into the p and n type regions. The forward bias current can be fitted using (2.20) to establish the resistance of the diode (originating from metal contacts and/or epilayers) and the ideality factor of the photodiode. For a diffusion current dominated photodiode the ideality factor is 1, a generation-recombination dominated photodiode has an ideality factor of 2. The resistance for the metal contacts for a photodiode can also be separately calculated by a set of ohmic contact pads on the wafer with increasing distance between the pads, as pictured in Figure 2.5. By plotting the current at a set voltage against the distance between the metal contacts the resistance of the contacts can be extrapolated from the resistance at 0 nm distance. A good ohmic contact shows a resistance of $\sim 10 \Omega$ for a photodiode of diameter $420 \mu\text{m}$.

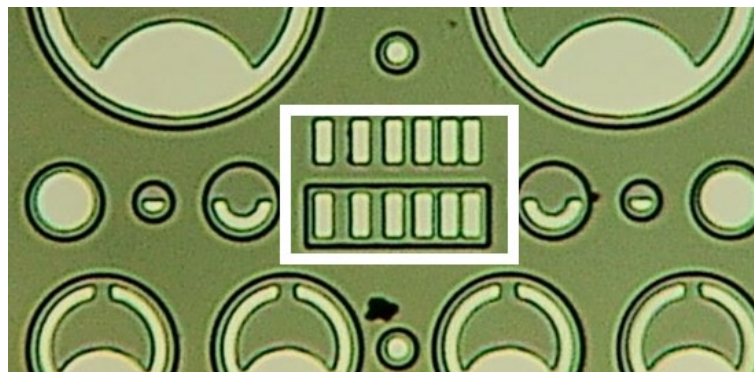


Figure 2.6: An image of the metal pads (red box) that can be included into photodiode device design used to calculate the resistance for the metal contacts of distances 5,10,15,20,25 μm .

The reverse bias current can give information about:

- The diffusion current,
- The generation–recombination current,
- The tunnelling currents
- The surface leakage of the photodiode.

The diffusion current

The diffusion current density has been discussed before as part of the nextnano++ current density calculation explanation in section 2.5.

Generation recombination current

The Generation recombination (G-R) current is a common form of current density and tends to dominate at low temperatures, so it is important to understand them as most T2SL measurements are done at 77 K. G-R currents can be from trap assisted recombination, where defects in the semiconductor will introduce extra energy levels inside the E_g of the material. G-R currents can also be band-to-band recombination, where the recombination is directly between the conduction band and valence band. It is described by the equation:

$$I_{G-R} = \frac{q n_i A_D W}{\tau_{eff}} \quad (2.27)$$

where q is the charge of an electron, n_i is the intrinsic carrier concentration, A_D is the area of the device, W is the depletion width and the effective carrier lifetime is τ_{eff} . The equation shows that the G-R current depends on the depletion width, which as discussed before increases with reverse bias.

Tunnelling current

Tunnelling current is of more importance for photodiodes made from materials with small E_g and VLWIR superlattice photodiodes which have very small E_g are particularly susceptible. Quantum electron tunnelling current happens when electrons do not obey the classical physics rule, overcoming the barrier by energy, but by tunnelling through the barriers into the conduction band. The tunnelling current, I_{tunn} , is described by the equation:

$$I_{tunn} = \frac{\sqrt{2m^*} q^3 E V A_D}{4\pi^2 \hbar^2 \sqrt{E_g}} \exp\left(-\frac{\alpha_T \sqrt{m^*} E_g^{1.5}}{q\hbar E}\right), \quad (2.28)$$

where E is the electric field, m^* is the electron effective mass and α_T is the tunnelling fitting parameter. The conduction and valence bands bend at high bias causing the likelihood of tunnelling occurring to increase.

Another main current contributor is drift current which was explained in section 2.5. Drift current is the current caused by electric fields. The majority carriers in each region, electrons in the n-type region and holes in the p-type region, flow through the material as determined by the electric field. The equation for the drift current density for electrons is below:

$$J_n = qn\mu_n E \quad \text{units: (Acm}^{-2}\text{)} \quad (2.29)$$

where n is the number of electrons per cubic centimetre, μ_n is the mobility of electrons ($\text{cm}^2\text{V}^{-1}\text{s}^{-1}$) and E is the applied electric field (Vcm^{-1}).

2.9 Barrier photodiodes current density behaviours

A barrier in a photodiode is a semiconductor material with a E_g larger than that of the other material. A photodiode with carrier blocking barrier exhibits IVs that look different from typical PIN current density measurements. The current densities of structures with barriers are typically lower than structures without a barrier [11,12]. However, structures with blocking barriers can block the flow of majority carriers, leading to lower current density in forward bias than the current density in the reverse bias as seen in Figure 2.6. The device in Figure 2.6 is an nBn structure with an n-region made up of 12 ML InAs_{0.59}Sb_{0.41}/35.5 ML InAs and a barrier region of 8.3 ML Al_{0.85}Ga_{0.15}As_{0.01}Sb_{0.99}/9.3 ML InAs measured at 77 K. The large E_g superlattice is used for the barrier and blocks both of the charge carriers reducing the current density at 0 V to $1 \times 10^{-7} \text{ Acm}^{-2}$.

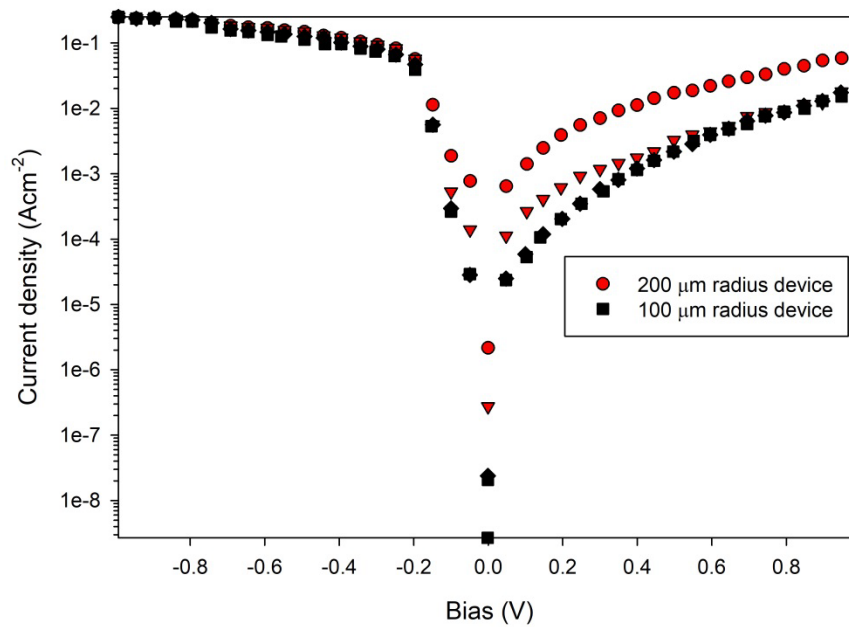


Figure 2.7: The current density voltage measurements of an nBn photodiode measured at 77 K

2.10 Infrared radiation from blackbody emitters

In this thesis the infrared signals from a blackbody emitter are used to test the photodetectors. In order to calculate the quantum efficiency of the photodetector, the power of light emitted by the blackbody emitter at set wavelengths and temperatures is required. The power of light radiated by the blackbody emitter is calculated by using Planck's law.

2.10.1 Planck's Law

All objects emit infrared radiation due to the temperature of the object. Planck's law is used to calculate the power per unit wavelength per unit area ($W(\lambda)$) of the radiation emitted from a perfect black body source.

$$W(\lambda) = \frac{2\pi c^2 h}{\lambda^5 (e^{(hc/\lambda k_B T_{BB})} - 1)} \quad (2.30)$$

where T_{BB} is the blackbody temperature and k_B is the Boltzmann constant

2.10.2 Wien's Displacement Law

Wien's displacement law of black body radiation is used to map how the black body spectrum of an object changes with temperature. The wavelength with the strongest spectral energy density is given by:

$$\lambda_{peak} = \frac{b}{T_{BB}} \quad (2.31)$$

where b is the Wien's displacement constant (2.898×10^{-3} mK).

2.10.3 Stefan-Boltzmann Law

The Stefan-Boltzmann law is used to give the total power emitted by a Black body emitter across all wavelengths. The Stefan-Boltzmann law is shown in equation (2.37)

$$E_\lambda = \sigma T_{BB}^4 \quad (2.32)$$

where σ is the Stefan-Boltzmann constant (5.6704×10^{-8} Wm⁻²K⁻⁴) and E_λ is the total energy emitted by the blackbody at all wavelengths. The Stefan-Boltzmann law is important as it is used to approximate the power of light the photodiode receives which is crucial to evaluate its performance.

2.11 Summary

In this chapter the theory and settings used in the nextnano++ simulations have been described. The wavefunction equations and k.p theory, used to solve the band structure of semiconductors, have been explained in section 2.1 and section 2.3. Section 2.2 explains the importance of periodic boundary conditions, which are used in all the cut-off wavelength simulations in this thesis. The periodic boundary conditions are an important tool for decreasing computational time, as it simulates an infinite superlattice. The relationship between temperature and bandgap is also explained. As superlattice detectors can be operated under different temperature conditions, how

the bandgap of a superlattice changes at different temperatures is very important. The dark current contributors for simulated and physical PN and PIN photodiodes have also been explored, this includes the recombination mechanisms. Finally the power of the infrared radiation for blackbody emitters is explained. These equations are applied in chapter 7 to calculate the power of the infrared radiation, from the black body emitter, reaching the photodiode device under testing.

References

-
- ¹ S. Birner, T. Zibold, et al. "nextnano: General Purpose 3-D Simulations," *IEEE Trans. Electron Dev.* 54, 2137 (2007)
- ² D. C. Rapaport, *The art of molecular dynamics simulation [electronic resource]*, 2nd ed. Cambridge, UK: Cambridge, UK, 2004.
- ³ I. Vurgaftman, J. R. Meyer, and L. R. Ram-Mohan, "Band parameters for III–V compound semiconductors and their alloys," *J Appl Phys*, vol. 89, pp. 5815-5875, 2001.
- ⁴ P. Y. Yu, M. Cardona, and Lu. J. Sham, "Fundamentals of Semiconductors: Physics and Materials Properties," *Phys. Today*, vol. 50, no. 11, pp. 76–77, 1997, doi: 10.1063/1.882012.
- ⁵ G. L. Bir and G. E. Pikus, *Symmetry and strain-induced effects in semiconductors*, vol. 624. Wiley New York, 1974.
- ⁶ Steenbergen, E.H. Strain-balanced InAs-InAsSb Type-II Superlattices on GaSb Substrates for Infrared Photodetector Applications. Ph.D. Thesis, Arizona state university, Tempe, AZ, USA, May 2012.
- ⁷ N. F. Johnson, H. Ehrenreich, P. M. Hui, and P. M. Young, "Electronic and optical properties of III-V and II-VI semiconductor superlattices," *Phys. Rev. B*, vol. 41, pp. 3655-3669, 02/15/ 1990.
- ⁸ P. T. Webster, "Growth, Optical Properties, and Optimization of Infrared Optoelectronic Materials," 2016.
- ⁹ K. Wong, G. Gopir, J. Hagon, and M. Jaros, "Absorption-Coefficient and Electric-Field-Induced Localization in InAs-AlGaSb Multiquantum-Well structures," *Semicond. Sci. Technol.*, vol. 9, no. 12, pp. 2210–2216, 1994, doi: 10.1088/0268-1242/9/12/008.
- ¹⁰ Y. P. Varshni, "Temperature dependence of the energy gap in semiconductors," *Physica*, vol. 34, no. 1, pp. 149–154, 1967, doi: 10.1016/0031-8914(67)90062-6.
- ¹¹ E. F. Schubert, Gessmann ,T. and Kim, J. K. , *Light emitting diodes*. Wiley Online Library: Wiley, 2005.
- ¹² M. Delmas, R. Rossignol, J.B. Rodriguez, and P. Christol, "Design of InAs/GaSb superlattice infrared barrier detectors," *Superlattices Microstruct*, vol. 104, pp.402-414, 2017/04/01/2017.

3 Simulation details and experimental methods

In this chapter the experimental procedures and simulation process details are described. Various characterisation techniques and the fabrication procedures for the photodiodes are also explained. Further details on the operating procedures of the parameters used for the nextnano simulations can be found in the appendix A [1]. The nextnano++ simulations in this thesis are aiming to find a superlattice design that has a:

- A LWIR cutoff wavelength
- Absorption coefficient greater 2000 cm^{-1} or higher than in the LWIR to be equivalent to InAs/InGaSb superlattice theoretical absorption coefficients [2].
- Current density in the order of $1 \times 10^{-5} \text{ Acm}^{-2}$ to keep the results on the same level of other published InAs/GaAsSb results [3]
- A quantum efficiency greater than 30 %, to line up with the typical values for InAs/GaAsSb superlattices [4].

3.1 Nextnano++ superlattice structure definition

Nextnano++ defines objects in reference to a grid system. This grid defines the points in the structure in the simulation. At each point energy levels are solved, using the Schrödinger equation and 8 band k.p theory. In this work a minimum of 3 grid points were used per monolayer. Increasing the number of grid points would improve the accuracy of the simulation, but also increase the computational simulation time.

A superlattice period was defined, by stating the size and position of the well and barrier, in reference to the edge of the simulated structure. For band structure and absorption simulations, a single period of the superlattice was defined and periodic boundaries were used to simulate an infinite superlattice. However, for current-density simulations a finite structure (all the periods defined in the simulation) with doping is needed. This is done by defining a well, then shifting the well by the length of the superlattice period and repeating the period by the number of periods in the structure.

Then the simulation can be used to calculate the current density and band structure of a finite superlattice. The valence band offset is an important parameter for the band structure calculations; usually it is defined as the position of the valence band edge in reference to the conduction band. However, in nextnano++ it is defined slightly differently the valence band offset is the average of the three valence bands (VBO_{av}), heavy hole, light hole and split-off. The nextnano++ definition of valence band offset is defined in (3.1),

$$VBO_{av} = \frac{(E_{hh} + E_{lh} + E_{so})}{\left(3 - \frac{2}{3}\delta_{cr}\right)} \quad (3.1)$$

where E_{hh} , E_{lh} , E_{so} are the energies of the heavy hole, light hole and split-off valence bands. δ_{cr} is the crystal-field splitting energy, defined as is the energy difference between two degenerate electron orbitals.

To define the doped part of a PIN structure, the charge is defined in each region of the structure and the type of dopant is named in the impurity section of the simulation. The carrier impurity energy of InAs is typically 0.001 eV [5]. In nextnano the impurity is defined as -1000 eV which is an unphysical large number used in nextnano++ to ensure full ionisation under all biases.

3.2 Nextnano++ current simulations

Figure 3.1 shows the flow of the Nextnano++ program when simulations include the current density calculations. The parts of the calculation that are unaffected by the bias applied to the sample are calculated before the current calculations. These include:

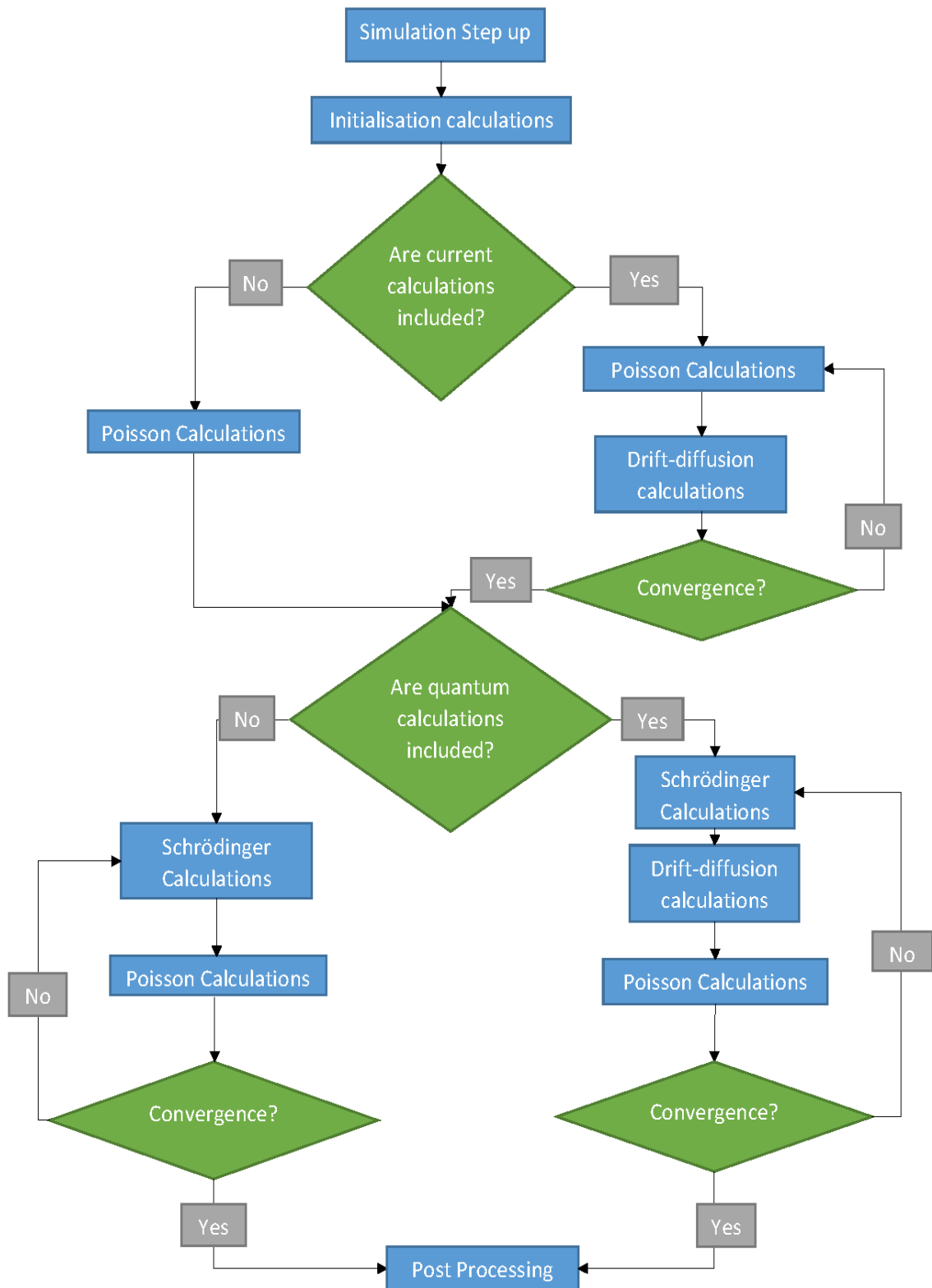
- Classical band structures
- Polarisation charges calculations
- Strain fields calculations
- Intrinsic density determination

In the simulation setup section the input file is checked for errors. In the Initiation calculations section the calculations not affected by the bias of the structures and the quantum calculations of the structures are performed. If current is included the Poisson equation, (2.27 repeated) coupled to the drift-diffusion equations is calculated until the answers converge over all biases.

$$\nabla^2 \phi = \frac{-\rho(x)}{\epsilon_0} \quad (2.27 \text{ repeated})$$

If quantum considerations are included, the Schrödinger equation runs through multiple iterations until the eigenfunction solutions to the Schrödinger equation converge. At the same time the Poisson equation calculations will run and converge on an answer. The number of iterations specified in the file is the number of times the Schrödinger equation is solved for a specific grid point. Next the current density drift-diffusion equations are calculated. The theory of the drift-diffusion equations is discussed in section 2.5. The quantum current calculations sections solve the Schrödinger equation; the drift-diffusion equation; and the Poisson equation all together. After

several iterations the current calculations converge and record the current-density at a set bias in the output file.



3.3 Optical calculations

The nextnano++ optical absorption calculations are computed after the quantum calculations. A key factor of the calculation is the polarisation direction of light must be specified. In this thesis the light was propagating in a direction normal to the quantum well. There are several parts of the optical absorption calculation these include:

- Polarised light
- The transition rate
- Interband transitions
- Density of states of the electron and holes

An in depth explanation on the optical calculation in nextnano++ can be found in the nextnano++ software documentation, and the thesis of Thomas Eißfeller [6].

The first parameter that needs to be calculated as part of the optics calculation is the dielectric tensor which is derived from susceptibility. Susceptibility describes the polarisation response of a dielectric material to an applied electric field. This is a very important parameter as the light used in the optics calculations is polarised therefore, the direction of the polarised light effects the absorption coefficient of the superlattice. The relationship between polarisation and electric field is written as

$$\hat{P} = \epsilon_0 \hat{\chi} \hat{E} \quad (3.2)$$

where \hat{E} is the electric field, $\hat{\chi}$ is the susceptibility and ϵ_0 is the electric permittivity of free space.

The absorption coefficient (α) of a material exposed to the polarised light is

$$\alpha = \frac{2\omega}{c} \kappa(\omega) \quad (3.3)$$

where c is the speed of light in a vacuum and ω is the angular frequency of the light, $\kappa(\omega)$ is the extinction coefficient in terms of angular frequency. The extinction coefficient can be calculated from the refractive index of the material. This means the absorption coefficient can be written in terms of refractive index (n_r) and relative dielectric constant (ϵ) in the form

$$\alpha = \frac{\omega}{n_r c} \epsilon^2(\omega) \quad (3.4)$$

The absorption coefficient at ω depends on the transition rate between the two states n and n' ($W_{n \rightarrow n'}$), the rate of an electron being excited from the initial energy level to the final energy level.

$$W_{n \rightarrow n'} = \frac{2\pi}{\hbar} |M|^2 g(\hbar\omega) \quad (3.5)$$

Where M is the 8×8 matrix from the 8 band k.p theory and $g(\hbar\omega) = g(E)$ is the density of states in the superlattice. For the 8 band k.p calculations M an 8×8 matrix is used to calculate interaction between the wave functions ψ_n and $\psi_{n'}$.

The density of states is needed to calculate the transition rate for the absorption calculations of interband transitions, the density of states is for the states from E to $E + dE$,

$$g(E) = g(k) \frac{dk}{dE} \quad (3.6)$$

where $g(k)$ is the density of states in k-space. For superlattices the density of states in a superlattice is proportional to $E_g^{1/2}$,

$$g(E) = \frac{1}{2\pi^2} \left(\frac{2\mu}{\hbar^2} \right)^{3/2} (E - E_g)^{1/2} \quad (3.7)$$

The density of states for superlattices is proportional to $E - E_g^{1/2}$ whereas the density of states for a quantum well is proportional to E_g^0 . This is because the density of states for a superlattice is not step-like as seen in discrete quantum wells nor is it the continuous curve seen in bulk material. The superlattice density of states is between the step-like density of states in quantum wells and the continuous density of states of bulk material due to the minibands of the superlattice.

3.4 *Sample fabrication*

The photodetectors in this thesis are grown by molecular beam epitaxy at the National Epitaxy Facility. The samples were fabricated in the clean rooms at Sheffield University. A cross-section of an ideal photodiode is shown in Figure 3.2. The total etch depth for the samples is 1300 nm, this is a relatively large etch depth for a photodiode.

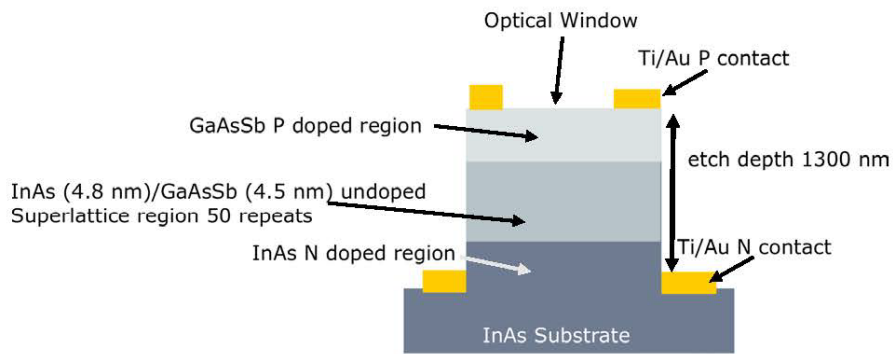


Figure 3.2: A cross section of the 110 μm photodetector devices in this thesis

The samples in this thesis were circular in design shown in Figure 3.3 with device radii of, 210 μm (A), 110 μm (B), 60 μm (C) and 35 μm (D). Ti/Au Top contacts were deposited to the p-region of the structure and a grid contact on the n region of the structure. To measure the samples in low temperature set-ups the sample was attached to a T0-5 header and ball bonded.

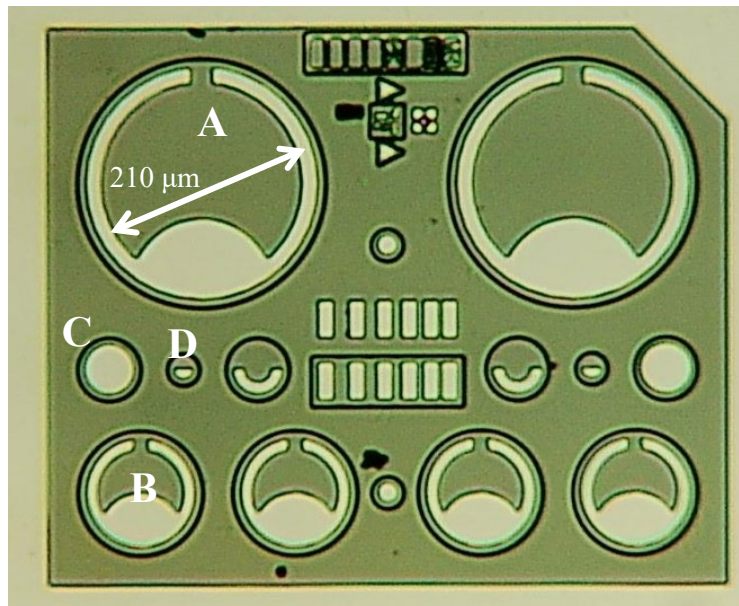


Figure 3.3: The image of the PIN device design and the radius of the devices, 210 μm (A), 110 μm (B), 60 μm (C) and 35 μm (D).

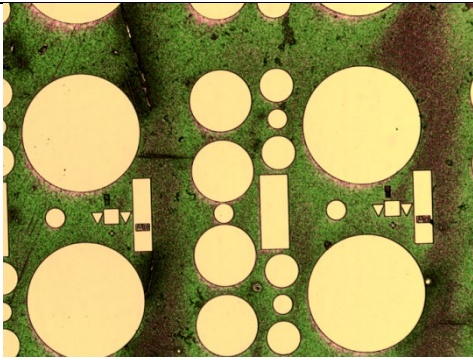
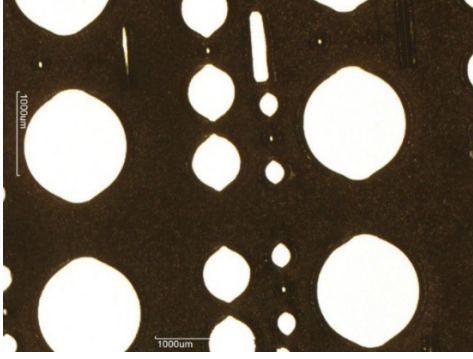
The sample is cleaved from the wafer with a diamond tipped stylus, the newly cleaved sample was then 3 staged cleaned using, N-butyl, acetone and IPA. N-butyl was heated and the sample was submerged in the liquid for 30 seconds. The sample is next dipped in acetone and finally the sample is dipped in IPA and blown dry with nitrogen. The sample is checked under the microscope and the 3 stage clean is repeated until the sample looks clean. A pattern for the top metal contacts was deposited using photolithography and (20 nm/200 nm) Titanium/Gold contacts are deposited by thermal evaporation. The sample was then cleaned and photolithography is used to pattern the device sizes on the sample. The sample was wet etched using a citric acid: Phosphoric acid: H_2O_2 : Deionised water (DIW) etch, the ratio 1:1:4:16. The etching solution was

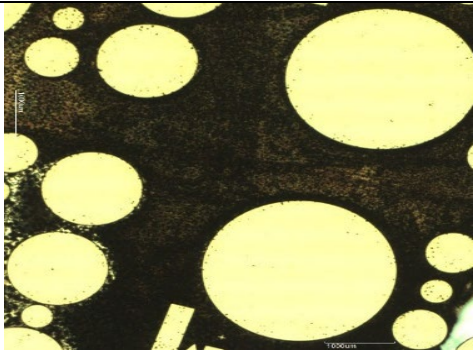
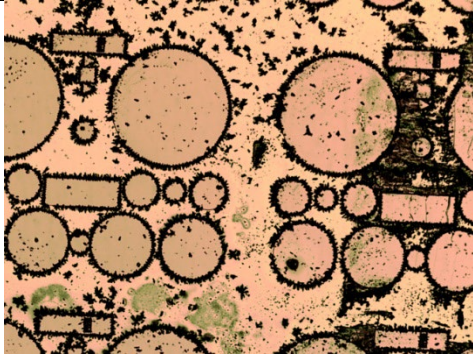
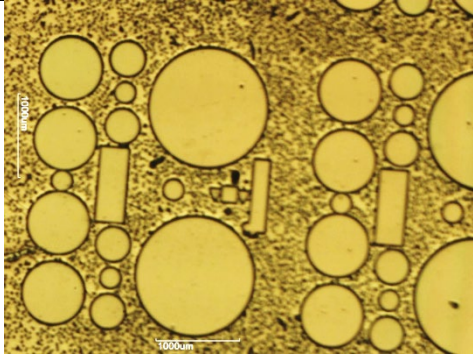
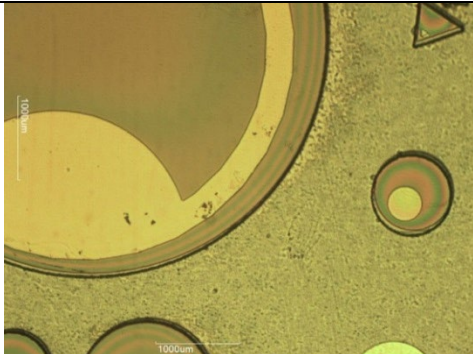
made up and stirred, then left for 5 mins for the sample etching rate to even out in the etching solution. The etch depth and profile was measured using a profilometer. After etching the sample to the correct depth the sample was cleaned and photolithography was used to pattern the sample for grid contacts. The Ti/Au (20 nm/200 nm) grid contacts were deposited on the sample by thermal evaporation. Finally the sample is then cleaned and the covered in Su8, except for the metal contacts, to stop the sample from oxidising when exposed to the air.

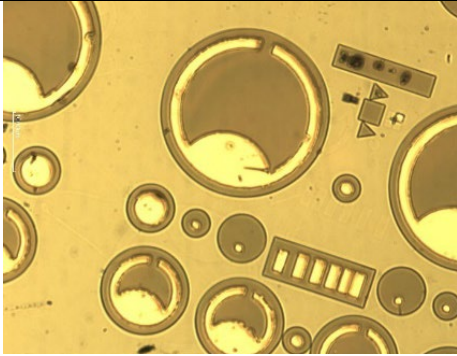
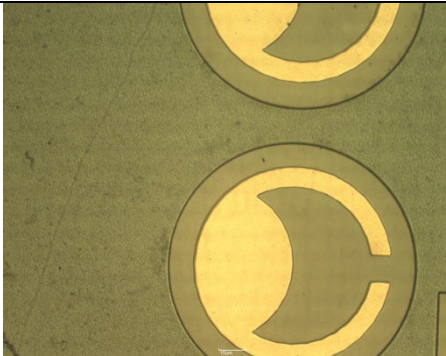
3.4.1 Etching Recipe investigations

The etching recipe used on a photodiode has a large effect on the quality of the photodiode, uneven etching across the sample can mean one device is better than another device. Etching recipes for superlattices containing Sb can be quite difficult as each layer of the superlattice will have a different etching rate which can lead to under cutting in the material. Several etching recipes were tried a brief description of the etching recipes are found in Table 3.1.

Table 3.1: Summary of superlattice etching recipes and the results

Etch Name	Recipe	Image of etch	Etch rate (nm/min)	Comments
A	Sulphuric acid: H ₂ O ₂ :DIW 1:8:80		N/A	The etch depth is unmeasurable, an oxide builds on the sample surface and the solution does not seem to etch at all.
B	Tartaric acid: HCl: H ₂ O ₂ 2.08:1:1.02 (10 g of tartaric acid dissolved in 14 ml of DIW)		576	Solution is cooled for 5 mins. Directional etch, causing the circular mesa to change shape, there is substance on the surface

Etch Name	Recipe	Image of etch	Etch rate (nm/min)	Comments
C	Phosphoric acid:H ₂ O ₂ 3:1		Unstable etch rate	The etching solution does not etch evenly and an oxide forms on the surface of the sample before the etch depth needed is reached. The Oxide is and etch stop.
D	Phosphoric acid: H ₂ O ₂ :DIW 1:1:1		427	An oxide forms mainly on the mesa sides, and the oxide on the mesa floor makes depositing grid contacts harder.
E	Phosphoric acid:H ₂ O ₂ : citric acid 3:1:2 11.6 g citric acid dissolved in 10 ml DIW		270	The sample etches unevenly, the oxide forms on the surface of the sample; this would make depositing grid contacts difficult.
F	Phosphoric acid: H ₂ O ₂ : DIW 1:1:2 Plus a 30 s finishing etch HCl: H ₂ O ₂ : DIW 1:1:4		900	The etch solution does not produce as much oxide the device floor is significantly cleaner making grid contact easier.

Etch Name	Recipe	Image of etch	Etch rate (nm/min)	Comments
G	citric acid: H ₂ O ₂ 40:1 citric acid 50 g in 100 ml		0.23	The etch solution is quite slow, but it does not produce the oxide on the sample where it etches. This etch is too slow to be practical
H	Citric acid: Phosphoric acid: H ₂ O ₂ : DIW 1:1:4:16		143	The etch solution not produce the oxide on the sample. This etch is a good speed for etching, the etch rate is very stable and predictable. This makes this is the best etch solution to use to etch these samples

As shown in Table 3.1 several etching solutions were trailed to find the best etching solution for the InAs/GaAs_{0.09}Sb_{0.91} superlattice. However as can be seen in Table 3.1 several of the etching recipes formed a coloured substance on the mesa floor of the diode and were not suitable. Etch A did not etch the sample a measurable depth even after 5 minutes, for this reason a different acid etching recipe was used. Etch B is unfortunately directional, this causes the circular devices of known sizes to be etched into ovals and almost etching the smallest device size away completely. This directionality means the size of the mesa is not known, affecting the current density calculations. The shape also means the top contact pattern will no longer fit on to the top of the mesas. Therefore etch solution B with tartaric acid was not used to etch the final samples. Etch recipes C and D formed a substance on the surface which seemed to block further etching and would also stop the deposition of the n contact onto the mesa floor. Energy-dispersive X-ray spectroscopy (EDX) was carried out on the etched samples to determine the composition of the substance; the spectrum of one sample can be seen in figure 3.4. The spectroscopy showed the

substance on the surface of the sample was made from phosphorus, oxygen and carbon. Therefore to stop the substance forming the citric acid was added to the solution (etch E).

Etch E still produces the oxide so the amount of phosphoric acid was reduced in etch F. Some improvement is seen in etch F compared to other recipes, however the oxide is still formed on the sample before the target etch depth is reached. To improve the etching recipe in order to achieve the etch depth of 1300 nm, the phosphoric acid was removed from the etch solution completely and the sample was etch with citric acid, H₂O₂ and DIW only (Etch G). Etch G gives a clean surface after etching, however etch G is too slow to be practical for the large etch depth needed. Etch recipe H aims for balance between speed and surface condition by including a small amount of phosphoric acid to speed up the etch rate. The phosphoric acid ratio used is smaller than the previous etch recipes (Citric acid: Phosphoric acid: H₂O₂: DIW 1:1:4:16). The higher ratio of H₂O₂ and DIW to acid, compared to previous etches, seems to keep the surface of the mesa floor cleaner. The surface is not completely clean but, clean enough to be able to deposit the n contact with strong adhesion. This etch recipe also seems to relatively stable at 143 nm/minute which makes fabrication easier as the timings are reliable and predictable.

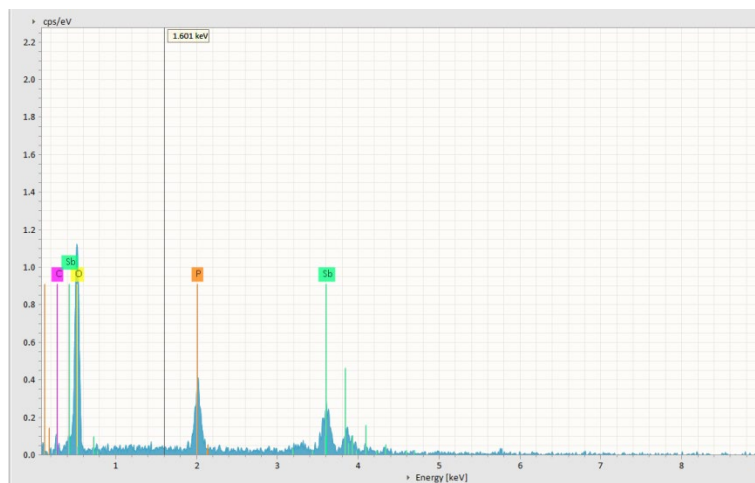


Figure 3.4: EDX results for the substance on the surface of mesa floor of the etched InAs/
GaAs_{0.09}Sb_{0.91} sample etched in etch recipe C.

3.5 Dark current measurements

3.5.1 Current – voltage measurements

One of the first characteristics tested for any photodiode, is the current voltage (I-V) characteristics. These results communicate information about the devices dark current, a low dark current leads to a good device. As the T2SL in this thesis have narrow bandgaps the I-V

measurements were taken at liquid nitrogen temperatures, to reduce the dark current contributions due the temperature of the room.

The unpackaged sample is placed in to a JANIS ST-500 liquid nitrogen vacuum chamber probe station. A flow of liquid nitrogen circulates under the vacuum pumped main chamber and using the cold finger plate the sample is cooled to 77 K. The forward and reverse bias current characteristics of the sample are then measured. The reverse bias characteristics indicate the dark current of the device, whereas the forward bias indicates the series resistance in the device. The JANIS ST-500 chamber has 2 probe tip arms with manipulators outside the chamber; these are used to make contact with the deposited gold contacts on the samples. A camera is used to assess the position of the probe tip as probing too hard or with a blunt or unclean probe tip can add series resistance to the measurements. One of the benefits to using the JANIS ST-500 probe station for I-V measurements is the sample does not need to be packaged and ball bonded. The process of ball bonding applies ultrasonic vibrations and downward force to the sample which can cause damage to the fragile semiconductor material the sample is made from.

Drift current is the main current expected in the reverse bias, it is caused by majority carriers flowing towards an area of low concentrations E_g electrons flow from n region to p-type region, as describes in section 2.8.

3.6 *Blackbody photoresponse measurements*

The photoresponse of the LWIR sample in this thesis was measured using a blackbody emitter. The sample was packaged and placed inside a dewar which then was cooled with liquid nitrogen.

3.6.1 *Operating a liquid nitrogen cooled cryostat dewar*

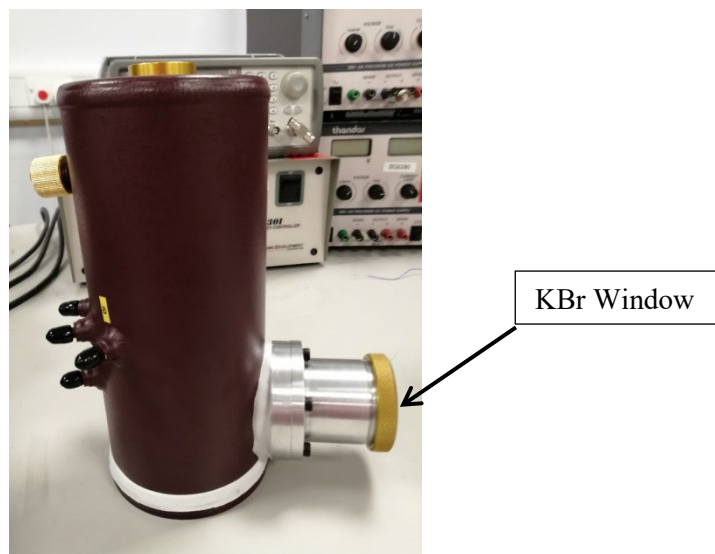


Figure 3.5: The liquid nitrogen dewar cryostat with KBr window fixed in front of the packaged device.

A sample packaged on a TO-5 header is placed into the sockets in the dewar, inside the screwed in section under the KBr window. The KBr window for the dewar was then fixed in place and sealed, so the dewar can be placed under vacuum. The pressure should be about 1×10^{-2} bar, the dewar can then be disconnected from the vacuum pump and will hold vacuum for several days.

The sample needs to be cooled slowly to avoid thermal cracking caused by the multiple layers of different materials in superlattices cooling down at different rates. To avoid thermal cracking, a small volume of liquid nitrogen into the top of the dewar, waiting four minutes before pouring more liquid nitrogen into the dewar.

3.6.2 Blackbody set up

The cooled dewar is then placed in front of a blackbody emitter as shown in Figure 3.4.

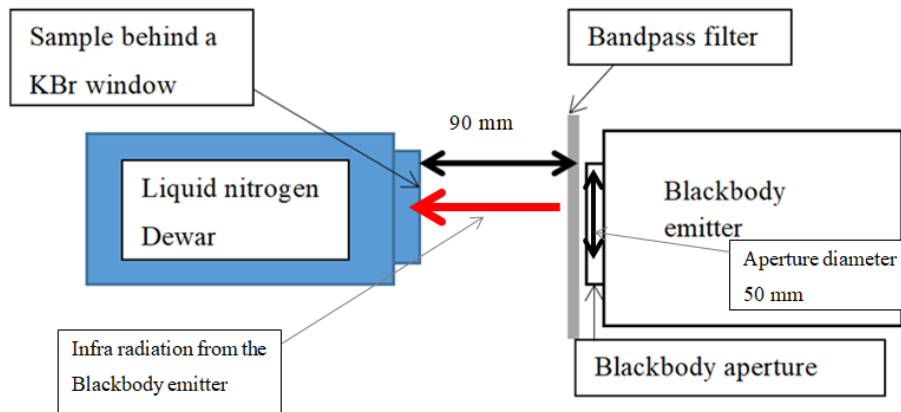


Figure 3.6 Diagram of the experimental set up for the spectral analysis for a package photodiode exposed to a blackbody emitter. With angle of incidence being 0° , a distance of 90 mm between the liquid nitrogen cooled photodiode and the blackbody emitter which has an aperture diameter of 50 mm.

The blackbody emitter, which had an aperture diameter size of 50 mm, was heated to 1000°C and the dewar was placed in front 90 mm away from the blackbody emitter. Infrared bandpass filters ranging from 3 to $15\ \mu\text{m}$ were placed in front of the blackbody emitter one at a time. The voltage on the lock-in amplifier caused by the change in photocurrent was recorded. From these results the photocurrent in each bandpass filter range is calculated.

The filters attenuated the blackbody signal differently so the percentage transmission of each filter was measured using an FTIR. The photocurrent results were normalized against the appropriate bandpass filter. The band pass filter with the highest transmission is the $15.9\ \mu\text{m}$ filter as can be seen in Figure 3.5.

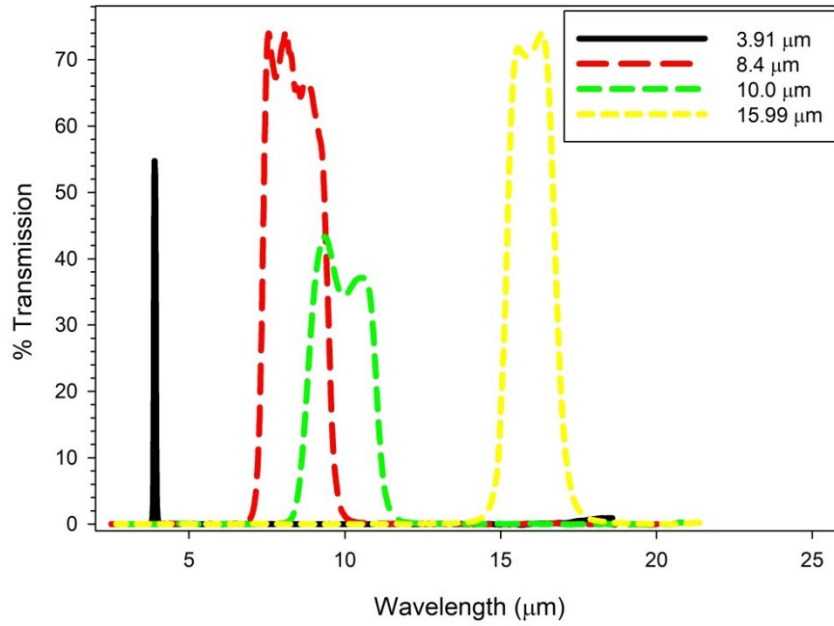


Figure 3.7: The transmission spectrum of the bandpass filters taken using an FTIR.

The theoretical photocurrent for a photodiode with 10 % external quantum efficiency was calculated using the equation below.

$$i_{ph} = \int_{\lambda_1}^{\lambda_2} R(\lambda)P(\lambda).d\lambda \quad (3.8)$$

$$R(\lambda) = \frac{\eta q}{hc} \quad (3.9)$$

where q η is the quantum efficiency of the device. The power of the signal at wavelength, $P(\lambda)$ is calculated using,

$$P(\lambda) = F.W(\lambda)\sin^2\left(\frac{\theta}{2}\right)A.M_F.T_F.\cos(\varphi) \quad (3.10)$$

where φ is the angle of incidence, T_F is the transmission factor, about 1 in air over a short distance. A is the Area of the photodiode, F is the magnification provided by lens, this equals 1 as one was not used and M_F is the chopper modulation factor. θ is the optical field of view is defined as $\theta = 2 \tan^{-1}\left(\frac{\rho}{D}\right)$, D is the distance between the blackbody and the device and ρ is the diameter of the aperture opening of the blackbody source.

Planck's law is used to calculate $W(\lambda)$, the power per unit wavelength per unit area of the emitted radiation,

$$W(\lambda) = \frac{2\pi c^2 h}{\lambda^5 (e^{\left(\frac{hc}{\lambda k_b T_{BB}}\right)} - 1)} \quad (3.11)$$

T_{BB} is the blackbody temperature and k_b is the Boltzmann constant and λ is the wavelength of the light. Though, this law assumes a perfect blackbody, with perfect emissivity across all wavelengths from the irradiating object. The blackbody spectrum calculated using the equations above and assuming the photodiode has a 10 % quantum efficiency is shown in Figure 7.10.

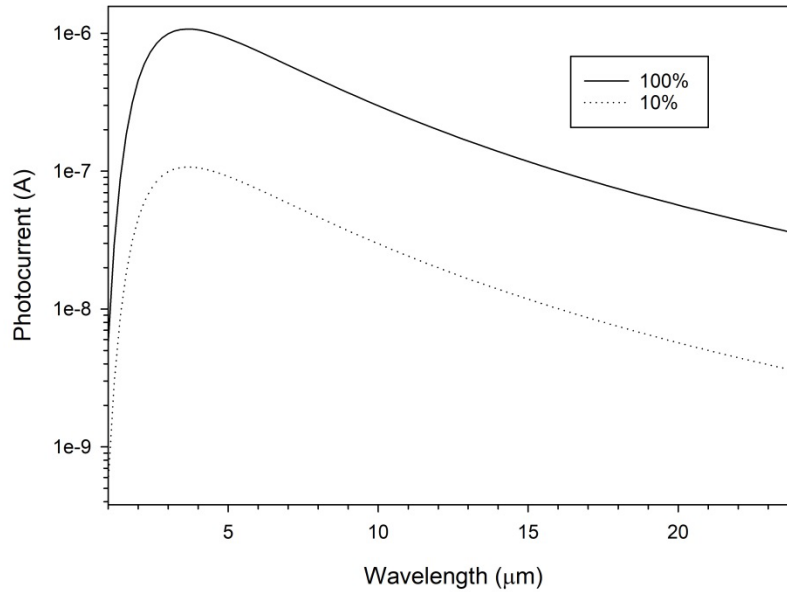


Figure 3.8: Photo spectrum of a photodiode with 100 % external quantum efficiency and the theoretical photocurrent of a 10 % external quantum efficiency photodiode exposed to a blackbody emitter at 1000 °C.

References

- ¹ S. Birner, T. Zibold, et al. "nextnano: General Purpose 3-D Simulations," *IEEE Trans. Electron Dev.* 54, 2137 (2007)
- ² C. H. Grein, M. E. Flatte and H. Ehrenreich, "Comparison of ideal InAs-InAs_{1-x}Sb_x and InAs-In_xGa_{1-x}Sb superlattice IR detectors," in *Proc. of the Third International Symposium on Long Wavelength Infrared Detectors and Arrays: Physics and Applications III*, pp. 211-18, 1995.
- ³ F. Wang, J. Chen, Z. Xu, Y. Zhou, and L. He, "InAs-based InAs/GaAsSb type-II superlattices: Growth and characterization," *J. Cryst. Growth*, vol. 416, pp. 130-133, 2015/04/15/ 2015.
- ⁴ M. Huang, J. Chen, J. Xu, F. Wang, Z. Xu, and L. He, "ICP etching for InAs-based InAs/GaAsSb superlattice long wavelength infrared detectors," *Infrared Phys Technol*, vol. 90, pp. 110-114, 2018/05/01/ 2018.
- ⁵ <http://www.ioffe.ru/SVA/NSM/Semicond/InAs/bandstr.html#Donors> last accessed 15/01/2022
- ⁶ Thomas Eißfeller, *Linear Optical Response of Semiconductor Nanodevices*, Technische Universität München (2008)

4 Design of lattice-matched InAs/GaAs_{0.09}Sb_{0.91} type II superlattice photodetectors

4.1 Introduction

Conventional Type II superlattices (T2SLs) have alternating thin layers of InAs and In_{1-x}Ga_xSb where the thickness of the layers, and the x-composition, are adjusted to achieve the desired cutoff wavelength. In general to achieve a longer cutoff wavelength a thicker InAs layer, or a higher x-composition, can be used. Strain-balancing becomes increasingly more challenging as InAs layer thickness increases or as the x-composition increases. This causes a significant challenge in obtaining the high number of high quality T2SL periods required to achieve high absorption efficiency in the VLWIR wavelengths.

This chapter explores the design of a T2SL photodetector using InAs and lattice-matched GaAs_{0.09}Sb_{0.91} (referred to as GaAsSb in this thesis). In principle this can be strain free, so that complicated strain-balancing schemes at the interface are not required (for example inserting InSb monolayers at the InAs and GaSb interfaces between InAs /GaSb superlattices) [1]. Additionally the layer thickness is not limited by critical thickness, so that thick layers can be grown without generating an excessive level of defects [2].

Benefits of lattice matched InAs/GaAsSb T2SL include:

- Freedom in thickness of InAs and GaAsSb, where the thicker periods can be grown without the strain causing defects like dislocations.
- A higher number of periods can be grown for the same reason, leading to thicker absorption regions and potentially higher Quantum Efficiency (QE).
- Higher growth temperature, with potential to use MOVPE, because there is no requirement for InSb interface. InAs/GaAsSb T2SL, grown at 480 °C with high crystal quality and reduced defects, has been reported [3].
- MOVPE growth is cheaper than other growth mechanisms and has the potential to be easily scaled up for commercial growth.
- Use of InAs substrate which has better transmission in LWIR [4].

Early evidence of progress in InAs/GaAsSb includes:

- It has been shown that InAs/GaAsSb superlattice structures have a dark current density an order of magnitude lower than an InAs/GaSb superlattice with the same cutoff wavelength, λ_c [5].
- The photoluminescence intensity for InAs/GaAsSb is also shown to be higher at various temperatures than an InAs/InSb/GaSb superlattice [6].

- A QE of 57.9 % at 15 μm has been achieved for the long wavelength infrared range which is comparable to the QE to other superlattice structures [3,7].

In this Chapter simulations for the λ_c and effective bandgaps of the InAs/GaAsSb T2SL structures are reported. The effective bandgaps and λ_c of 75 T2SL structures were modelled, giving a thorough representation of the trend in the structures. This is significantly more comprehensive than typical reported studies that explore less than 10 structures [8, 5].

The key findings in this chapter are:

- Cutoff wavelength simulations of various InAs/GaAsSb superlattice structures show a range of cutoff wavelengths in MWIR, LWIR and VLWIR can be achieved.
- λ_c shows a stronger dependence on thickness of the InAs well.
- The absorption coefficients of InAs/GaAsSb superlattices have been simulated. Designs with similar thicknesses of InAs and GaAsSb layers (symmetrical superlattice) have higher absorption coefficients when compared to asymmetrical superlattice designs with the same cutoff wavelength.
- When comparing designs with the same cutoff wavelengths, the wavefunction overlap between E1 (electron ground state energy level) and HH1 (heavy hole ground state energy level) is larger in T2SL with symmetrical designs.

4.2 Model details and verification

The software used for the simulations is called nextnano++ [9]. The parameters for InAs and GaAsSb, used in the simulations, are provided in appendix A. This software uses 8 band k.p theory to solve the Schrodinger, Poisson and current equations using periodic boundaries. The “pseudomorphic_strain” model, which applies strain in all directions of the superlattice, successfully reproduces theoretical and experimental results for InAs/GaAsSb superlattice structures. The simulations calculate the energy levels of the superlattice by solving the Schrodinger equation at each of the 500 grid points spread evenly over the superlattice period. To define the effective bandgap of the superlattice, the transition between the highest energy level in the valence heavy hole band (HH1) and the lowest energy level in the conduction band (E1) is recorded. The bandgap results were used to calculate the cutoff wavelength, so the results quoted in this chapter are plotted against the cutoff wavelength from literature.

Simulated bandgap values were benchmarked against the published results in [10,11]. The ternary materials parameters are interpolated from the binary materials that make up the ternary materials, such as GaAsSb which is interpolated from GaAs and GaSb. This strain approximation was applied to all superlattice structures including the lattice matched structures. The simulation then used the 8 band k.p theory to solve Schrodinger’s equation for the structure.

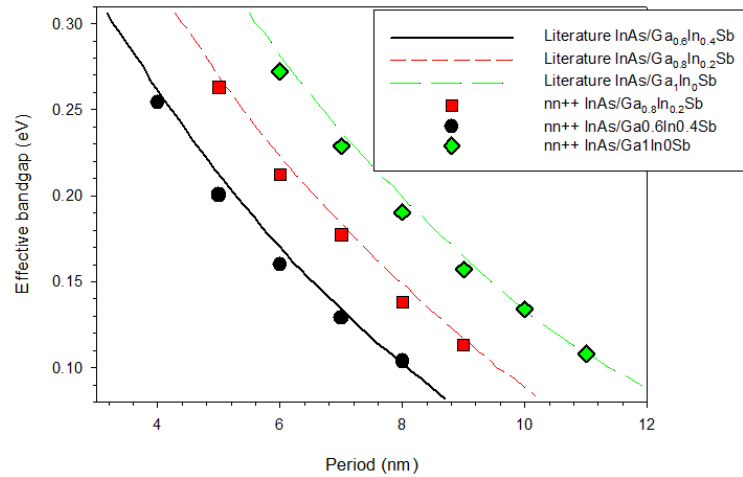


Figure 4.1: Effective bandgap of InAs/Ga_xIn_{1-x}Sb symmetrical period with increasing period size at 77 K with differing In percentage in the ternary material. Comparing 8 k·p simulated results with Lackner et al.[10] to nextnano++ simulation results using the default parameters for nextnano++ results.

The simulated effective bandgap results in Figure 4.1 at 77 K agree with the theoretical results presented by Lackner et al. [10] for superlattices of InAs/Ga_xIn_{1-x}Sb with varying percentages of Ga (from $x = 0.6$ to 1.0). The small discrepancy in Figure 4.1 has been attributed to differences in the material parameters used in the simulations.

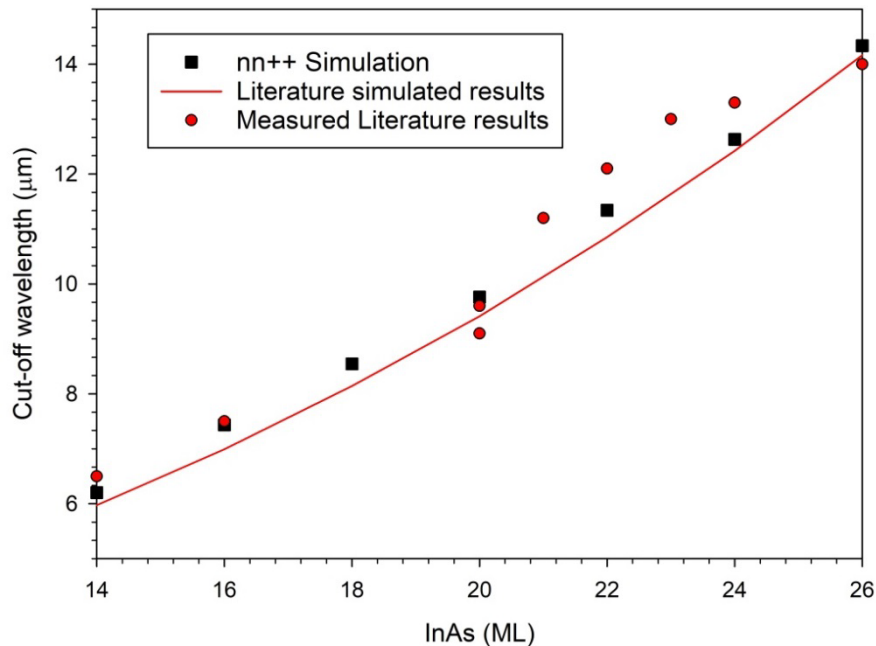


Figure 4.2: The cutoff wavelength of an InAs/GaAs_{0.09}Sb_{0.91} superlattice with 7 ML GaAsSb barrier with increasing size InAs well at 77 K, compared to the measured literature results and the 8 k·p simulated results from Wang et al. 2015 [11] to nextnano++.

Having verified the accuracy of the model using the InAs/Ga_xIn_{1-x}Sb T2SL, the model was used to calculate the bandgaps for the InAs/GaAsSb T2SL. The simulated results at 77 K are in good agreement with reported simulated and experimental results [11], as shown in Figure 4.2. These

structures have a GaAsSb barrier size of 7 ML with increasing InAs well widths from 14 to 26 ML.

In addition to the cutoff wavelength, the absorption coefficients were simulated. The absorption calculations used the smallest transition of 1 meV, any transition of this energy or larger were calculated. They are required to calculate the absorption efficiency of the T2SL photodetector. As before a benchmarking exercise was carried out. Two InAs/ Ga_{0.6}In_{0.4}Sb symmetrical superlattice structures with cutoff wavelengths in LWIR [12,13] were simulated in Figure 4.3. The simulation results have good agreement especially for the 10 ML/10 ML design at wavelengths larger than 12 μm and wavelengths shorter than 10.8 μm.

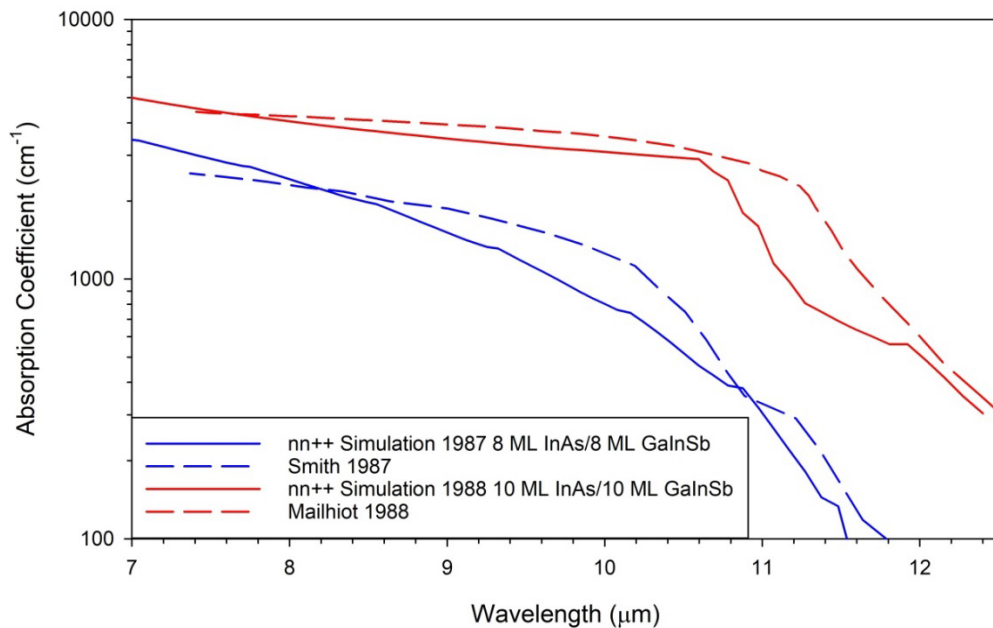


Figure 4.3: Simulation absorption coefficient results for symmetrical InAs/GaInSb superlattices compared to literature result [12,13]

A Short Wavelength Infrared (SWIR) In_{0.53}Ga_{0.47}As/GaAs_{0.51}Sb_{0.49} T2SL [14] was also used for benchmarking the absorption coefficient simulations. Figure 4.4 shows the comparison between simulated and published absorption coefficients. The simulated results agree with the literature showing steps in the spectrum which correspond to the transitions between the electron and hole energy levels. The results are in good agreement with the literature.

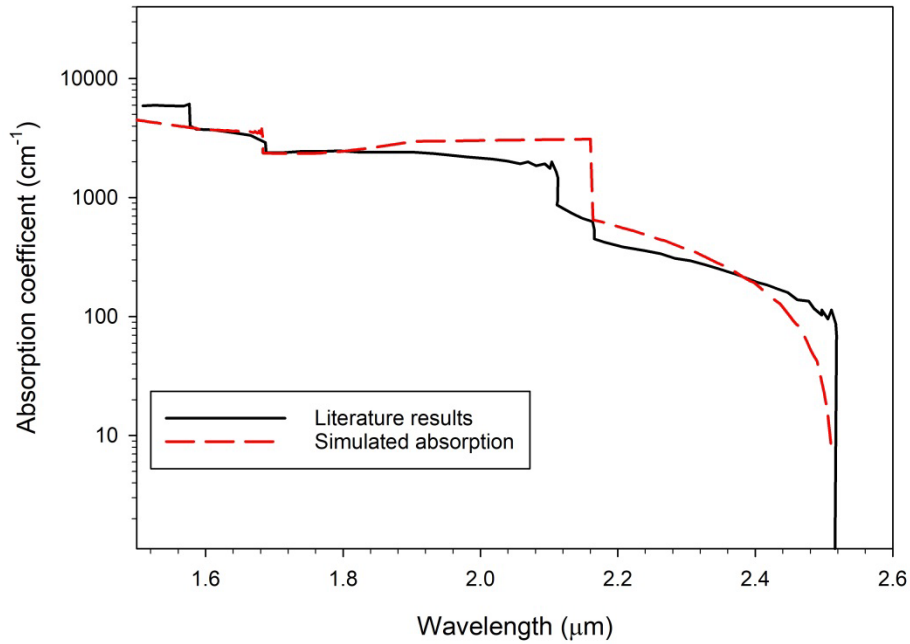


Figure 4.4: $\text{In}_{0.53}\text{Ga}_{0.47}\text{As}$ 5 nm / $\text{GaAs}_{0.51}\text{Sb}_{0.49}$ 5nm SWIR T2SL at 300 K [14]

The light used in the simulation is x-polarised light. This means the light simulated has values in the perpendicular direction to the direction of travel, the direction of growth, the light has magnitude in the magnetic field direction. Figure 4.5 gives a visual representation of the effect of polarisation on light travelling through a polarisation filter.

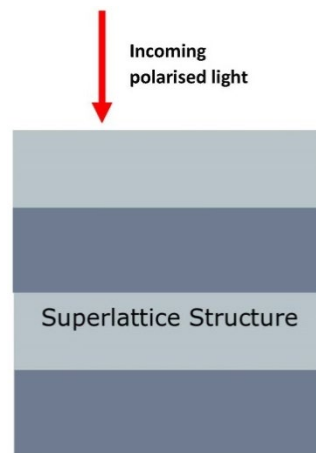


Figure 4.5: A diagram polarised light entering the simulated superlattice structure.

4.3 Simulated Results

4.3.1 Cutoff wavelength

The model was then used to explore a wider range of InAs/GaAsSb designs. A total of 75 different InAs/GaAsSb superlattice designs were simulated, covering InAs thicknesses from 7 to

26 ML and GaAsSb thicknesses from 7 to 20 ML. Simulated cutoff wavelengths at 77 and 300 K are summarised in Figure 4.6.

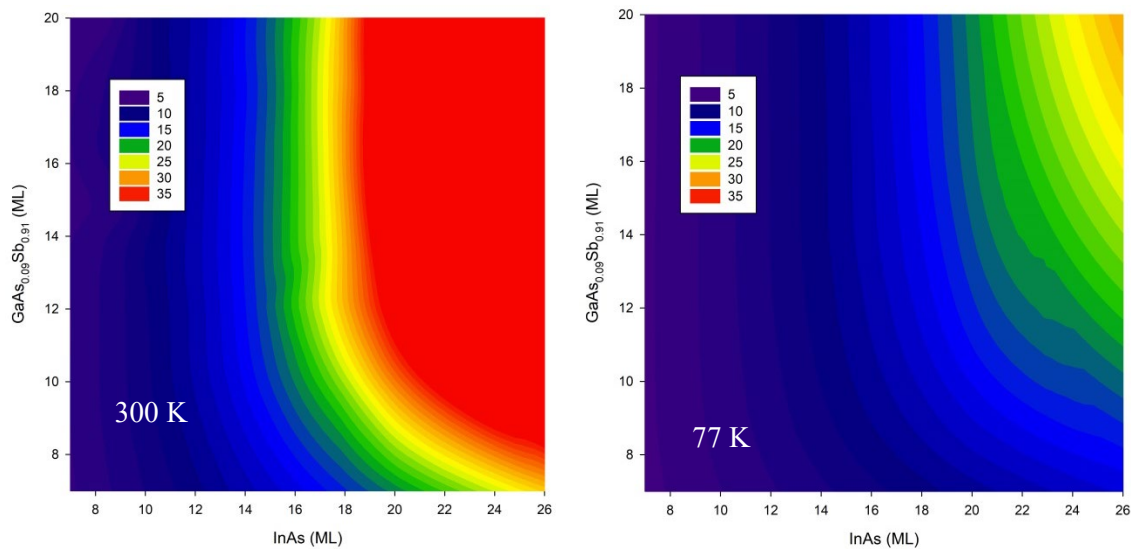


Figure 4.6: The cutoff in (μm) of InAs/GaAsSb with different superlattice periods at 300 K (left) and 77 K (right) Where the red areas represent cutoff wavelengths of over 25 μm or longer.

Key notable observations are.

- 1) In general, for a given InAs/GaAsSb design, the cutoff wavelength at 300 K is longer than that at 77 K.
- 2) The cutoff wavelength has a weak dependence on the thickness of the GaAsSb barrier layer.
- 3) Cutoff wavelengths from MWIR to VLWIR can be achieved.

The results in Figure 4.6 show that there is a range of InAs/GaAsSb designs that can be adopted to achieve MWIR, LWIR and VLWIR cutoff wavelengths. At 77 K, a structure with an InAs well width of 7-14 ML and a GaAsSb barrier width from 7-20 ML achieves MWIR. The LWIR is achieved in the light blue region. For example $\lambda_c = 10 \mu\text{m}$ is achieved with InAs well width from 16 ML with any thickness of GaAsSb barrier, from 10-20 ML. The teal to red regions represents the VLWIR, $\lambda_c > 14 \mu\text{m}$ were achieved with InAs layers of thickness > 17 ML and a GaAsSb layer > 14 ML. For example structures with InAs well width of 20 ML achieve $\lambda_c > 14 \mu\text{m}$ with GaAsSb barrier widths > 10 ML.

It can also be seen in Figure 4.6 that the cutoff wavelength has a weak dependence on the thickness of GaAsSb. For example, for designs with 7 ML of InAs and at 300 K, changing the GaAsSb thickness from 7 to 20 ML produces only 0.11 μm change in cutoff wavelength. In contrast, when GaAsSb is fixed at 7 ML, changing InAs layer from 7 to 26 ML produces a change

in cutoff wavelength of 21.35 μm , this is clearly displayed in Figure 4.7. A similar trend is observed from the results at 77 K.

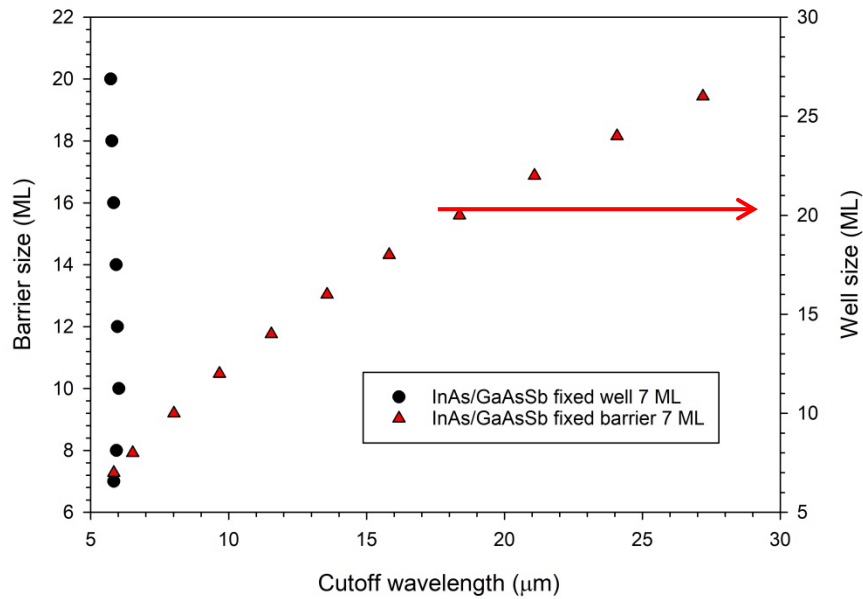


Figure 4.7: The cutoff wavelength of InAs/ GaAsSb superlattice structures at 300 K with a fixed barrier width of 7 ML GaAsSb with different InAs well widths (blue), and a fixed well width of 7 ML InAs with different GaAsSb barrier widths (black).

To analyse the dependence on InAs layer thickness, wavefunctions of three structures are presented in Figure 4.8. The band edges (conduction band (CB), heavy hole (HH) and light hole (LH)), energy levels (E1 and HH1) and wave functions are plotted. As the InAs well increases from 7 to 20 ML, the energy level of E1 lowers from 0.14 eV to 0.01 eV, and hence increases the λ_c , from 4.7 to 17 μm . The energy level of HH1 is unchanged as the barrier width is constant. A similar effect is seen if the well is fixed to 7 ML and the barrier is increased from 7 to 20 ML, the energy level of HH1 has increased from -0.12 eV to -0.04 eV, causing λ_c to increase from 4.7 to 5.8 μm . The results show that increasing the InAs well width from 7 to 20 ML produces a larger increase of the cutoff wavelength (4.7 to 17 μm), compared to only a much smaller increase (4.7 to 5.8 μm) when the GaAsSb barrier width is increased over the same range.

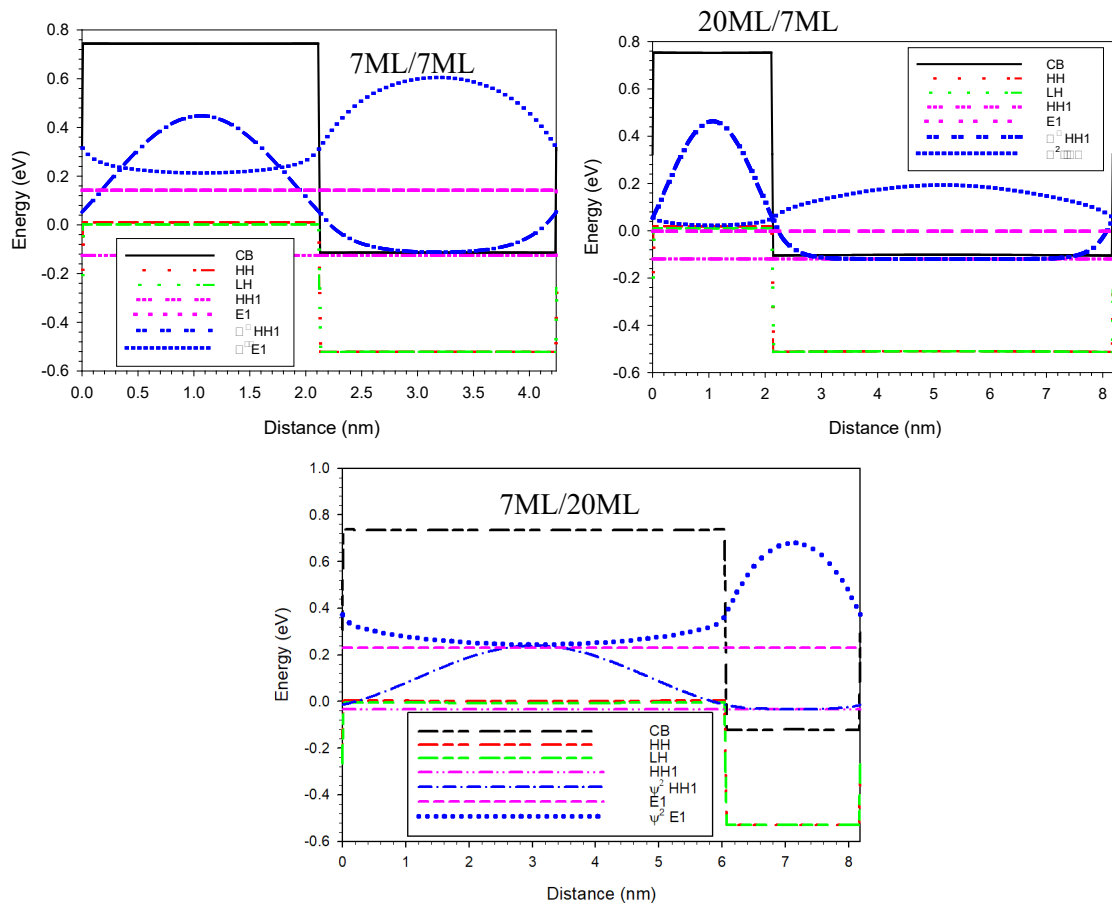


Figure 4.8: The energy levels, band edges and wavefunction squared at 77 K of a 7 ML InAs/7 ML GaAsSb barrier (top left) a 20 ML InAs well/7 ML GaAsSb barrier (top right) and a 7 ML InAs well/20 ML GaAsSb barrier (middle bottom).

4.3.2 Absorption coefficients

The absorption coefficient of a structure is a very important property to consider when choosing a superlattice structure. The absorption coefficient of the InAs/GaAsSb structures at the wavelengths of 5 μm , 10 μm and 15 μm are shown in Figure 4.9.

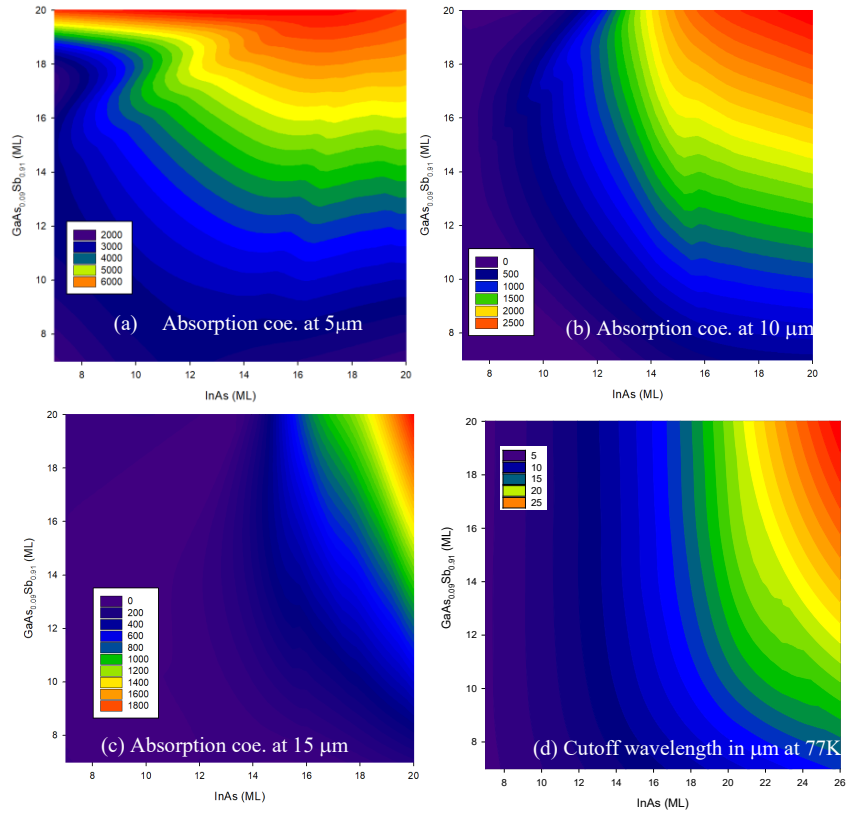


Figure 4.9: The absorption coefficient (cm^{-1}) at 5 μm (a), 10 μm (b) and 15 μm (c) for superlattices of various InAs/GaAsSb structures at 77 K. The cutoff wavelengths are shown in (d).

Key notable observations are.

- 1) For any given design the absorption coefficient is higher at the shorter wavelength range.
- 2) The design option to achieve high absorption coefficient at VLWIR is much more limited than at MWIR.
- 3) In general, when comparing designs with the same cutoff wavelength, symmetrical designs (similar InAs and GaAsSb widths) have higher absorption coefficients.

The absorption coefficients for a wide range of InAs/GaAsSb designs were simulated and shown in Figure 4.9. For comparison typical InAs/GaSb T2SL absorption coefficients are reported to be in the 1500-2500 cm^{-1} range for the MWIR and $> 1000 \text{ cm}^{-1}$ for the LWIR [15]. The results simulated absorption coefficient for the LWIR structure with 16 ML InAs/10 ML GaAsSb is 273 cm^{-1} , which is lower than that reported for InAs/GaSb T2SL.

Figure 4.9 (a) shows the absorption coefficient at 5 μm . The highest absorption coefficients are obtained when the GaAsSb layer is large. For designs with 20 ML of GaAsSb, the absorption coefficient is high $> 6000 \text{ cm}^{-1}$ and the variation is small at 5 μm for InAs thickness of 7-20 ML although the cutoff wavelength varies from MWIR to VLWIR as the thickness of InAs layer increases.

At 10 μm , the number of designs that can produce high absorption coefficients, above 2500 cm^{-1} (red zone), is smaller as shown by those in the top right corner of Figure 4.9(b). In general the absorption coefficient is highest for designs with the larger periods, >18 ML InAs, as these superlattices have longer cutoff wavelengths than 10 μm . For example the design with 18 ML InAs/20 ML GaAsSb has a higher absorption coefficient of 2350 cm^{-1} than a design with 16 ML InAs/16 ML GaAsSb which has an absorption coefficient of 1980 cm^{-1} .

Figure 4.10 suggests that for designs with similar cutoff wavelength, 10.3 μm , a more symmetrical period design (16 ML InAs/10 ML GaAsSb) yields a higher absorption coefficient of 273 cm^{-1} than that of 20 ML InAs/7 ML GaAsSb yields an absorption coefficient of 27 cm^{-1} . Similar trend is observed at longer wavelengths. For structures with a cutoff wavelength of 12.4 μm the almost symmetrical design (17 ML InAs/ 16 ML GaAsSb) yields a higher absorption coefficient at 10 μm of 200.4 cm^{-1} than that of 26 ML InAs /7 ML GaAsSb yields a absorption coefficient of 30.2 cm^{-1} . Designs with InAs thickness below 12 ML have zero absorption coefficient as their bandgap energies are larger than the photon energy at the 10 μm wavelength. Therefore T2SL LWIR structures with similar thicknesses of InAs and GaAsSb produce higher absorption coefficients.

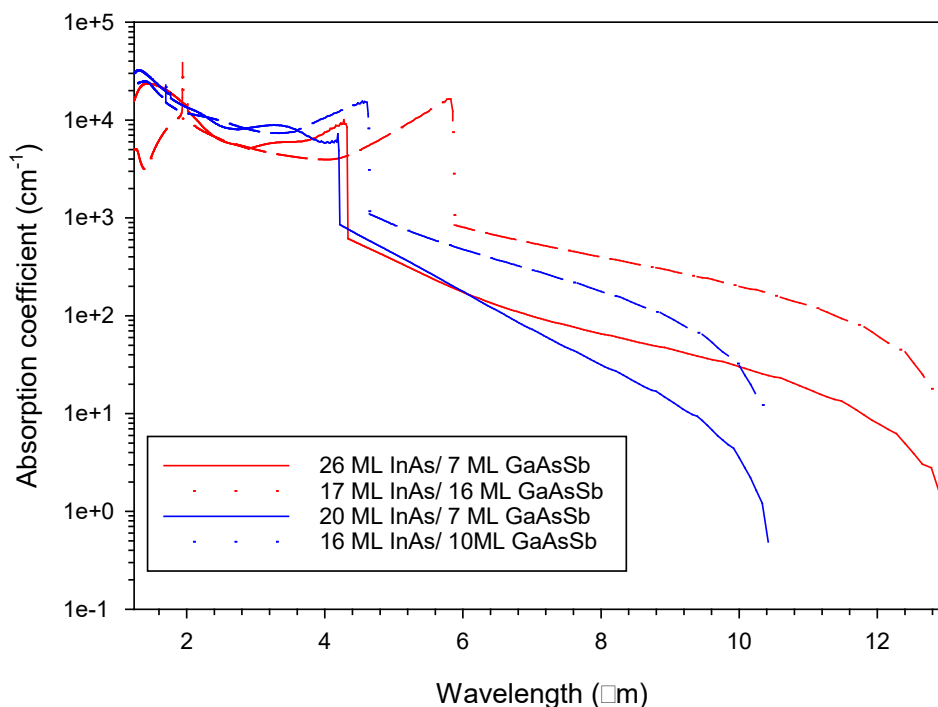


Figure 4.10: Absorption spectrums of two sets of InAs/GaAsSb superlattice structures with similar cutoff wavelengths at 77 K, red have a cut off wavelength of 12.4 μm and the blue structures have a cutoff wavelength of 10.3 μm .

he trend in the VLWIR is shown in Figure 4.9(c). The number of designs capable of producing absorption coefficient $>1800\text{ cm}^{-1}$ at 15 μm is even smaller. It is therefore clear that design

flexibility is much more restricted for detection of VLWIR at 15 μm . As before symmetrical design produces a higher absorption coefficient. For example, a symmetrical period design (18 ML InAs/18 ML GaAsSb) yields a higher absorption coefficient than 20 ML InAs/12 ML GaAsSb, decreasing from 1000 cm^{-1} to 600 cm^{-1} . The variation of the absorption coefficient becomes larger and more heavily dependent on the design at longer wavelengths.

4.3.3 Wavefunction overlap

To understand the trends observed for the absorption coefficients, the wavefunction overlaps for various designs are analysed. Key notable observations are.

- 1) At a given cutoff wavelength, symmetrical designs have larger wavefunction overlaps than asymmetrical designs.
- 2) In T2SL structures for a fixed InAs well width of 7 ML, the percentage of E1 and HH1 wavefunctions inside the InAs well decreases, with increasing GaAsSb barrier width.

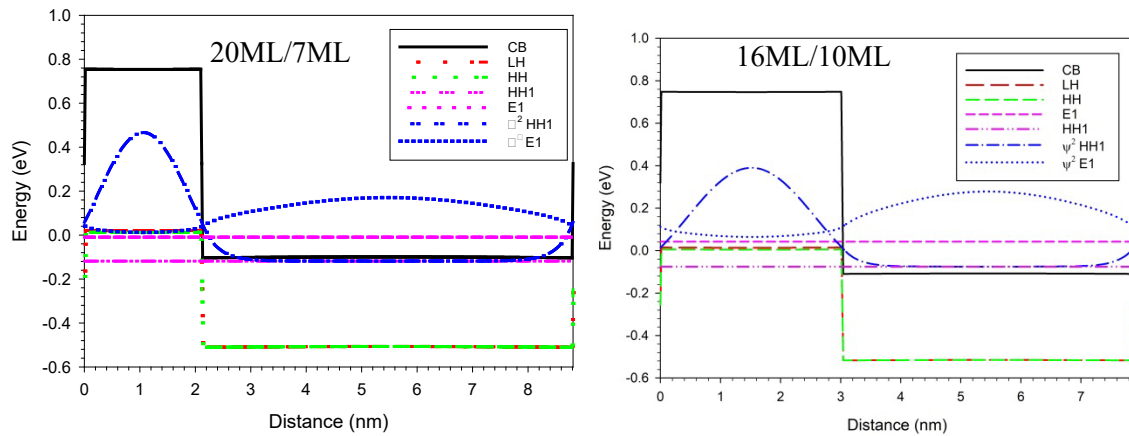


Figure 4.11: (left) Wavefunctions of 20 ML InAs and 7 ML GaAsSb structure (right) Wavefunctions of 16 ML InAs and 10 ML GaAsSb structure

It is constructive to analyse the wavefunctions for symmetrical and asymmetrical T2SL designs to understand the stronger absorption coefficients in the former design. The wavefunctions overlap determines the probability of the energy transition between E1 and HH1. Figure 4.11 shows the comparison between two superlattice designs with the same cutoff wavelength of 10.3 μm , a more symmetrical design (16 ML InAs/10 ML GaAsSb) and an asymmetrical design (20 ML InAs/7 ML GaAsSb). The results show that the symmetrical design has a larger wavefunction overlap leading to a larger absorption coefficient.

The percentage wave function ($\psi_{(E1)}$) in the well was calculated using the equation below

$$\% \text{ wavefunction in the well} = \frac{\int_0^W \psi_{(E1)} dx}{\int_{-\infty}^{\infty} \psi_{(E1)} dx}$$

(4.1)

where W is the width of the well.

The percentage overlap of the two wave functions is calculated by taking the lower of the 2 wave functions. A and B in Figure 4.12 are the points where the wavefunction with the lowest magnitude changes over. The wavefunction with the lowest magnitude was divided by the integration of the other wave function. For example in Figure 4.12 between 0 and point A the lowest magnitude wavefunction is E1, which is divided by the HH1 wavefunctions between the points. Whereas, between points A and B HH1 is the lowest wavefunction so it is divided by the integrated E1 wavefunction.

$$\text{Wavefunction overlap} = \frac{\int_0^A \psi_{(E1)}(x) dx}{\int_0^A \psi_{(HH1)}(x) dx} + \frac{\int_B^A \psi_{(HH1)}(x) dx}{\int_B^A \psi_{(E1)}(x) dx} + \frac{\int_L^B \psi_{(E1)}(x) dx}{\int_L^B \psi_{(HH1)}(x) dx} \quad (4.2)$$

where L is the length of the superlattice period. For ease of calculation only the lowest energy electron level and highest energy heavy hole level wavefunction were used, and the miniband dispersion is ignored. The calculations were calculated for $k=0$ in the k plane, not across all positions in the k plane. Calculating the overlap for all positions across the k plane would be more accurate. These approximations mean the wavefunction overlaps calculated below are treated as indicative of the total overlap rather than the definitive overlap.

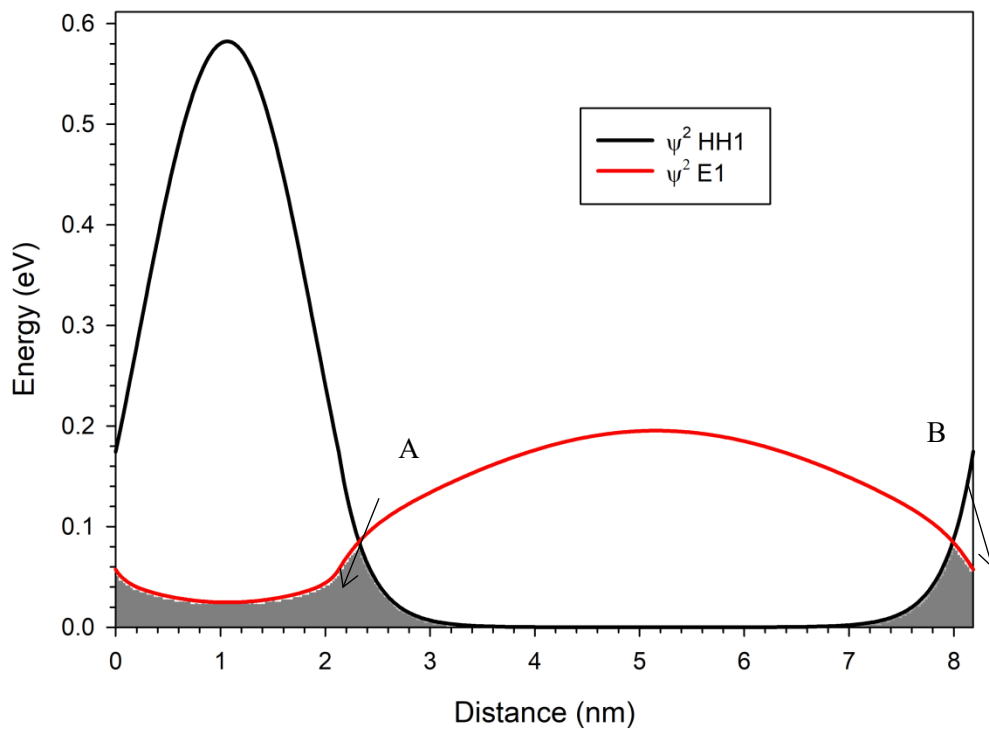


Figure 4.12: The graphical representation of the squared wavefunction overlap calculated in equation (4.2)

Table 4.1: The percentage wavefunction overlap of HH1 and E1 for superlattice structures with similar cut-off wavelengths in the MWIR, LWIR and VLWIR.

	InAs Well (ML)	GaAsSb Barrier (ML)	Cutoff wavelength (μm)	Wavefunction overlap (%)
MWIR	7	20	4.7	11.7
	9	7	5.2	16.1
LWIR	14	14	7.98	8.8
	16	10	7.68	8.3
VLWIR	18	16	14.5	7.1
	20	10	14.1	6.7

Table 4.1 shows the wavefunction overlaps for several designs with similar cutoff wavelengths. The overlaps were calculated using the method demonstrated in figure 4.12. The designs with closer to symmetrical designs have larger wave function overlaps. This is as expected as the wave function will leak into the barrier material and interact with the wave function from the neighbouring well increasing the wave function overlap.

4.4 Discussion

The weak dependence of the cutoff wavelength on the barrier (GaAsSb) thickness is consistent with those reported in [16,17] for other InAs/InAsSb superlattice T2SLs. This can be explained by the smaller effective mass of the electrons, causing E1 to change more prominently with the quantum well width. To provide a qualitative explanation, the energy level (E_n where n is the number of the energy level) in a quantum well with infinite barrier potential is given by

$$E_n = \left(\frac{\hbar^2 n^2}{2m^* L^2} \right) \quad (4.3)$$

where m^* is the effective mass of the electron in InAs, L is the width of the quantum well and \hbar is reduced Planck's constant. On the other hand if m^* is large, as it is for the holes in GaAsSb, the effect of L will be weaker.

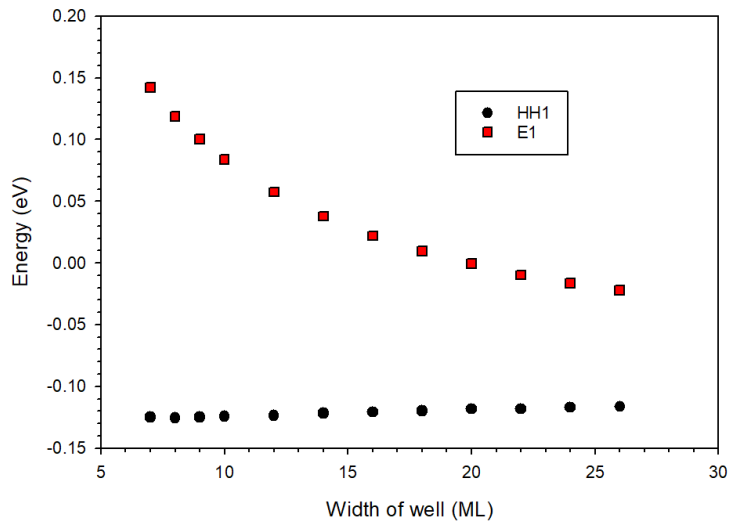


Figure 4.13: The change in the energy of HH1 and E1 of a InAs/ GaAsSb superlattice at 77 K, with a barrier width set at 7 ML and a changing width of well from 7 ML to 26ML to demonstrate the effect of equation(4.3).

The simulated results demonstrated that multiple designs can produce the same cutoff wavelength. It is noted that symmetrical designs produce higher absorption coefficients. Recall, in Figure 4.11 the symmetrical design (16 ML InAs/17 ML GaAsSb) shows a higher wavefunction overlap than an asymmetrical design (22 ML InAs/7 ML GaAsSb). Besides the absorption coefficient consideration, it is worth considering the role of the InAs layer thickness when designing the lattice matched InAs/GaAsSb T2SL. Some of the reported influence of InAs includes:

- 1) Results by R. Taalat [18] suggest InAs rich structures would be preferable for InAs/GaSb superlattice. When compared to different superlattice designs with λ_c of 5 μm , the InAs rich structure (7 ML InAs/ 4 ML GaSb) has a dark current density $2 \times 10^{-7} \text{ Acm}^{-2}$ at -0.8 V whereas a symmetrical period (10 ML InAs/ 10 ML GaSb) had a dark current density of $4 \times 10^{-6} \text{ Acm}^{-2}$ at -0.8 V.
- 2) InAs has a background doping of N-type and GaSb has P-type due to defects [19,20]. GaSb structures with native Ga vacancies causes a high p-type background doping in superlattices containing GaSb [21,22,23]. The thickness of InAs can be used to control the effective background doping of the T2SL [24].
- 3) Simulations suggest that the VLWIR can be achieved, using a thick InAs layer. For example the 20 ML InAs/ 12 ML GaAsSb has a cutoff wavelength of 15 μm . Therefore, to achieve a very broadband absorption design a thick InAs layer can be adopted.

4.5 Conclusions

In summary, 8-band $k \cdot p$ theory was used to calculate the effective bandgap of InAs/GaAsSb type-II superlattice structures. The models in nextnano+ was validated and confirmed to be capable of reproducing experimentally reported bandgaps and absorption coefficients. Thick absorption regions are needed for high performance detectors as the absorption coefficient is lower in InAs/GaAsSb, relative to those in strained InAs/GaSb superlattice lattice matched materials. However, the main expected advantage for InAs/GaAs_{0.09}Sb_{0.91} based superlattice structures is strain free layers so that thick absorption regions can be grown with reduced defects. Effective bandgap simulations indicate that the InAs/GaAsSb superlattices are more dependent on the thickness of the InAs than on the thickness of the GaAsSb superlattice layers. The simulations also suggest LWIR is possible with structures with InAs wells >12 ML and VLWIR is possible with InAs wells >16 ML, provided that the GaAsSb barriers are > 12 ML. Absorption coefficient simulations indicate that symmetrical (similar thicknesses of InAs well and GaAsSb barrier) superlattices will have higher absorption coefficients than asymmetrical structures with similar bandgaps.

The LWIR results show that for designs with cutoff wavelengths of 10 μm , a more symmetrical period design (for example 16 ML InAs/10 ML GaAsSb) yields a higher absorption coefficient, 177.94 cm^{-1} . When compared to the asymmetrical design 20 ML InAs /7 ML GaAsSb which has an absorption coefficient of 31.57 cm^{-1} . The LWIR absorption coefficient at 10 μm results also suggests designs with a 13 μm cutoff wavelength, a close to symmetrical period design (17 ML InAs /16 ML GaAsSb) yields a 170.2 cm^{-1} higher absorption coefficient than 26 ML InAs /7 ML GaAsSb, 200.4 to 30.2 cm^{-1} . Further simulations suggest this higher absorption is due to higher wavefunction overlap.

References

¹ W. Fangfang, Z. Yi, and H. Li, "High performance InAs/GaAsSb superlattice long wavelength infrared photo-detectors grown on InAs substrates," *Semicond. Sci. Technol*, vol. 32, p. 055011, 2017.

² S. M. Bedair, T. P. Humphreys, N. A. El-Masry, Y. Lo, N. Hamaguchi, C. D. Lamp, *et al.*, "Defect reduction in GaAs grown by molecular beam epitaxy using different superlattice structures," *Appl. Phys. Lett.*, vol. 49, pp. 942-944, 1986.

³ X. Zhicheng, C. Jianxin, W. Fangfang, Z. Yi, and H. Li, "High performance InAs/GaAsSb superlattice long wavelength infrared photo-detectors grown on InAs substrates," *Semicond. Sci. Technol*, , vol. 32, p. 055011, 2017.

⁴ S. Adachi, "Optical dispersion relations for GaP, GaAs, GaSb, InP, InAs, InSb, Al_xGa_{1-x}As, and In_{1-x}Ga_xAs_YP_{1-Y}" *J Appl Phys*, vol 66, pp. 6030, 1989.

-
- ⁵ F. Wang, J. Chen, Z. Xu, Y. Zhou, and L. He, "Performance comparison between the InAs-based and GaSb-based type-II superlattice photodiodes for long wavelength infrared detection," *Opt Express*, vol. 25, pp. 1629-1635, 2017/02/06 2017.
- ⁶ J. Wu, Z. Xu, J. Chen, and L. He, "Temperature-dependent photoluminescence of the InAs-based and GaSb-based type-II superlattices," *Infrared Phys Technol*, vol. 92, pp. 18-23, 2018/08/01/ 2018.
- ⁷ D. Jiang, W. Xiang, F. Guo, H. Hao, X. Han, X. Li, *et al.*, "Very high quantum efficiency in InAs/GaSb superlattice for very long wavelength detection with cutoff of 21 μm ," *Appl. Phys. Lett*, s, vol. 108, p. 121110, 2016.
- ⁸ C. H. Grein, W. H. Lau, T. L. Harbert, and M. E. Flatte, "Modeling of very long infrared wavelength InAs/GaInSb strained layer superlattice detectors" vol. 4795: *SPIE*, 2002.
- ⁹ S. Birner, T. Zibold, *et al.* "nextnano: General Purpose 3-D Simulations," *IEEE Trans. Electron Dev.* 54, 2137 (2007)
- ¹⁰ D. Lackner, M. Steger, M. L. W. Thewalt, O. J. Pitts, Y. T. Cherng, S. P. Watkins, *et al.*, "InAs/InAsSb strain balanced superlattices for optical detectors: Material properties and energy band simulations," *J Appl Phys*, vol. 111, p. 034507, 2012.
- ¹¹ F. Wang, J. Chen, Z. Xu, Y. Zhou, and L. He, "InAs-based InAs/GaAsSb type-II superlattices: Growth and characterization," *J. Cryst. Growth*, vol. 416, pp. 130-133, 2015/04/15/ 2015.
- ¹² D. L. Smith, and C. Mailhiot, "Proposal for strained type II superlattice infrared detectors" *J Appl Phys*, 62, pp. 2545-2548, 1987,
- ¹³ C. Mailhiot, and D. L. Smith, "Long-wavelength infrared detectors based on strained InAs-Ga_{1-x}In_xSb type-II superlattices" *J. Vac. Sci. Technol. A*, 7, pp. 445-449, 1989
- ¹⁴ J. Easley, C. R. Martin, M. H. Ettenberg, and J. Phillips, "InGaAs/GaAsSb Type-II Superlattices for Short-Wavelength Infrared Detection," *J Electron Mater*, vol. 48, pp. 6025-6029, October 01 2019.
- ¹⁵ G. Ariyawansa, M. Grupen, J. M. Duran, J. E. Scheihing, T. R. Nelson, and M. T. Eismann, "Design and modeling of InAs/GaSb type II superlattice based dual-band infrared detectors," *J Appl Phys*, vol. 111, p. 073107, 2012.
- ¹⁶ A. M. Hoang, G. Chen, A. Haddadi, S. A. Pour, and M. Razeghi, "Demonstration of shortwavelength infrared photodiodes based on type-II InAs/GaSb/AlSb superlattices," *Appl. Phys. Lett.*, vol. 100, p. 211101, 2012
- ¹⁷ H. J. Haugan, F. Szmulowicz, G. J. Brown, and K. Mahalingam, "Band gap tuning of InAs/GaSb type-II superlattices for mid-infrared detection," *J Appl Phys*, vol. 96, pp. 2580-2585, 2004.
- ¹⁸ R. Taalat, J.-B. Rodriguez, M. Delmas, and P. Christol, "Influence of the period thickness and composition on the electro-optical properties of type-II InAs/GaSb midwave infrared superlattice photodetectors," *J Phys D Appl Phys*, vol. 47, p. 015101, 2013/12/03 2013.
- ¹⁹ M. Gorni, A. Parisini, E. Gombia, M. Baldini, S. Vantaggio and C. Ghezzi, "Electrical characterization of a buried GaSb p-n junction controlled by native defects," *Cryst. Res. Technol*, vol, 49, pp. 628-633, 2014.
- ²⁰ D. Shaw, "Native defects and self-diffusion in GaSb," *Semicond. Sci. Technol.*, IOP Publishing, Vol 18, pp. 627-632, 2003.
- ²¹ M. Hakala, M. J. Puska, and R. M. Nieminen, "Native defects and self-diffusion in GaSb," *J Appl Phys*, vol. 91, pp. 4988-4994, 2002.
- ²² H. Bracht, S. P. Nicols, E. E. Haller, J. P. Silveira, and F. Briones. "Self-diffusion in ⁶⁹Ga/¹²¹Sb/⁷¹Ga/¹²³Sb isotope heterostructures." *J Appl Phys*, vol.89 (10), pp. 5393-5399, 2001.
- ²³ S.P. Svensson, D. Donetsky, D. Wang, H. Hier, F.J. Crowne, G. Belenky, "Growth of type II strained layer superlattice, bulk InAs and GaSb materials for minority lifetime characterization," *J. Cryst. Growth*, vol. 334 (1), pp. 103-107, 2011
- ²⁴ M Delmas, D C M Kwan, M C Debnath, B L Liang and D L Huffaker. "Flexibility of G containing Type-II superlattice for long-wavelength infrared detection" *J Phys D Appl Phys*, Vol.52 (47) pp. 5102, 2019

5. Temperature dependence of InAs/GaAs_{0.09}Sb_{0.91} superlattice cutoff wavelength and absorption coefficient simulations

5.1. Introduction

The previous chapter explored the effect of different periods of the superlattice on cutoff wavelength and absorption coefficient. In this chapter a more detailed study of the temperature dependence of these parameters are carried out. Since T2SL IR photodetectors are normally operated at low temperatures to minimise dark currents, it is important to investigate how absorption coefficients change with temperature. This is particularly important if the operating wavelength is close to the cutoff wavelength of the photodetector.

The key observations in this chapter are:

- Nextnano++ simulations of the temperature dependence of cutoff wavelength are in good agreement with literature values in Figure 5.1 and Figure 5.2 [1].
- Stronger temperature dependence of cutoff wavelength and absorption coefficients was seen in superlattice structures with longer smaller bandgaps. This is most pronounced when the InAs Well thickness is changed.
- Changing the GaAsSb barrier was found to have relatively weak influence over the cutoff wavelength and its temperature dependence behaviour, if the cutoff wavelength is in the MWIR.
- InAs/GaAsSb superlattice designs with similar cutoff wavelengths and different periods were simulated. The simulations showed structures with similar cutoff wavelengths exhibit similar temperature dependence of cutoff wavelength.
- Comparisons of the optical absorption coefficients of the structures with similar cutoff wavelengths showed higher absorption coefficients are obtained if the thicknesses of InAs and GaAsSb are more similar. This was observed in structures having cutoff wavelengths in the LWIR and VLWIR wavelengths.

5.2. Model validation

The nextnano++ band structure simulations have been validated at 77 K and 300 K in the previous chapter. To validate them at other temperatures, more simulations were done. In the nextnano++ program the valence band position is fixed, the bandgap is temperature dependent the conduction band energies do change with temperature. The change in conduction band energies and the bandgap depend on the Varshni equation (equation 2.29).

This is important as InAs and GaAsSb have different dependencies on temperature. The theoretical E_g of bulk InAs changes with temperature by 0.1 eV from 0 K to 300 K [2], whereas the E_g of GaAs_{0.33}Sb_{0.67} changes by 0.07 eV over 300 K [3]. [3] also shows that temperature dependence of E_g does not significantly change with the percentage of Sb in the GaAsSb alloy. The strained InAs/GaSb T2SL is commonly used for the LWIR and several temperature dependence of cutoff wavelength studies have been conducted. However, there is no extensive study of cutoff wavelength for different superlattice periods on the lattice matched InAs/GaAs_{0.09}Sb_{0.91} superlattice system. To validate the model's accuracy, the cutoff wavelengths of InAs/GaSb T2SLs were simulated at multiple temperatures for two different superlattice periods shown in Figure 5.1.

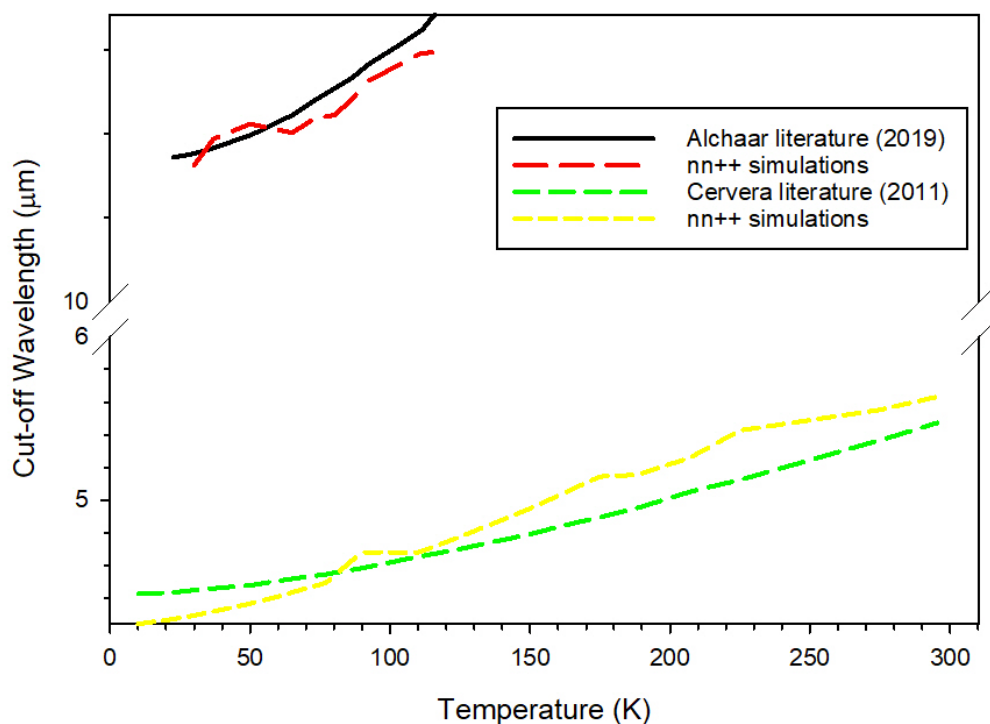


Figure 5.1 Nextnano++ (nn++) cutoff wavelength simulations for two strained InAs/GaSb superlattice structures at various temperatures compared to experimental results. The red and black structures 15 ML InAs/7 ML GaSb [4], the Yellow and Green structures are 8 ML InAs/8 ML GaSb. [5]

Both [5] and [4] in Figure 5.1 are experimental, not simulation results. The simulation results show qualitative agreement to the experimental results. The small deviation could be due to the simulation superlattices being “perfect” structures with no defects and every period being exactly the same thickness, whereas the experimental results may have imperfections.

To further test the model, another lattice matched In_{0.53}Ga_{0.47}As/ GaAs_{0.51}Sb_{0.49} SWIR superlattice structure was simulated in Figure 5.2. The SWIR experimental results from [6] are very close with the simulation using the nextnano default database especially at the higher temperatures. The

simulation agreement was improved by reducing the nn^{++} valence band offset of the barrier material by 0.16 eV.

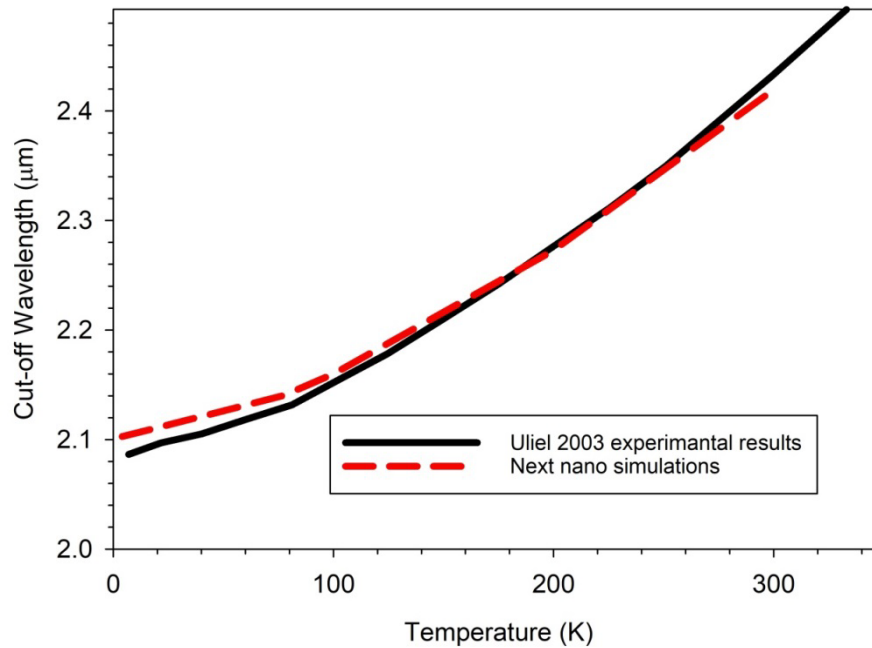


Figure 5.2: Nextnano simulations for 5 nm InGaAs/5 nm GaAsSb lattice matched superlattice cutoff wavelength at various temperatures compared to experimental literature results. [6]

5.3. Temperature dependence of cutoff wavelength simulation

Simulations to investigate how the cutoff wavelength of the superlattice varies with temperature were performed. In the nextnano++ program the valence band position is fixed, the bandgap is temperature dependent the conduction band energies do change with temperature. The change in conduction band energies and the bandgap depend on the Varshni equation (equation 2.29). The results for symmetric superlattices are shown in Figure 5.3. The results in Figure 5.3 (A) show a very small change in cutoff wavelength for the MWIR superlattice structures as seen by the black line. The increase in cutoff wavelength at higher temperatures increased was greater in larger superlattice structures, which have cutoff wavelengths in the LWIR and the VLWIR (the blue, pink and aqua lines in Figure 5.3). This trend is further demonstrated in Table 5.1 where the MWIR structure (7 ML/7 ML) cutoff wavelength increases from 4.5 μm to 5.7 μm , when the temperature is increased by from 40 to 300 K. The difference in the wavelength shown in Table 5.1 for the 7 ML/7 ML was 1.2 μm , a total percentage change of 23.5 %. The change in the cutoff wavelength is more pronounced at longer wavelengths. The cutoff wavelength of the VLWIR structure, 20 ML/20 ML, changes by significantly more, from 17.2 μm to 35 μm a change of 17.8 μm over the same temperature range; this is a much larger percentage change of 68.2 %. This

is also illustrated by the highest value of $d\lambda_c/dT$ starting at $0.03 \mu\text{m}/\text{K}$ and increasing to $0.27 \mu\text{m}/\text{K}$ at temperatures of 295 K as shown in Figure 5.3 (B).

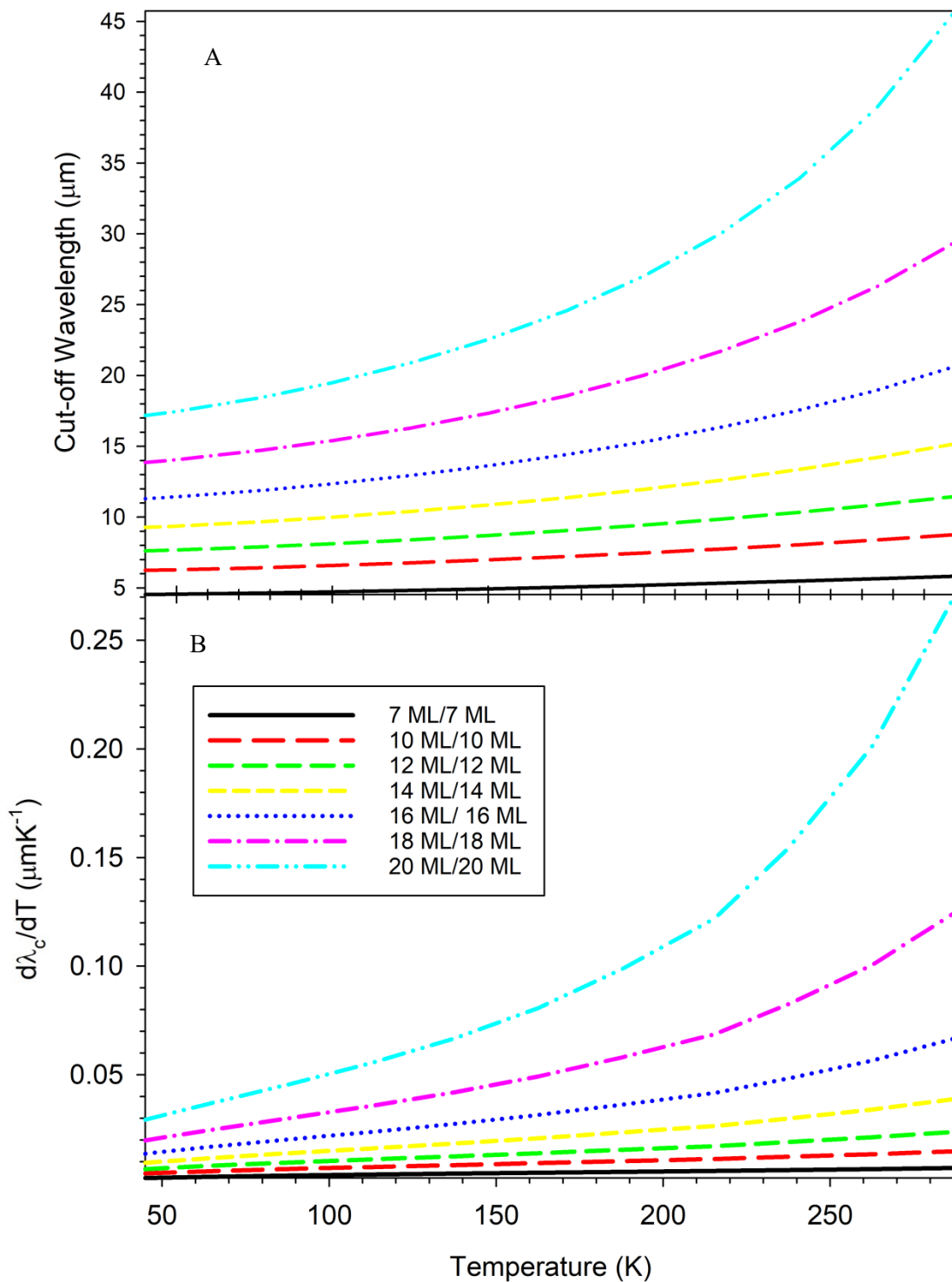


Figure 5.3(A) The cutoff wavelength of lattice matched symmetrical InAs/GaAsSb superlattices at temperatures varying from 40 K to 300 K. (B) the change in the cutoff wavelength over the change in temperature for the same structures

Table 5.1: The difference in cutoff wavelength of lattice matched symmetrical InAs/ GaAsSb superlattices at the temperatures 40 K and 300 K.

	Cutoff wavelength at 40 K (μm)	Cutoff wavelength at 300 K (μm)	Difference in cutoff wavelength (μm)	Percentage difference in cutoff wavelength (%)
7 ML/ 7 ML	4.5	5.7	1.2	23.5
12 ML/ 12 ML	7.6	11.5	3.9	40.8
16 ML/ 16 ML	11.3	20.6	9.3	58.3
20ML/ 20 ML	17.2	35.0	17.8	68.2

The larger change in the cutoff wavelength for the LWIR and VLWIR structures can be explained by the relationship between E_g and the cutoff wavelength (λ_c) described below and the Varshni equation (2.29 repeated)

$$\lambda_c = \frac{hc}{E_g} . \quad (1.2 \text{ repeated})$$

The Varshni equation describes the E_g dependence on temperature,

$$E_g(T) = E_g(0) - \frac{\alpha_g T^2}{\beta_g + T} . \quad (2.29 \text{ repeated})$$

These equations partly explain the significantly larger $d\lambda_c/dT$ value for the 20 ML InAs/20 ML GaAsSb structure compared to the structure with a smaller period of 7 ML InAs/7 ML GaAsSb. Equation 1.2 clearly shows that a small change in E_g leads to a large change in the cutoff wavelength at VLWIR wavelengths.

To investigate whether the barrier or well dimension has a larger effect on the temperature dependence of the cutoff wavelength, the dependence of the barrier thickness on the cutoff wavelength with temperature was simulated. Structures with an InAs well thickness of 7 ML and a GaAsSb barrier thickness varying from 7 ML to 20 ML, shown in Figure 5.4.

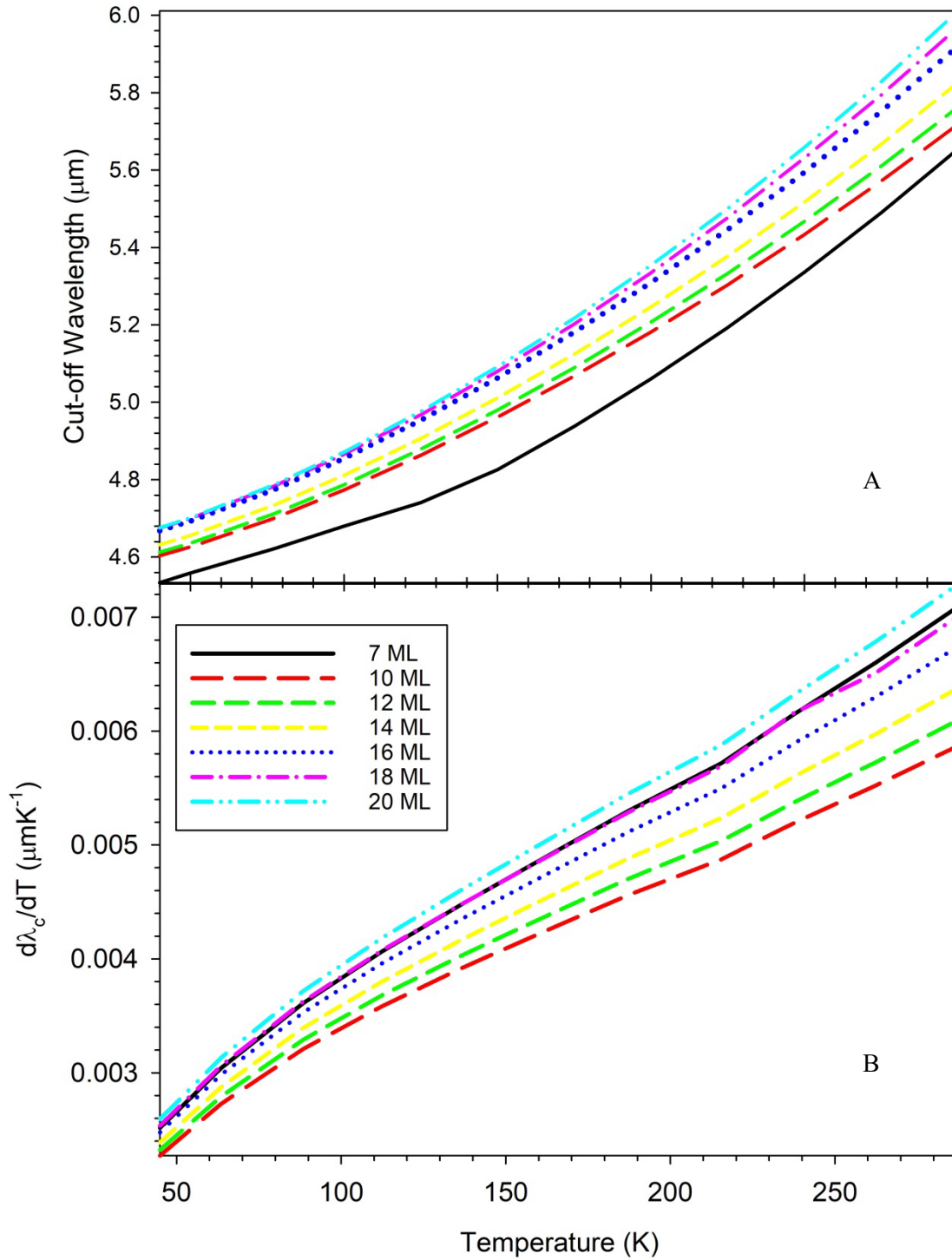


Figure 5.4: (A) The cutoff wavelengths of superlattice with periods varying from 7 ML InAs/7 ML GaAsSb to 7 ML InAs/20 ML GaAsSb with increasing temperature. (B) the change in the cutoff wavelength over the change in temperature for the same structures

The cutoff wavelengths of the structures varies from 4.5 μm to 4.7 μm for the 7 ML InAs/7 ML GaAsSb and 7 ML InAs/20 ML GaAsSb respectively at 40 K. Most of the structures have a cutoff wavelength increase of 1.2 μm across the temperatures. The effect of increasing barrier size has little influence over $d\lambda_c/dT$ compared to those for symmetrical periods in Figure 5.3. This may be

due to the relatively large bandgaps of all the structures as the cutoff wavelengths are in the MWIR at 40 K. Figure 5.4 (B) shows that the change in $d\lambda/dT$ increases marginally with the size of the GaAsSb layer. The largest change of $d\lambda/dT$ is $0.007\mu\text{m}/\text{K}$ and the smallest is $0.0052\mu\text{m}/\text{K}$, indicating the changes are minimal. The change in cutoff wavelength values is further illustrated in Table 5.2. The percentage change in the cutoff wavelength for these structures is around 23 %; this is understandable as the cutoff wavelengths of the structures at 40 K are between 4.5 and $4.7\mu\text{m}$ across the whole barrier size range. The increasing barrier size raises the first heavy hole band towards the top of the valence band, reducing the overall bandgap of the structure and hence increasing the cutoff wavelength. The results in this section confirm that as the T2SL bandgap, and its temperature dependence are weakly dependent on the thickness of the GaAsSb barrier.

Table 5.2: The cutoff wavelength change of InAs/GaAsSb superlattice structures with well thickness of 7 ML and changing barrier thickness

InAs/GaAsSb	Cutoff wavelength at 40 K (μm)	Cutoff wavelength at 300 K (μm)	Difference in cutoff wavelength (μm)	Percentage difference in cutoff wavelength (%)
7 ML/ 7 ML	4.5	5.7	1.2	23.5
7 ML/ 12 ML	4.6	5.8	1.2	23.1
7 ML/ 16 ML	4.7	5.9	1.2	22.6
7 ML/ 20 ML	4.7	6.0	1.3	24.3

Next, the influence of InAs well thickness as investigated. Simulations were carried out with InAs thickness ranging from 7 ML to 20 ML and a fixed GaAsSb barrier of 7 ML thick. Figure 5.5 shows that as the InAs layer thickness increases, the change in cutoff wavelength is more pronounced with increasing temperature. The change in the $d\lambda/dT$ for the 7 ML InAs/7 ML GaAsSb is much smaller than the change $d\lambda/dT$ for the 20 ML InAs/7 ML GaAsSb.

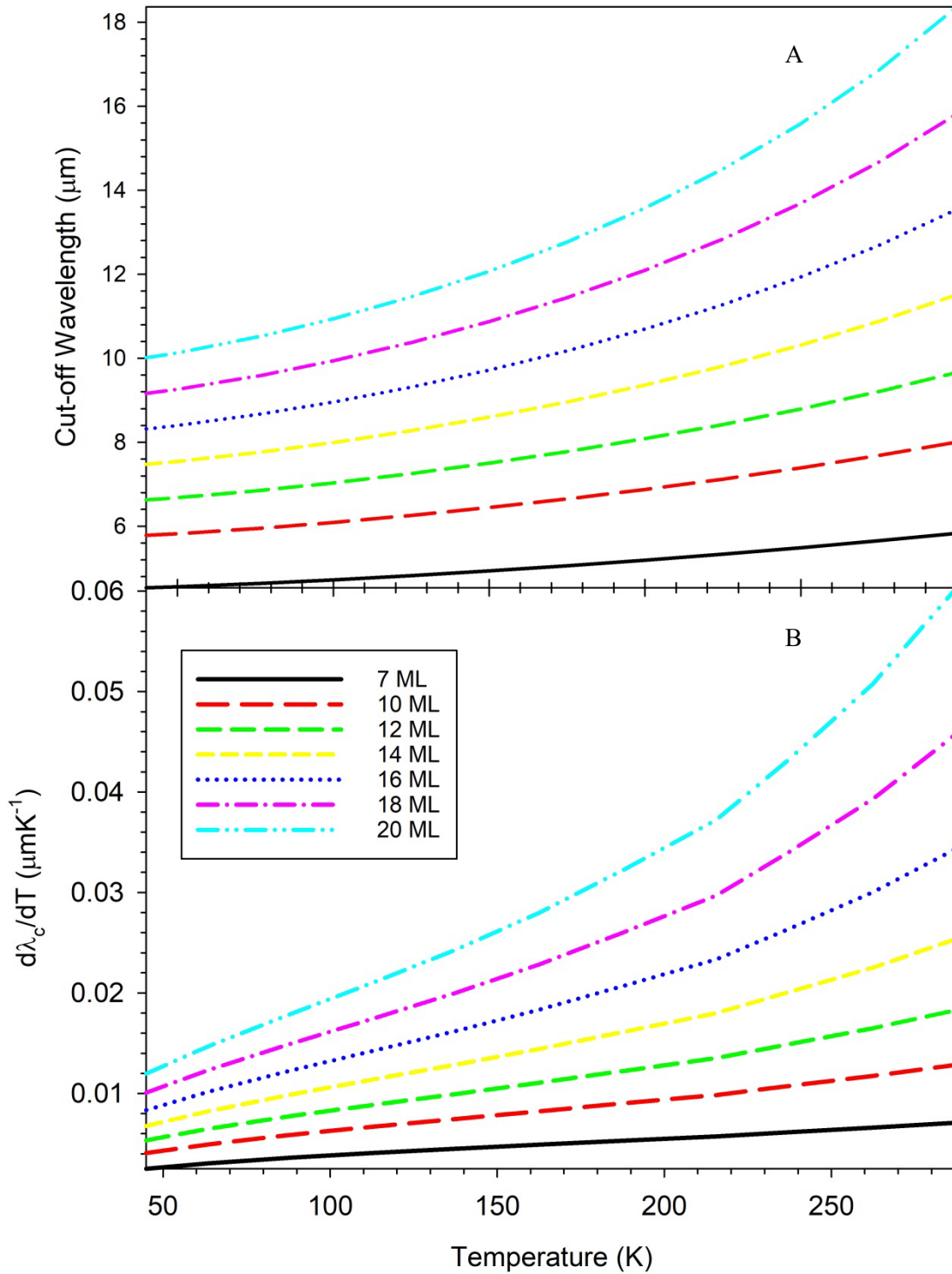


Figure 5.5: (A) the cutoff wavelength of InAs/GaAsSb superlattices with a 7 ML GaAsSb barrier and changing InAs well widths from 7 ML to 20 ML at temperature ranging from 40 K to 300 K. (B) The change in the cutoff wavelength over the change in temperature for the same structures

The results in Figure 5.5 (A) shows that the 7 ML InAs/20 ML GaAsSb structure changes from a cutoff wavelength of 10.0 μm at 40 K, lengthening to a VLWIR structure with a cutoff wavelength of 18.4 μm at 300 K. Compared to the 7 ML InAs/7 ML GaAsSb structure which stays within the MWIR wavelengths. As seen in Figure 5.5 (B) the change in $d\lambda_c/dT$ is one order

of magnitude larger than the results in Figure 5.4 (B). The largest change in cutoff wavelength is 8.4 μm , as seen in Figure 5.5 is for a VLWIR structure with 20 ML of InAs wells. The percentage change in cutoff wavelength from Figure 5.5 is presented in Table 5.3. The percentage change for the LWIR structure 20 ML InAs/7 ML GaAsSb is 59.2 %, more than double the percentage change for the MWIR structure 7 ML InAs/7 ML GaAsSb. This is not a surprise due to the smaller value of E_g in the LWIR structure.

Table 5.3: The cutoff wavelength change of InAs/GaAsSb superlattice structures with well thickness of 7 ML and changing barrier thickness

InAs/GaAsSb	Cutoff wavelength at 40 K (μm)	Cutoff wavelength at 300 K (μm)	Difference in cutoff wavelength (μm)	Percentage difference in cutoff wavelength (%)
7 ML/ 7 ML	4.5	5.7	1.2	23.5
12 ML/ 7 ML	6.6	9.7	3.1	38.0
16 ML/ 7 ML	8.3	13.5	5.2	47.7
20ML/ 7 ML	10.0	18.4	8.4	59.2

To assess the accuracy of the simulated temperature dependence of T2SL bandgaps, the published results in the literature are compared. In the MWIR superlattice [5] in Figure 5.1, the InAs/GaSb superlattice cutoff wavelength varies by 20.4 % compared to the 23 % in the 7 ML InAs/7ML GaAsSb MWIR structure in Table 5.3. In the LWIR InAs/GaSb photodiodes from [4] they reported a change of 2.7 % in the cutoff wavelength from 40 K to 115 K. This is a change of 0.02 μm per degree compared to the 0.032 μm per degree for the LWIR 20 ML InAs/7 ML GaAsSb structure in Table 5.3. This suggests the InAs/GaAsSb superlattices in the LWIR are more sensitive to temperature change than InAs/GaSb superlattices.

Figure 5.5 shows for structures with the same barrier size and a well size varying from 7 ML to 20 ML. As temperature increases the cutoff wavelength of the superlattice increases, as does the change in cutoff wavelength. The difference between the cutoff wavelength of 7 ML InAs/7 ML GaAsSb and the 20 ML InAs/7 ML GaAsSb at 77 K is 5.9 μm which increases to a difference of 12.7 μm at 300 K. This can be explained by longer wavelength structures being more dependent on temperature. The MWIR superlattice results have a similar percentage cutoff wavelength change to the results from in Figure 5.2 where the InAs/GaSb superlattice varies by 20.4 % compared to the 23 % of the nextnano simulations. LWIR InAs/GaSb photodiodes from have percentage change of 2.7 % in the cutoff wavelength from 40 K to 115 K this is a change of 0.2 μm per degree compared to the 1.45 μm over same temperature range for the LWIR

20ML InAs/7 ML GaAsSb structure. This suggests the InAs/GaAsSb superlattices in the LWIR are more sensitive to temperature change than InAs/GaSb superlattices.

Results in this section show that the cutoff wavelengths of LWIR and VLWIR structures have a larger dependence on temperature. This temperature dependence could be a disadvantage for a superlattice design as any temperature fluctuations could drastically change the E_g of the structure. This would be a considerable disadvantage when the wavelengths of interest are close to the structure's cutoff wavelength, as any change in the E_g of the structure can significantly change the absorption coefficient. For example a structure with a 10.3 μm cutoff wavelength at 77 K the absorption coefficient at 9 μm changes from 12 to 35 cm^{-1} at 100 K. To verify whether symmetrical or non-symmetrical structures have stronger temperature dependence, simulations for structures with cutoff wavelength close to 10 μm at 77 K were simulated.

5.3.1. Comparison of structures with the same cutoff wavelength at 77 K

The temperature dependant cutoff wavelength simulations were extended to include eight structures with cutoff wavelengths close to 10 μm at 77 K. The results in Figure 5.6 show that structures with the similar cutoff wavelengths will exhibit similar temperature dependence.

In Figure 5.6(A) two superlattice structures 16 ML InAs/10 ML GaAsSb and 20 ML InAs/7 ML GaAsSb show very similar cutoff wavelengths across all temperatures. Figure 5.6 (B) clearly shows how the $d\lambda_c/dT$ is not strongly dependent on the design. $d\lambda_c/dT$ is marginally reduced when the thickness of GaAsSb is increased from 12 ML to 20 ML, for a fixed 14 ML InAs.

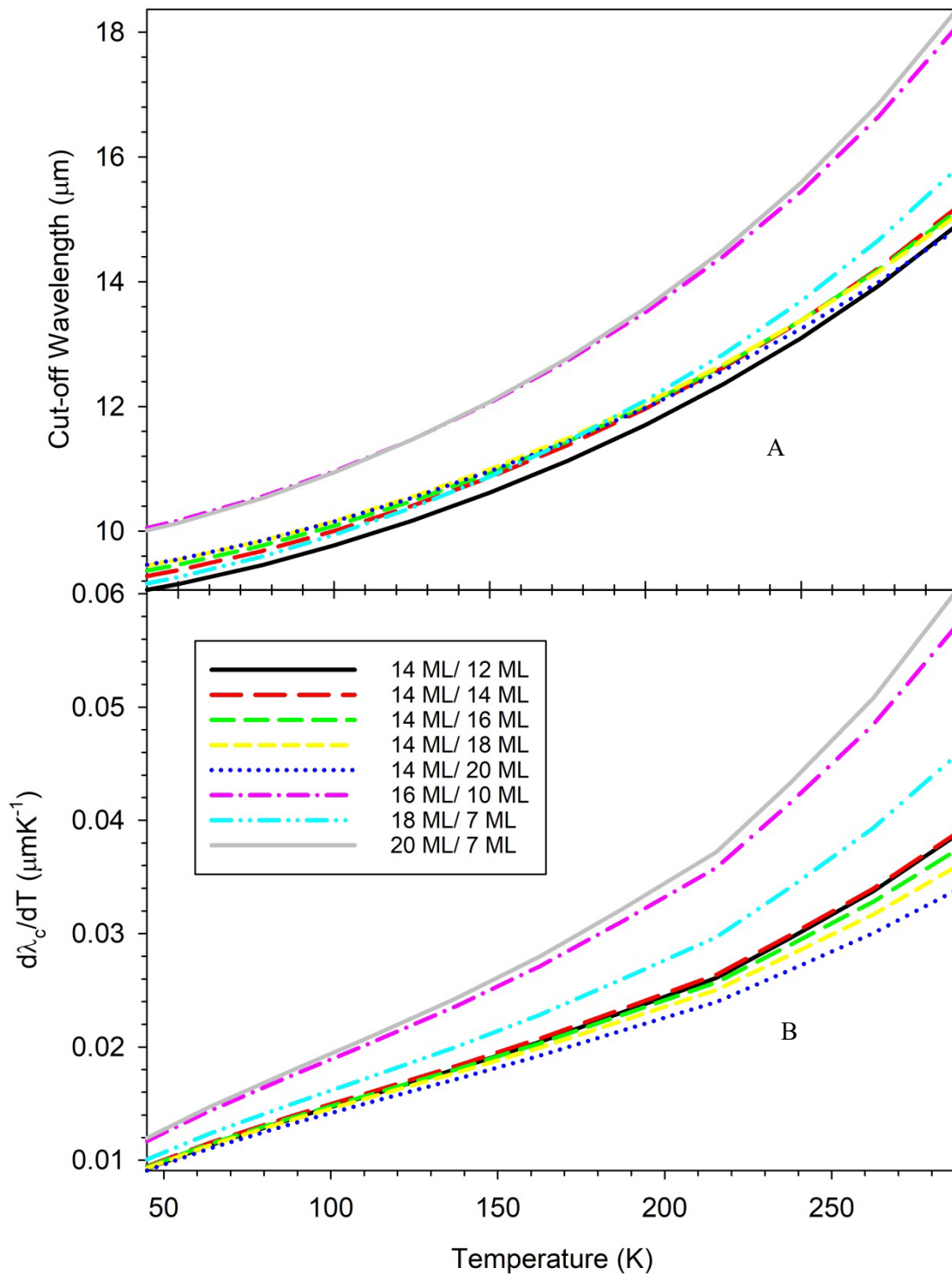


Figure 5.6: (A) InAs/GaAsSb superlattice periods with a cutoff wavelength close to 10 μm at 77 K (B) the change in the cutoff wavelength over the change in temperature for the structures in A

In addition to cutoff wavelength, the temperature dependence of the absorption coefficient is investigated. Two of these structures, 16ML InAs/10 ML GaAsSb and 20ML InAs/7 ML GaAsSb, were simulated.

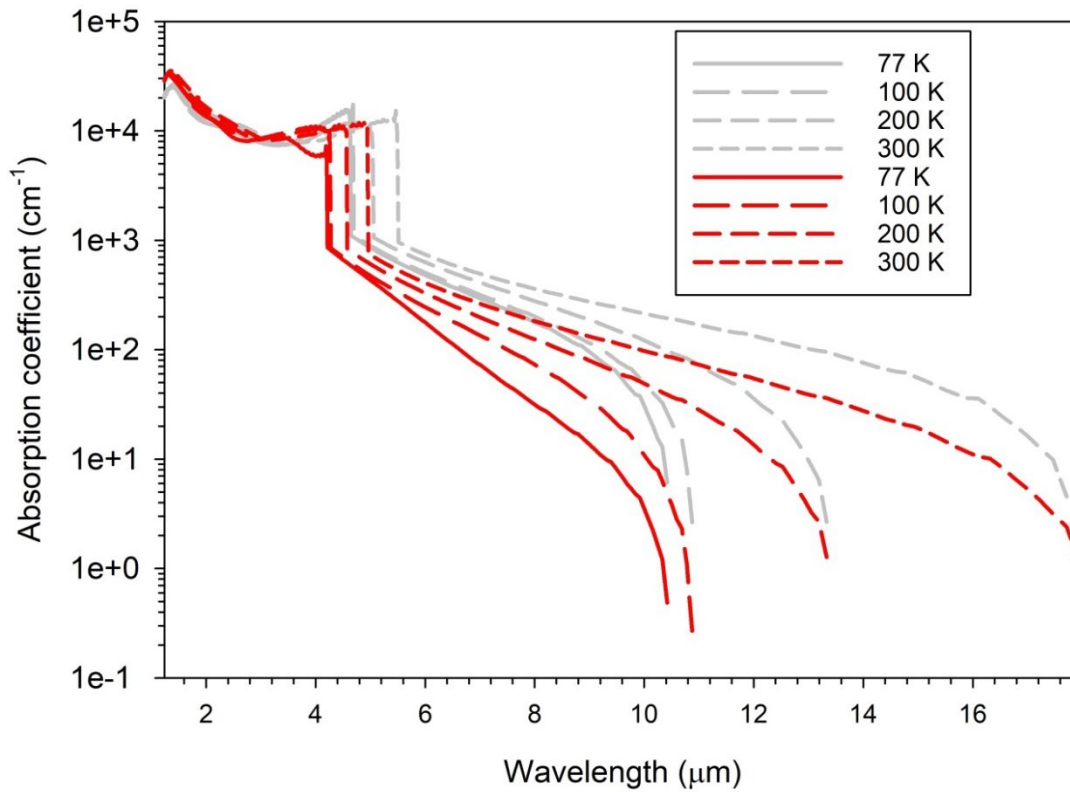


Figure 5.7 Absorption coefficient at different wavelengths for various temperatures, 77 K, 100 K, 200 K, and 300 K, for the superlattices 16 ML InAs/10 ML GaAsSb (grey) and 20 ML InAs/7 ML GaAsSb (red).

The results in Figure 5.7 consistently show that for the two structures, the more symmetrical 16 ML InAs/10 ML GaAsSb structure has a larger absorption coefficient at all the simulated temperatures. The cutoff wavelength of the two structures stayed comparable as the temperature increased. The difference in absorption coefficient is especially noticeable in the wavelengths closer to the structures cutoff wavelength; the absorption is in the same order of magnitude in the MWIR (below 4 μm). Figure 5.7 extends the conclusion drawn in the previous chapter suggesting that close to symmetrical structures are preferable, as they have higher absorption coefficients at all temperatures.

The comparison of the absorption coefficients at 8 μm is shown in Table 5.4. The absorption steadily increases as the cutoff wavelength of the structure increases. The largest difference in absorption coefficient is for 300 K with a value of 176 cm^{-1} .

Table 5.4: Comparison of the absorption coefficient for 16 ML InAs/ 10 ML GaAsSb and 20 ML InAs/ 7 ML GaAsSb at 8 μm and at multiple temperatures

Temperature (K)	16 ML InAs/10 ML GaAsSb (cm^{-1})	20 ML InAs/7 ML GaAsSb (cm^{-1})	Difference in absorption coefficient (cm^{-1})
77	178	32	143
100	201	73	128
200	277	124	153
300	359	182	177

Another pair of structures with a cutoff wavelength close to VLWIR at 77 K was compared in Figure 5.8. The results in Figure 5.8 show similar trends, the structures have similar cutoff wavelengths at all temperatures and the more symmetrical structure have a consistently higher absorption coefficient.

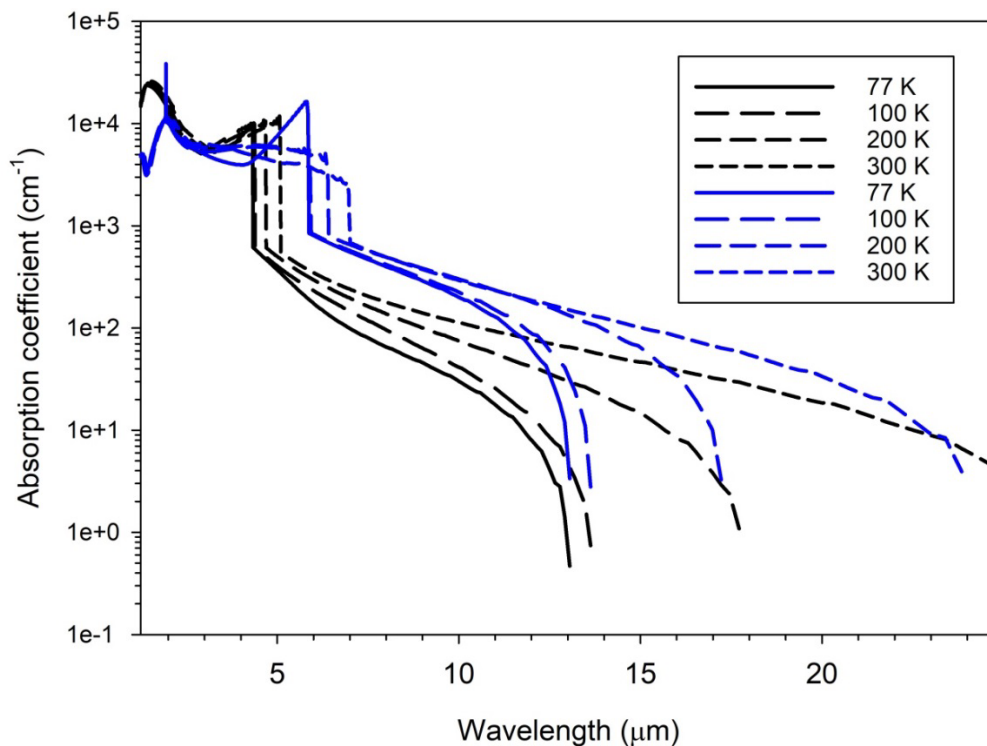


Figure 5.8: Absorption coefficient at different wavelengths for various temperatures, 77 K, 100 K, 200 K, and 300 K, for the superlattices 17 ML InAs/16 ML GaAsSb (blue) and 26 ML InAs/7 ML GaAsSb (black) which both have cutoff wavelengths of 13.1 μm .

The differences in absorption coefficients of the two structures at 10 μm are in Table 5.5. The absorption at 10 μm of 26 ML InAs/7 ML GaAsSb is weak and only goes above 100 cm^{-1} at 300 K. The difference in absorption coefficient between the two structures is around 175 cm^{-1} , except for 200 K due to the high absorption coefficient of 17 ML InAs/16 ML GaAsSb at this

temperature. This higher absorption coefficient at 200 K is due to the structure having a very sudden absorption end instead of tailing off more gradually, like the 26 ML InAs/7 ML GaAsSb structure. The difference in absorption coefficient is also higher than the shorter wavelength structures at the same temperature. This suggests that choosing a more symmetrical structure has a bigger impact on the absorption coefficient for longer wavelength detecting structures.

Table 5.5: Comparison of the absorption coefficient for 17 ML InAs/16 ML GaAsSb and 26 ML InAs/7 ML GaAsSb at 10 μm and at multiple temperatures.

Temperature (K)	17 ML InAs/16 ML GaAsSb (cm^{-1})	26 ML InAs/7 ML GaAsSb (cm^{-1})	Difference in absorption coefficient (cm^{-1})
77	200	30	170
100	225	42	184
200	302	75	227
300	294	114	180

5.4. Conclusion

The temperature dependence of cutoff wavelengths of different InAs/GaAsSb superlattices periods was investigated. The simulations were validated against InAs/GaAsSb grown on GaSb and InGaAs/GaAsSb superlattice grown lattice matched to InP.

A range of symmetrical structures, 7ML InAs/7ML GaAsSb to 20ML InAs/20ML GaAsSb were investigated. The results show that structures with larger period superlattices, with cutoff wavelengths in the LWIR and VLWIR, have a stronger dependence on temperature. In other words the cutoff wavelength increases much more rapidly with increasing temperature as the cutoff wavelength increases.

A study on the effect of changing the thickness of GaAsSb barrier found that the cutoff wavelength is weakly dependent on the thickness of GaAsSb. This also leads to a weak temperature dependence of the cutoff wavelength in all structures studied, with a fixed 7 ML InAs and GaAsSb thickness of 7ML to 20 ML. Likewise a comparative study that fixed the thickness of GaAsSb to 7 ML but varying the InAs thickness from 7 ML to 20 ML was carried out. The results reveal that the temperature dependence of cutoff wavelength is the strongest in the structure with the thickness InAs layer of 20 ML corresponding to the longest cutoff wavelength. This larger change in cutoff wavelength is attributed to the smaller E_g , as shown in equation 1.2.

Superlattices with similar cutoff wavelengths at 77 K were also simulated. The results show that structures with similar cutoff wavelengths in LWIR and VLWIR, exhibit a similar temperature dependence trend independent of the superlattice period symmetry. However structures that have

more similar thicknesses of InAs and GaAsSb (i.e more symmetrical structures) consistently show higher absorption coefficients.

References

-
- ¹ S. Birner, T. Zibold, et al. “nextnano: General Purpose 3-D Simulations,” *IEEE Trans. Electron Dev.* 54, 2137 (2007)
 - ² S. Zollner, S. Gopalan, and M. Cardona, “The temperature dependence of the band gaps in InP, InAs, InSb, and GaSb,” *Solid State Commun.*, vol. 77, no. 7, pp. 485–488, 1991, doi: 10.1016/0038-1098(91)90725-B.
 - ³ R. Lukic-Zrnic, B. P. Gorman, R. J. Cottier, T. D. Golding, C. L. Littler, and A. G. Norman, “Temperature dependence of the band gap of GaAsSb epilayers,” *J. Appl. Phys.*, vol. 92, no. 11, pp. 6939–6941, 2002, doi: 10.1063/1.1517746.
 - ⁴ R. Alchaar, J. B. Rodriguez, L. Höglund, S. Naureen, and P. Christol, “Characterization of an InAs/GaSb type-II superlattice barrier photodetector operating in the LWIR domain,” *AIP Adv.*, vol. 9, no. 5, p. 055012, May 2019,
 - ⁵ C. Cervera *et al.*, “Temperature dependence performances of InAs/GaSb superlattice photodiode,” *Proc. Int. Conf. QSIP 2010*, vol. 54, no. 3, pp. 258–262, May 2011,
 - ⁶ . Uliel *et al.*, “InGaAs/GaAsSb Type-II superlattice based photodiodes for short wave infrared detection,” *QSIP*, vol. 84, pp. 63–71, Aug. 2017, doi: 10.1016/j.infrared.2017.02.003.

6. Temperature dependence of dark current density simulations

6.1. Introduction

This chapter investigates the temperature dependence of dark current density in InAs/GaAsSb superlattices. The previous chapter suggests that structures with near symmetrical periods are favourable, especially for the VLWIR, as their absorption coefficients had a larger difference at all temperatures. However, the benefit of an increased absorption coefficient is only important if the dark current is not significantly greater than non-symmetric structures. This is because an increase in dark current would reduce the signal-to-noise ratio of photocurrent measurements.

The temperature dependence of current density is a significant property to understand, due to superlattices photodiodes being operated at temperatures down to 77 K. Ideally they would be operated at room temperature for ease of use, however low temperature operation is required to minimise dark currents. It is well known that the dark current will increase rapidly when the bandgap reduces. If the wavelength of interest is near the superlattice cutoff wavelength, any change in bandgap could change the absorption coefficient by an order of magnitude. Therefore the cutoff wavelength, operation wavelength and dark current need to be carefully considered when designing IR photodiodes.

Modelling to identify the dominant design feature that controls the dark current density is important prior to growth of the structure to minimise the production cost.

Key results in this chapter are:

- Simulated and measured current densities of InAs/GaSb and InAs/GaAsSb T2SL structures are in good agreement showing that nextnano++ [1] current density simulations are reliable.
- In InAs/GaAsSb T2SLs with identical thickness for InAs and GaAsSb, the dark current drops by ~ 4 orders of magnitude when the temperature drops from 200 K to 77 K. Analysis of activation energy suggests that the dominant dark current mechanism is generation-recombination in MWIR diodes but is diffusion dominated in LWIR and VLWIR diodes. Using the dark current density of 10^{-5} Acm^{-2} as a performance indicator, structures with cutoff wavelengths below $8 \mu\text{m}$ can meet this requirement at an operating temperature of 77 K. 10^{-5} Acm^{-2} was chosen as a benchmark as it is the dark current predicted by rule 07 at 77 K [2].
- For a fixed thickness of InAs layer, changing the thickness of GaAsSb has a weak effect in changing the bandgap. For example with a 7 ML InAs, changing GaAsSb layer thickness from 7 to 20 ML only increases the dark current density at 77 K by 2 orders of

magnitude. The rate of change of dark current with temperature remains similar independent of the thickness of GaAsSb.

- Simulation results suggest that changes in InAs thickness had a larger effect on the current density. When the thickness of GaAsSb was fixed to 7 ML and the thickness of InAs was varied from 7 to 20 ML, the dark current density at 77 K increases by ~ 3 orders of magnitude. The dark current decreases exponentially with temperature at a similar rate for all the structures simulated.
- When different T2SL diodes with cutoff wavelengths of 10, 13 and 18.5 μm at 77K are analysed, the dark current densities from different designs, with a similar cutoff wavelength, are similar too. However in a design with a more similar thickness of InAs and GaAsSb, the absorption coefficient is higher and hence can produce a higher signal to noise ratio.
- When the generation-recombination current was removed the dark current at 140 K drops by 2 orders of magnitude in the LWIR diode with a 20 ML InAs/9 ML GaAsSb period. Similar observation was made at 300 K confirming that the generation recombination can be a major dark current mechanism.

6.2. Current density model validation

A detailed order and flow of the current density simulations performed in nextnano++ are shown in Figure 6.1.

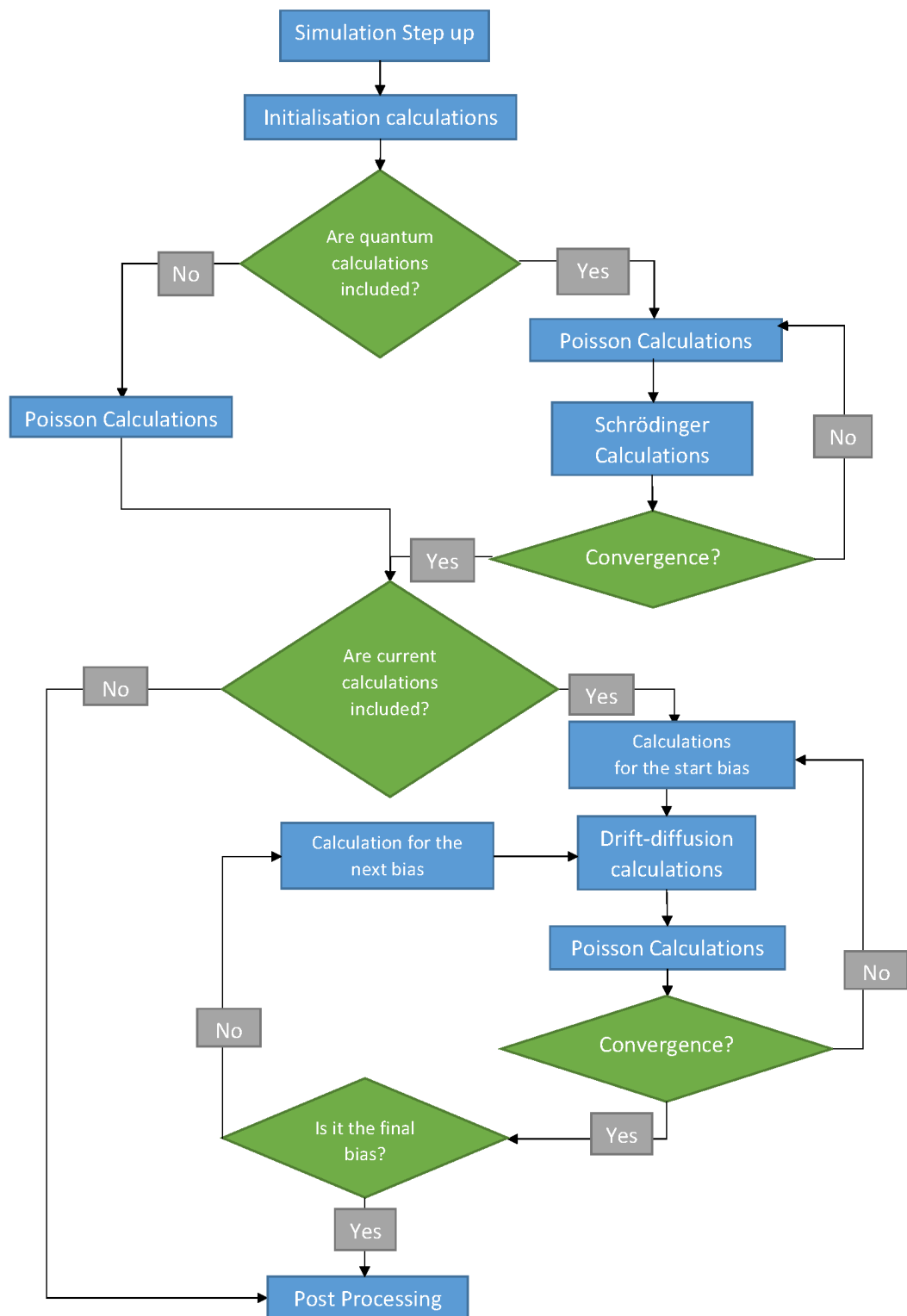


Figure 6.1: A flow chart of the program flow for the current density simulations for photodiode devices

The default simulation conditions were investigated by simulating the current density of a GaAs PN at 300, 200 and 77 K. The results in Figure 6.1 show no change in the current density in the

reverse bias, which clearly indicates errors in the simulation. In the forward bias the turn on voltages increases with decreasing temperature as expected, but no temperature dependence was observed at the lower bias voltages from 0 to 0.5 V. To improve the simulation the parameters for the current density calculations were investigated.

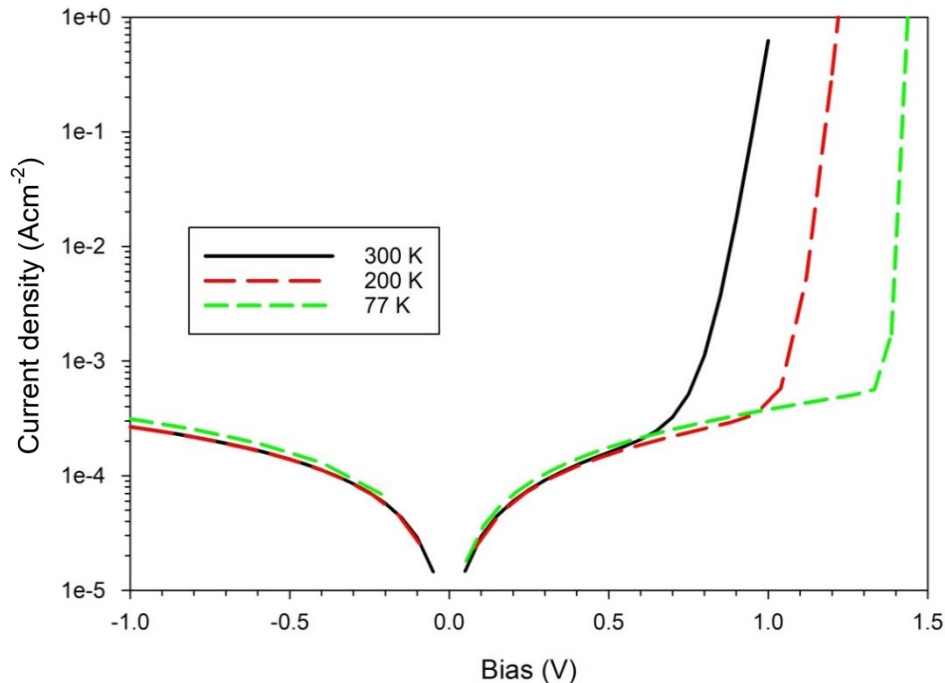


Figure 6.2: The current density of a GaAs PN structure at 77, 200 and 300 K

First the carrier densities of electrons and holes were investigated. In nextnano++ the carrier densities is calculated at each grid point through the structure, the acceptable value for each of the carrier densities is limited to be between the minimum and maximum carrier densities. The lowest value of minimum carrier density allowed is $1 \times 10^{-10} \text{ cm}^{-3}$, this is unphysical and far too small for a semiconductor. The value is used as a stop point, therefore if the carrier densities calculated are as small this value the simulation fails as the carrier concentration is unphysical.

However, as the simulation converges more easily when a small carrier density range is used, the minimum and maximum carrier densities need to be adapted for each simulation.

Nextnano++ current calculations use the drift-diffusion equations to calculate the current density which is described in equation (6.1),

$$J = qn_i\mu_n E + qD_e \frac{dn}{dx} \quad (6.1)$$

where n_i is the intrinsic density, the square root of product of the two carrier densities. E is the electric field applied, μ_n is the carrier mobility with units $\text{cm}^2\text{V}^{-1}\text{s}^{-1}$, q is the charge of an electron and D_e is the diffusion coefficient. The simulation in Figure 6.2 shows the effects of varying the minimum carrier density value on the current density of a GaAs PN diode. The results show a

significant drop of reverse current density when the minimum carrier density is changed from 1×10^7 to $1 \times 10^{-1} \text{ cm}^{-3}$. Further reduction in the minimum carrier density to $1 \times 10^{-8} \text{ cm}^{-3}$ and lower does not produce significant change in the current density. Some simulation noise is notable in the reverse bias, but this does not show a clear dependence on the value of minimum carrier density used.

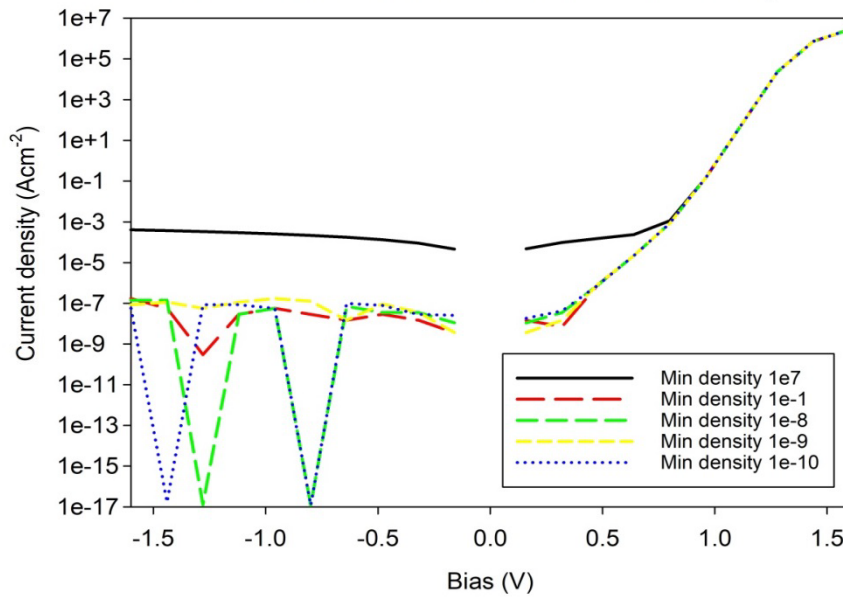


Figure 6.3: Current density simulations of a GaAs PN at 300 K using various minimum carrier density values

The GaAs PN structure in Figure 6.3 was re-simulated using the minimum carrier density of $1 \times 10^{-9} \text{ cm}^{-3}$ at temperatures from 77 to 300 K. There is a clearer temperature dependence trend in the forward bias current-density. However, the current density seems to be limited to approximately $1 \times 10^{-6} \text{ Acm}^{-2}$ at low forward bias voltages and at the reverse bias voltages.

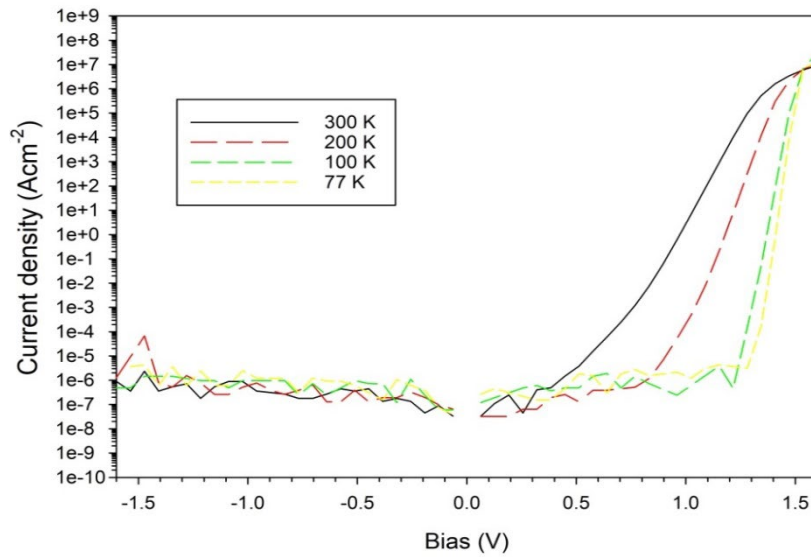


Figure 6.4: The current density of GaAs PN structure at multiple temperatures with a minimum carrier density of $1 \times 10^9 \text{ cm}^{-3}$

Next, the influence of the maximum carrier density was investigated. The default maximum carrier density is $1 \times 10^{30} \text{ cm}^{-3}$; this is unphysical and far too large for a semiconductor. The large value is used as a stop point, where the carrier density is too large even for laser calculations; therefore if the carrier densities are as large as this then the simulation fails as the carrier concentration is unphysical. The GaAs PN diode was re-simulated in Figure 6.4. The results have improved with the adjusted values for the maximum carrier density, which was changed from $1 \times 10^6 \text{ cm}^{-3}$ at 100 K, to $1 \times 10^8 \text{ cm}^{-3}$ at 300 K. The results are closer to the expected values with temperature, though the 100 K current-density results would be too low to verify experimentally.

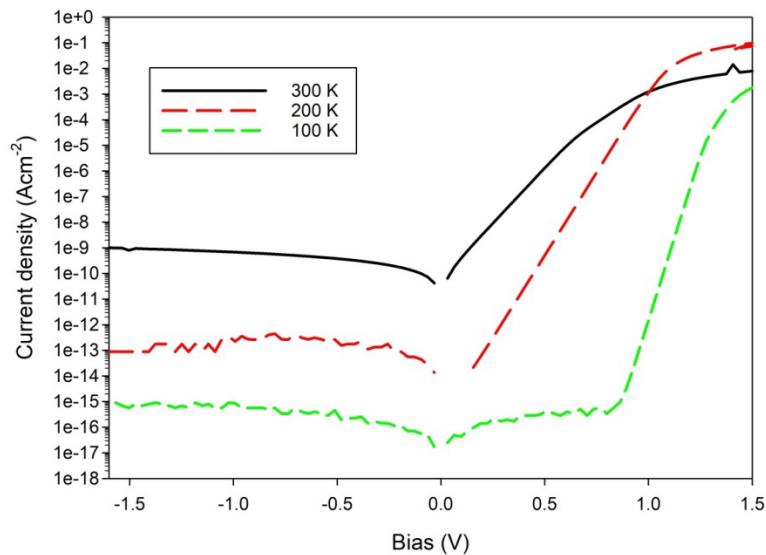


Figure 6.5: Current density calculations for GaAs PN at the temperatures 300 K, 200 K, 77 K with a minimum carrier density of $1 \times 10^9 \text{ cm}^{-3}$ and a maximum carrier density ranging from $1 \times 10^6 \text{ cm}^{-3}$ to $1 \times 10^8 \text{ cm}^{-3}$.

The results demonstrated the need to select appropriate values of minimum and maximum carrier densities to simulate current density range of interest.

6.2.1. InAs PIN verification

An InAs PIN was simulated and compared to experimental results, from our group [3]. These experimentally measured dark current densities were confirmed to originate from the bulk of the semiconductor, rather than the surface of the photodiode at temperatures above 200 K. Three temperatures were simulated from 77 K to 300 K the results are shown in Figure 6.6, while the structure of the sample is shown in the Table 6.1.

Table 6.1: The layer structure PIN photodiode from [3]

Region	Thickness (nm)	Doping (cm ⁻³)
P	1500	5x10 ¹⁷
I	6000	2x10 ¹⁵
N	3500	5x10 ¹⁷

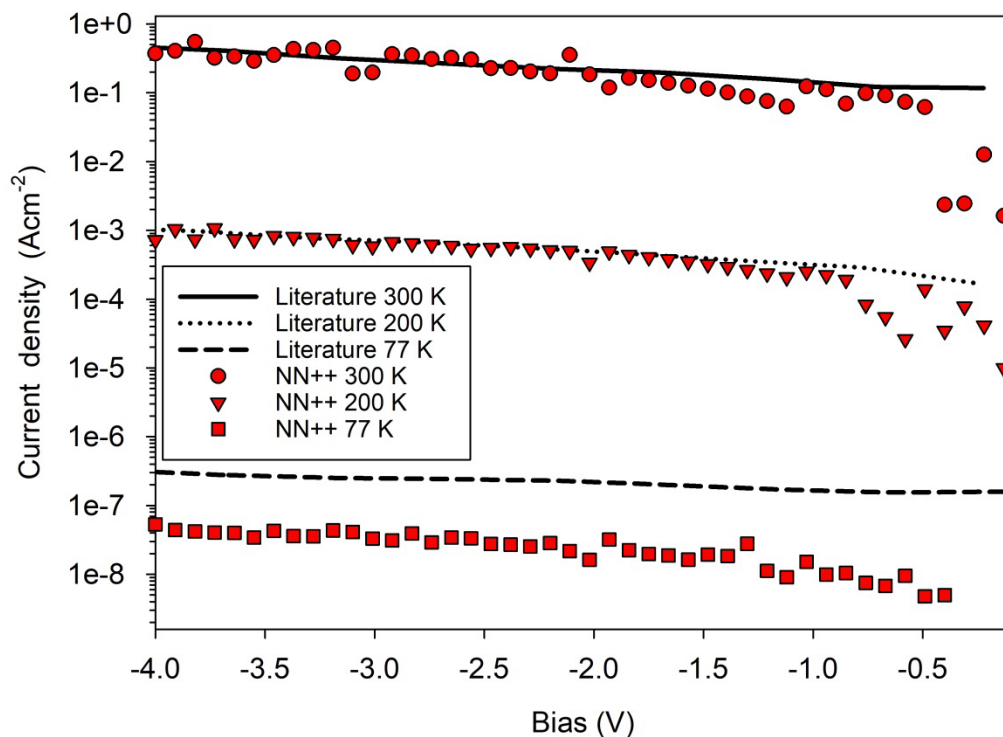


Figure 6.6: The PIN InAs from [3] compared to next nano simulations

The results in Figure 6.6 show good agreement with the experimental results at 300 K and 200 K, the slight fluctuations in results are likely to be due to convergence issues. At 77 K, the simulated current density is lower than the experimental results from [3]. Analysis of the results in [3] show the device is diffusion dominant at the temperatures of 200 and 300 K. However, at 77 K

generation-recombination current, surface leakage current and background induced current become more dominant, this could cause the discrepancy observed at 77 K. The number iterations for the current density equation was increased from 300 to 1000 to achieve smoother current density curves, though this did significantly increase the simulation time.

6.2.2. *InAs/GaSb PIN superlattice verification*

With good agreement between simulated and measured dark currents for InAs, simulations of a MWIR 6 ML InAs/7 ML GaSb superlattice PIN were compared to experimental results [4]. The cutoff wavelength of the superlattice PIN is 5 μm and the simulated results are shown in Figure 6.7.

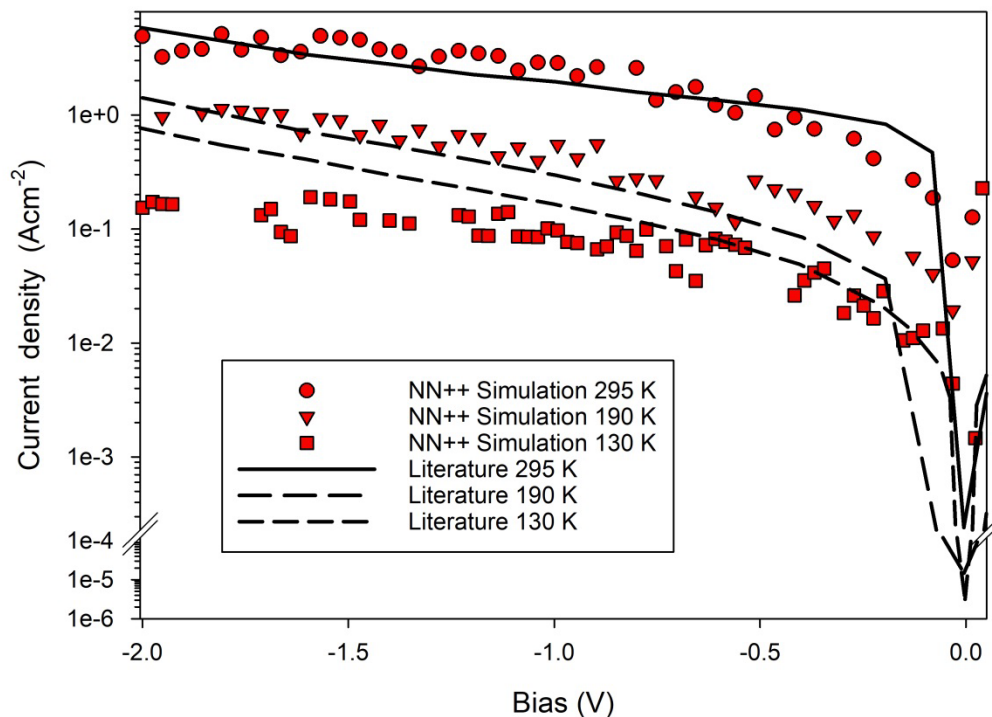


Figure 6.7: 6 ML InAs/7 ML GaSb superlattice PIN for three temperatures 130 190 and 295 K [4].

These results agree well at 295 K, with some fluctuations in the current density results. At 190 K there were more fluctuations in the current density results, possibly caused by the number of iterations being too low for the simulation to converge completely. The 130 K results deviate even further from the literature, confirming that nextnano++ simulations provide better agreement at higher temperatures.

6.2.3. *InAs/GaAsSb PIN superlattice verification*

Having achieved good agreement in InAs/GaSb T2SL, simulations were extended to InAs/GaAsSb T2SL. Current density simulations for a LWIR 20 ML InAs/9 ML GaAsSb PIN superlattice at 140, 120 and 77 K were performed and compared to experimental results from [5]. This is an important paper to validate the current-density against, as this is the same paper used

for the E_g and cutoff wavelength validation. The nextnano++ simulation results compared to [5] are shown in Figure 6.8. Very good agreement was achieved at temperatures of 120 and 140 K.

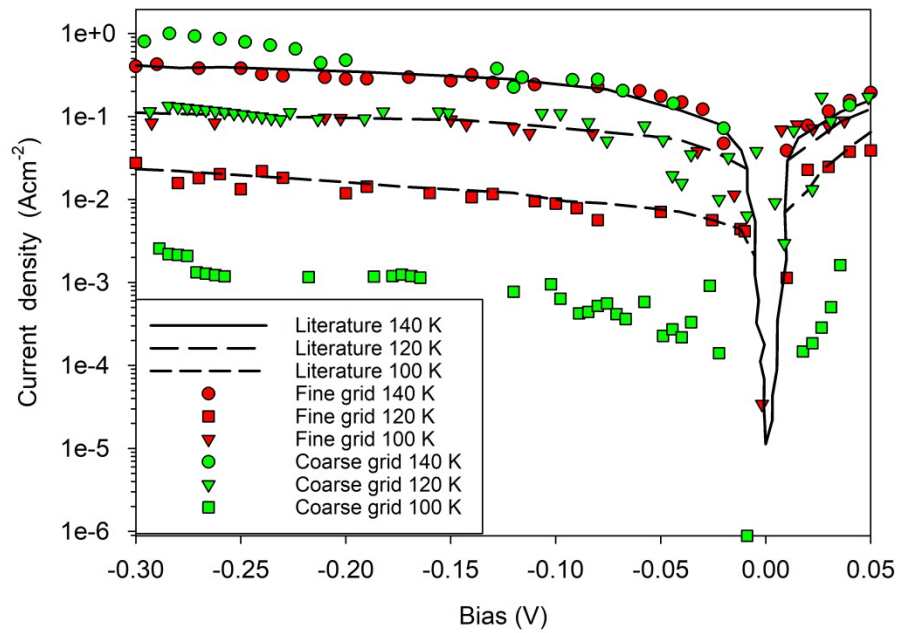


Figure 6.8: 20 ML InAs/9 ML GaAsSb simulation results with a coarse and fine grid at the temperatures 100, 120 and 140 K compared to [5].

As the current density simulations are for much larger structures than those used for the bandgap simulations the computational time increased. To decrease computational time a coarse grid simulation was trialled. The original grid had a spacing of 0.5 \AA between each grid point which is roughly 6 grid points per monolayer, whereas the coarse grid gives about 1 grid point per monolayer. The results in Figure 6.8 show that the number of grid points has a significant effect on the accuracy of the results at 100 K. The results for the coarser grid are reasonably close in the reverse and forward bias compared to the literature results at higher temperatures. However the simulated results agree better with the results from [5] at 100 K when the fine grid was used. The fine grid was used for the rest of this chapter.

6.3. Current density results

The simulations using the fine grid were more accurate, at the expense of a long computational time. To reduce the simulation time and to investigate whether diffusion current is dominant in the next nano simulations, the effect of the size of the i-region on the current density simulation was investigated. The same structure from [5] was simulated, but with a 10 quantum well n-region and p-region instead of the 55 in [5], and a i-region of 10, 20 30 and 100 quantum wells, instead of 285.

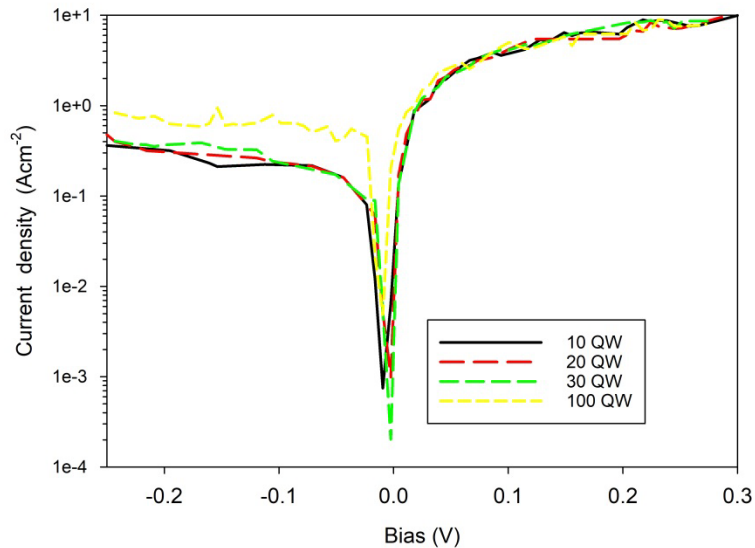


Figure 6.9: Current density of a 20 ML InAs/9 ML GaAsSb at 200 K for 10, 20, 30 and 100 quantum wells

The results in Figure 6.9 show that the current density at 200 K is higher when the number of quantum wells in the i-region is increased to 100. This indicates that the generation-recombination current has a significant effect on the current density results. The computational time was greatly affected by the number of quantum wells, 10 quantum wells finished 2 hours faster than the 30 quantum wells simulation and 10 hours faster than the 100 quantum well structure. The 100 quantum well structure's forward bias is very close to the other results, and the reverse bias is on average 0.2 Acm^{-2} higher than the smaller simulations. The increase in current density shows the effect of the generation-recombination current, as diffusion current would be unaffected by the size of the i-region. The 10 quantum well structure is used for the rest of this chapter, as the results are in the same order of magnitude and the simulations are used as a qualitative indication of the dark current trend.

6.3.1. *InAs/GaAsSb superlattices with a symmetrical structure*

Using the conditions established in the previous sections, the current-density simulations of symmetrical InAs/GaAsSb PIN photodiodes were conducted. Simulations were performed at 77, 100, 150, and 200 K, with period thicknesses ranging from 14 ML (7 ML InAs/7 ML GaAsSb) to 40 ML (20 ML InAs/20 ML GaAsSb). The simulations used the default current parameters from nextnano++ for the mobility of electrons and holes etc. These values were taken from the Vurgaftman parameter paper [6] and are listed in appendix A. These parameters were also used in the validation simulations earlier. The minimum and maximum carrier density values were altered for the simulations. The values used in these simulations ranged from $1e^{-9} \text{ cm}^{-3}$ for the 40 ML structure and $1e^{-7} \text{ cm}^{-3}$ for the 14 ML structure, the maximum carrier density was set at $1e^7 \text{ cm}^{-3}$. Though the range of values is large, and is unlikely for semiconductors, this creates a range that aids the iteration process. The range of values chosen was the smallest range of carrier density the

simulation could use and still converge on an answer. Throughout the simulations in this chapter the maximum carrier density does not go above $1e^8 \text{ cm}^{-3}$ and the minimum carrier density does not go below $1e^{-9} \text{ cm}^{-3}$.

At 77 K, increasing the period from 14 to 40 ML increases the cutoff wavelength from 4.64 μm to 18.5 μm . The corresponding change in cutoff wavelength is 5.19 μm to 27.0 μm at 200 K. Figure 6.10 shows the dark current density at a bias of -0.1 V. The results show strong temperature dependence. For discussion in this chapter, the operation temperature is assumed to be 77 K, when the structure needs to be classified as MWIR, LWIR or VLWIR. In the MWIR structure with a 14 ML superlattice period, the current density decreases from $1.77 \times 10^{-2} \text{ Acm}^{-2}$ at 200 K, to $1.02 \times 10^{-6} \text{ Acm}^{-2}$ at 77 K a difference of 4 orders of magnitude. In the LWIR structure with a 32 ML superlattice period, the current density decreases from 3.64 Acm^{-2} to $4.12 \times 10^{-4} \text{ Acm}^{-2}$, a difference of 5 orders of magnitude. Under the same conditions, the temperature dependence appears to be similar for the different superlattice periods. In the VLWIR structure with a 40 ML period, the current density decreases from 8.92 Acm^{-2} at 200 K to $9.3 \times 10^{-3} \text{ Acm}^{-2}$, again a different of 4 orders of magnitude.

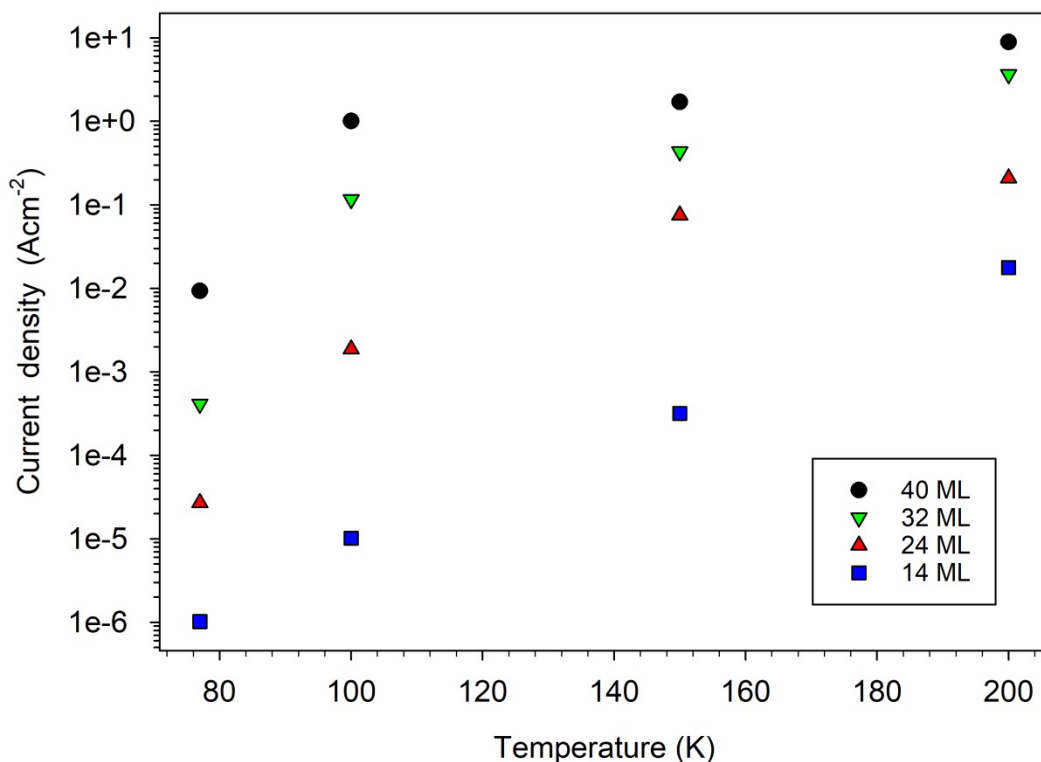


Figure 6.10: The current density for PIN structures with symmetrical periods InAs/GaAsSb at a bias of -0.1 V

The Arrhenius plots in Figure 6.11 were used to estimate the activation. However, the plots did not show obvious gradients that can be used to extract the activation energies. A reasonable estimate was obtained in the MWIR structure with a 14 ML period. For temperatures below

150 K the activation energy was calculated to be 0.126 eV, this is close to half the value of E_g for this structure (0.267 eV at 77 K) suggesting generation recombination current is dominant.

The LWIR structure below 150 K has activation energy of 0.09 eV (32 ML period) this is close to the bandgap of the structure (0.104 eV at 77 K) suggesting the structure is diffusion current density dominant. The VLWIR structure at temperatures below 150 K has activation energy of 6.65×10^{-2} eV (40 ML period) this is the same as the bandgap of the structure (6.72×10^{-2} eV at 77 K) showing the structure is diffusion dominant.

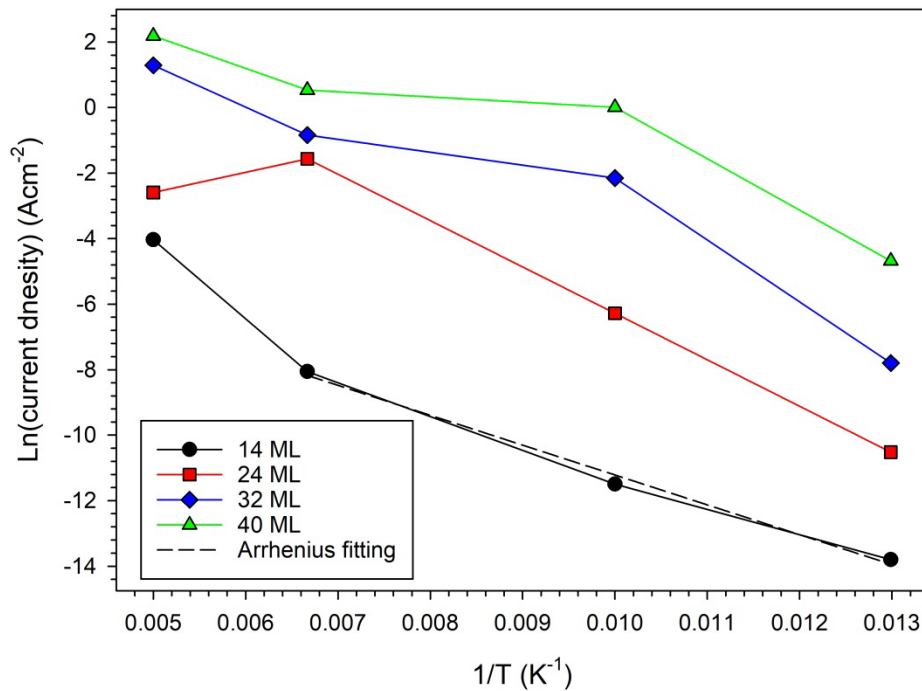


Figure 6.11: the Arrhenius plot for the symmetrical structures with period sizes from 14 ML to 40 ML InAs/ GaAsSb at -0.1 V

The results are consistent with that expected from dark current theory. In general a smaller bandgap causes the diffusion current to increase as the carrier density in the diffusion current is proportional to $\exp\left(-\frac{E_g}{k_B T}\right)$. When analysing dark current in an infrared photodiode, a useful dark current density benchmark is 1×10^{-5} Acm⁻², which is the predicted current density for a MCT photodiode at 77 K. Figure 6.10 shows this benchmark value can be achieved in the MWIR structure with a 14 ML period operating 100 K and the in the LWIR structure with a 32 ML period operating at 77 K. The dark current density results for the VLWIR structure with a 40 ML period are higher and will require lower operating temperatures. By extending the Arrhenius plot the VLWIR structure is predicted to achieve 1×10^{-5} Acm⁻² at a temperature of 45 K.

6.3.2. InAs/GaAsSb superlattices with a 7 ML thick InAs well

To investigate the influence of the thickness of the GaAsSb layer on the current density, a series of simulations of a PIN photodiode were conducted at 77, 100, 150 and 200 K. The structures had a 7 ML thick InAs well and the GaAsSb barrier was changed from 7 to 20 ML thick. At 77 K, changing the GaAsSb barrier thickness from 7 to 20 ML increased the cutoff wavelength from 4.64 to 4.78 μm . At 200 K the cutoff wavelength increases from 5.19 to 5.21 μm . It is clear the effect of changing the GaAsSb on the cutoff wavelength is weak. Figure 6.11 suggested that the dominant current process in the MWIR diode is generation recombination. In Figure 6.12 the current density of all MWIR diodes reduce by approximately 4 orders of magnitude, as temperature decreases from 200 to 77 K, which is consistent with the results in Figure 6.10. At 77 K the 7 ML InAs/7 ML GaAsSb has a current density of $1.0 \times 10^{-6} \text{ Acm}^{-2}$, the 7 ML InAs/12 ML GaAsSb ($1.5 \times 10^{-5} \text{ Acm}^{-2}$), and the 7 ML InAs/14 ML GaAsSb ($2.9 \times 10^{-5} \text{ Acm}^{-2}$). All three structures have current densities low enough for use in a thermal camera, the 7 ML InAs/7 ML GaAsSb structure also satisfies the requirement at 100 K. Arrhenius plots of these MWIR superlattices suggest that generation recombination is the dominant dark current mechanism. Though it should be noted that the simulations assume that the lifetime of the carriers are not affected by the period of the superlattice.

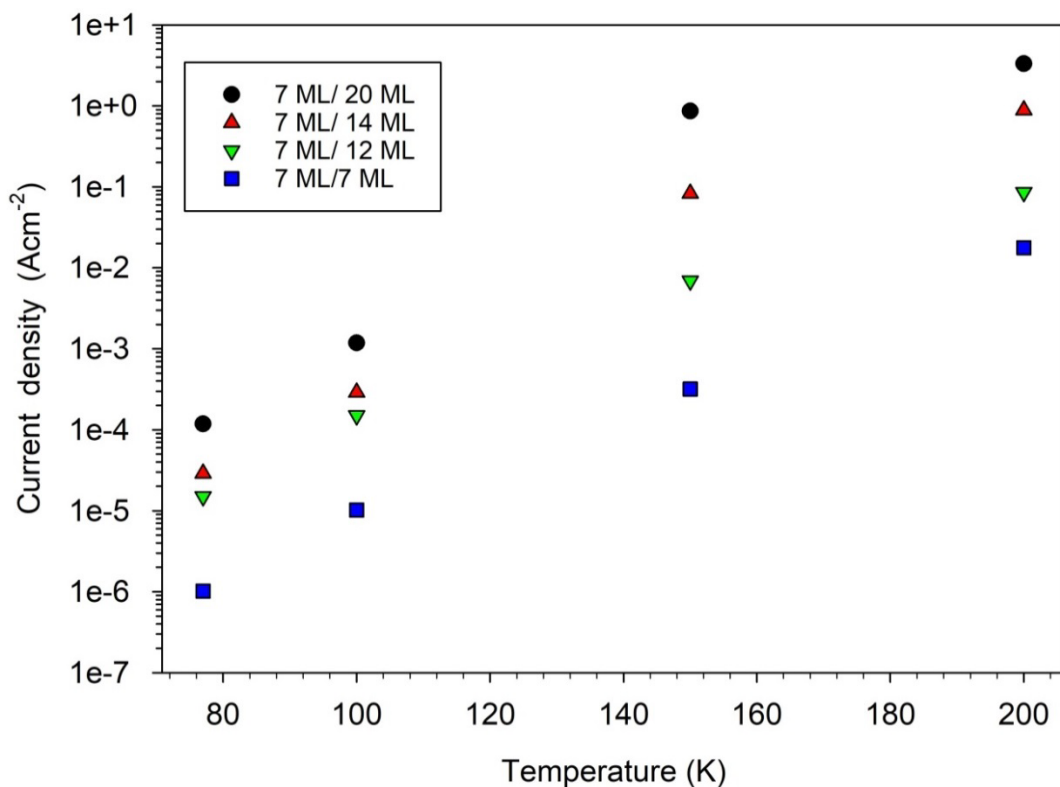


Figure 6.12: Current density of 7 ML InAs/GaAsSb superlattices with increasing GaAsSb thickness at the bias -0.1 V at the temperatures 77, 100 150 and 200 K

6.3.3. *InAs/GaAsSb superlattices with a 7 ML GaAsSb barrier*

Superlattices with a fixed GaAsSb barrier size of 7 ML and an InAs well varying from 7 ML to 20 ML were also calculated at different temperatures of 77, 100, 150 and 200 K. This is expected to have a larger change in the current density, as a change in InAs thickness has a larger effect on the bandgap as seen in the previous chapters.

The results in Figure 6.13 show the current density of each structure at -0.1 V. They show that as the size of the well increases the current density of the superlattice increases. The dark current in the MWIR structure (7 ML InAs/7 ML GaAsSb) shown in Figure 6.12 is generation recombination dominated.

The LWIR structure (20 ML InAs/7 ML GaAsSb) has a cutoff wavelength of 10.3 μm at 77 K. The current density changes from $2.05 \times 10^{-3} \text{ Acm}^{-2}$ at 77 K, to 3.15 Acm^{-2} at 200 K. This is not low enough to be suitable for use in a thermal camera. Lowering the temperature to 50 K yields a current density of $1.81 \times 10^{-4} \text{ Acm}^{-2}$. The arrhenius plot for this structure show that the activation energy of this sample below 150 K is 0.08 eV, which is more than half the bandgap of the superlattice at 77 K (0.12 eV). This suggests diffusion current is more dominant at all temperatures below 150 K, and extending the plot showed that $\leq 1 \times 10^{-5} \text{ Acm}^{-2}$ is achieved at temperatures below 45 K.

The current density values change by four orders of magnitude current density when the thickness of InAs is changed from 7 ML to 20 ML, confirming that the current density is strongly dependent on the thickness of InAs well. The results also show very good agreement to experimental results [5] obtained from a 20 ML InAs/9 ML GaAsSb superlattice structure as shown by the stars in Figure 6.13.

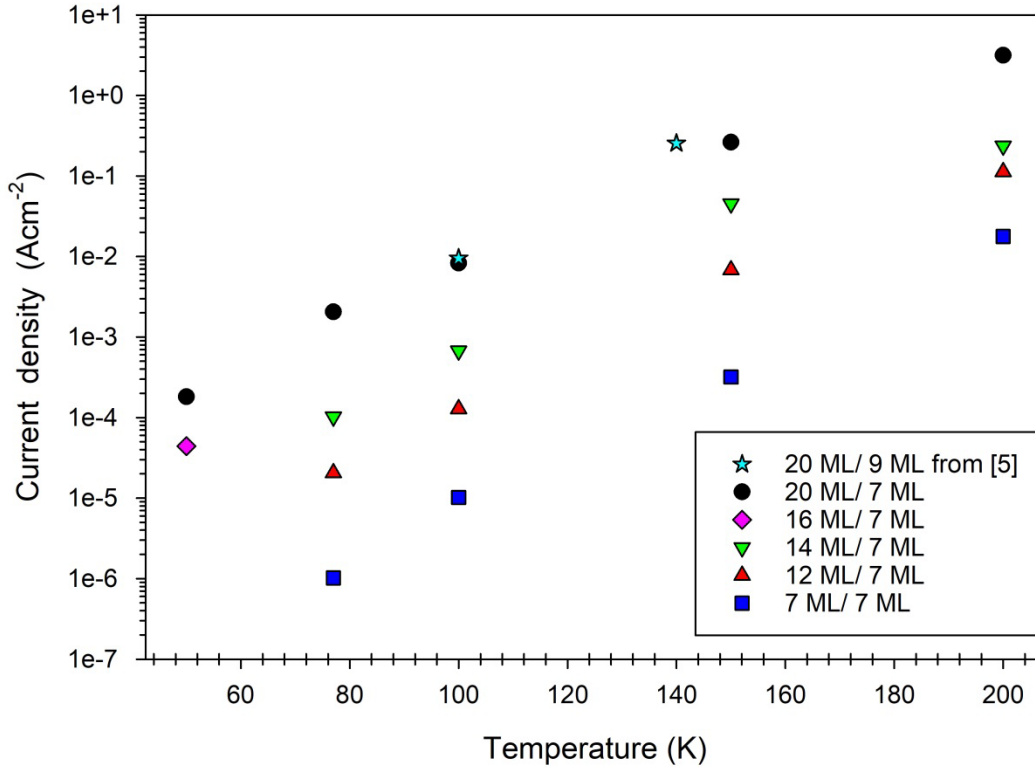


Figure 6.13: Current density of InAs/GaAsSb PIN with I-region of 10 quantum wells at -0.1 V at temperatures of 50,77,100,150 and 200 K. The GaAsSb barrier was fixed at 7 ML with the InAs layer increasing from 7 ML to 20 ML. Literature results for 20 ML InAs/9 ML GaAsSb PIN are also included (stars) [5].

6.4. Comparing InAs/GaAsSb superlattices with the same cutoff wavelengths at 77 K

Results from previous chapters showed for structures with similar cutoff wavelengths, the more symmetrical structure has higher absorption coefficients at all temperatures. It is important to understand how the current-density of the structures compare, to inform which period is superior for certain wavelengths. Simulations were performed to compare the current density of structures with the same cutoff wavelength at 77 K.

6.4.1. Structures with a cutoff wavelength of 10 μm at 77 K

InAs/GaAsSb structures with a LWIR cutoff wavelength of 10.3 μm at 77 K suggested by previous bandgap simulations are 16 ML InAs/10 ML GaAsSb and 20 ML InAs/7 ML GaAsSb. Figure 6.14 shows very little difference in the current-density for the two structures. This suggests that the dark current is largely dependent on the bandgap and not the relative thicknesses of the InAs and GaAsSb layers. However, it is worth noting that the simulation, being an “ideal” photodiode, does not include defects that could arise from growing different thicknesses of the

GaAsSb, for example whether the effect of Sb segregation. The assumption that the carrier lifetime for structures with the same cutoff wavelength is the same will need to be evaluated using experimental data.

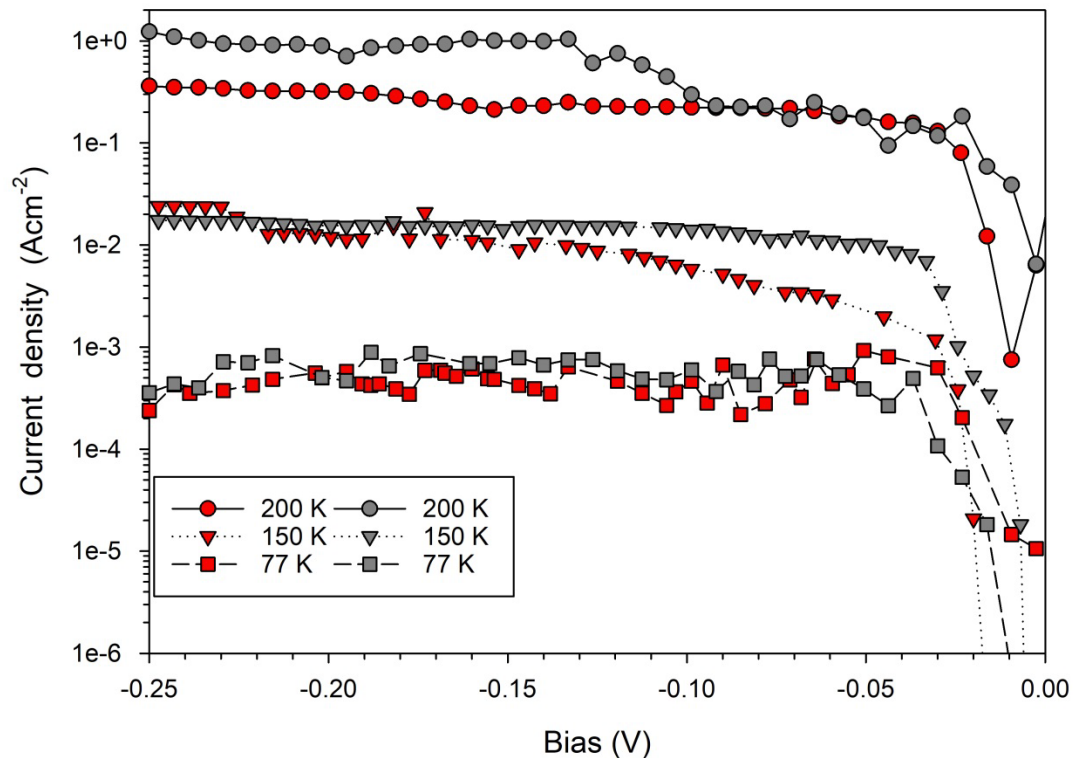


Figure 6.14: The current density of 2 PIN superlattice structures with the same cutoff wavelengths at multiple temperatures, 16 ML InAs/10 ML GaAsSb (grey) and 20 ML InAs/7 ML GaAsSb (red)

Overall comparing the results in chapter 5 figure 5.7 and Figure 6.14 it is implied that the symmetrical structure has an advantage. As the two structures have a similar cutoff and dark current, but the symmetrical structure has slightly higher absorption, averaging 150.2 cm^{-1} (at the wavelength of $8 \mu\text{m}$ in Table 5.4) over the temperature range from 77 K to 300 K.

To analyse which is the better superlattice to operate at $8 \mu\text{m}$ at 77 K the quantum efficiency was calculated from the absorption coefficient. This value was then compared to the dark current-density to provide a performance indicator. Previous simulations showed the structures 16 ML InAs/10 ML GaAsSb and 20 ML InAs/7 ML GaAsSb have absorption coefficients at $8 \mu\text{m}$ of 177.94 cm^{-1} and 31.5 cm^{-1} respectively at 77 K, this is summarised in the Table 6.2.

Table 6.2: Comparison of the absorption coefficient and current- density for 16 ML InAs/ 10 ML GaAsSb and 20 ML InAs/ 7 ML GaAsSb at $8 \mu\text{m}$ at 77 K

Temperature 77 (K)	16 ML InAs/10 ML GaAsSb	20 ML InAs/7 ML GaAsSb	Difference

The absorption coefficient at 8 μm (cm^{-1})	177.94	31.57	143.37
Current density a -0.05 V (Acm^{-2})	5.327×10^{-4}	4.239×10^{-4}	1.08×10^{-4}
Quantum efficiency (%)	4.12	0.772	3.35

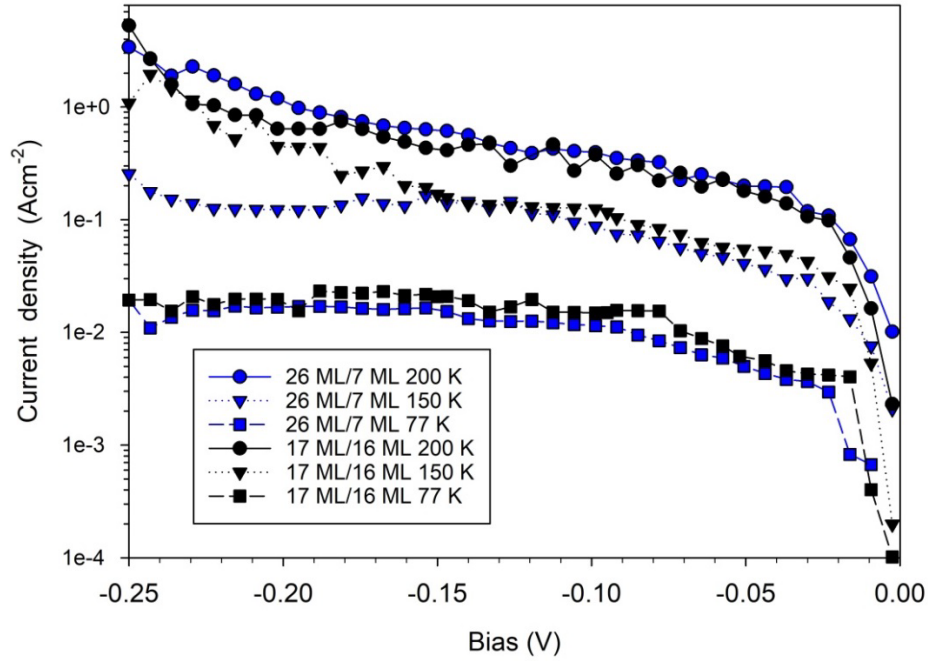
The quantum efficiency (η) definition used for this analysis is

$$\eta = 1 - e^{-\alpha(\lambda)L}$$

where L is the thickness of the detector, $\alpha(\lambda)$ is the absorption coefficient at a set wavelength. For the purpose of these comparisons the thickness of the structure is taken to be 300 periods of the superlattice, a typical PIN photodiode thickness. It is clear that a higher quantum efficiency is achieved in the more symmetrical structure. However the value is low suggesting that a thicker absorption region is needed. Absorption enhancement features to achieve multi-pass absorption will also be needed to increase the overall quantum efficiency.

6.4.2. Structures with cutoff wavelength 13 μm at 77 K

A pair of structures with a cutoff wavelength close to VLWIR were simulated in Figure 6.16 to assess the current-density of 17 ML InAs/16 ML GaAsSb and 26 ML InAs/7 ML GaAsSb. At 77 K both structures had a cutoff wavelength of 13 μm . The current density for these devices is higher than the results in Figure 6.14 as they have a smaller E_g . As before there is no obvious difference in the current density. In practice the surface leakage, growth and fabrication issues, arising from different thicknesses of InAs and GaAsSb, may cause one structure to be more favourable for real devices.



Comparing results from chapter 5 Figure 5.8 and Figure 6.16 it can be concluded that the symmetrical structure has a slight advantage. The two structures have a similar cutoff, similar dark current, but the symmetrical structure has a higher average absorption coefficient value of 190.3 cm^{-1} (see Table 5.5) over the temperature range.

The absorption coefficient at $10 \mu\text{m}$ for the two structures at 77 K is 200.4 cm^{-1} (17 ML InAs/16ML GaAsSb) and 30.2 cm^{-1} (26 ML InAs/7 ML GaAsSb). These values are shown in Table 6.3. As before, the more symmetrical structure is more favourable.

Table 6.3: Comparison of the absorption coefficient for 17 ML InAs/16 ML GaAsSb and 26 ML InAs/7 ML GaAsSb at $10 \mu\text{m}$ 77 K

Property at 77 K	17 ML InAs/16 ML GaAsSb	26 ML InAs/7 ML GaAsSb	Difference
The absorption coefficient (cm^{-1})	200.4	30.2	170.2
Current density at -0.05 V (Acm^{-2})	6.8×10^{-3}	5.2×10^{-3}	1.6×10^{-3}
Quantum efficiency (%)	5.84	0.902	4.94

6.4.3. Structures with a cutoff wavelength of 18 μm at 77 K

The superlattice structures 20 ML InAs/20 ML GaAsSb and 22 ML InAs/12 ML GaAsSb have a cut off wavelength close to 18.5 μm at 77 K. The absorption coefficient of these two structures at 15 μm is 127.15 cm^{-1} and 14.23 cm^{-1} respectively. Assuming that the devices will be used to detect a wavelength at 14 μm , the 20 ML InAs/20 ML GaAsSb structure has a high quantum efficiency, suggesting the more symmetrical structure is favourable.

Table 6.4: Comparison of the absorption coefficient for 20 ML InAs/20 ML GaAsSb and 22 ML InAs/12 ML GaAsSb at 14 μm 77 K

Property at 77 K	20 ML InAs/20 ML GaAsSb	22 ML InAs/12 ML GaAsSb	Difference
The absorption coefficient (cm^{-1})	127.15	14.238	112.7
Current density (Acm^{-2}) at -0.05 V	1.9×10^{-3}	2.6×10^{-4}	1.64×10^{-3}
Quantum efficiency (%)	4.52	0.439	4.13

6.4.4. The effect of the recombination currents

The simulated current density agrees with the measured value reported in literature. The simulated dark current seems high for “ideal” superlattice photodiodes with no surface leakage or defects. To confirm the effect of the recombination currents on the simulations, the same simulation was run with and without the recombination current contributions included shown in Figure 6.17. The recombination currents included in the simulations were Auger recombination, Schottky-Read-Hall recombination, and radiative generation recombination currents. The parameters used for the recombination currents are listed in Appendix A. The parameters used, are listed in appendix A, from the nextnano++ default database. The recombination parameters are taken from the Caughey/Thomas model [7], and the simulation depends on the temperature, the doping density and the parallel electric field.

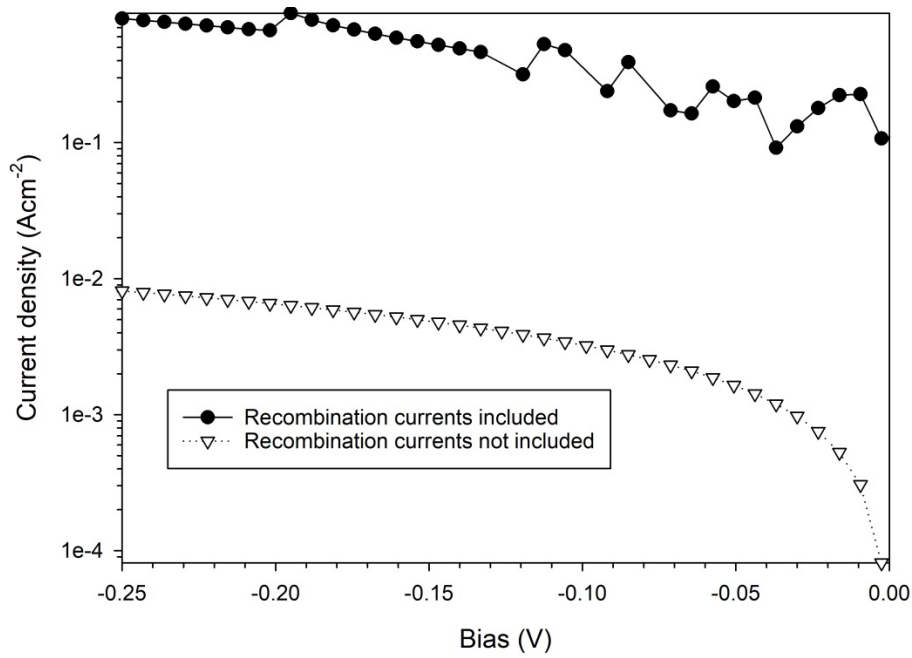


Figure 6.16: The current-density of the same structure from Figure 6.8 (20 ML InAs/ 9 ML GaAsSb) at 140 K with the recombination current contributions included and not included.

These results clearly show that the devices simulated are greatly affected by the generation-recombination contributions. To clarify the effect the recombination currents have on the current density, the InAs PIN from Figure 6.6 and [2] was simulated with and without the recombination currents included in Figure 6.18. The results showed a similar decrease in current-density when the generation-recombination currents were excluded. The recombination contributions need to be included in the simulations to make the simulations more realistic.

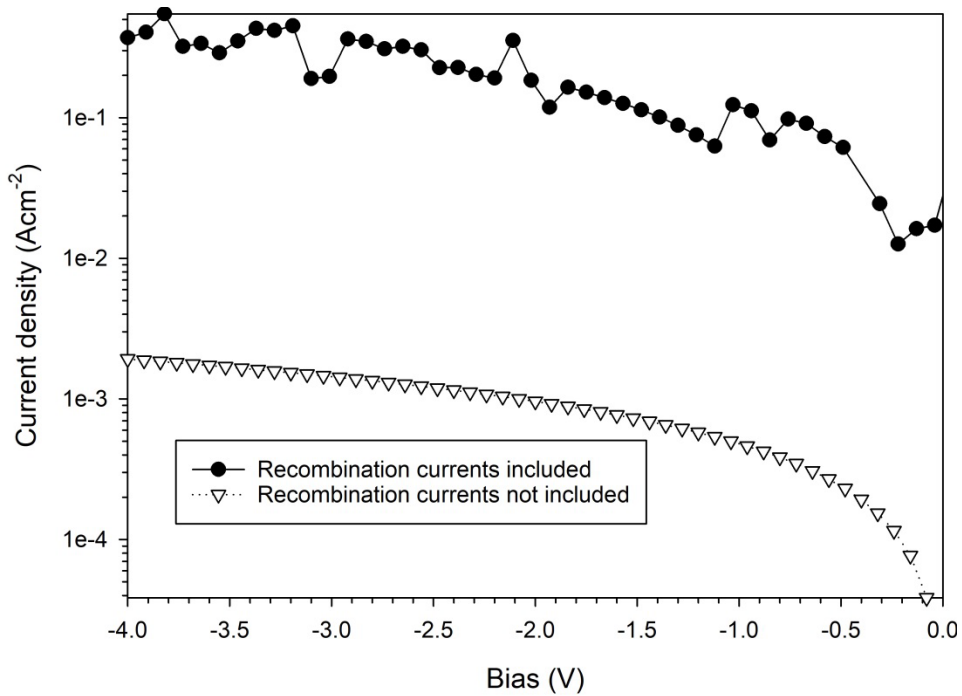


Figure 6.17: The current-density of the InAs PIN structure simulated earlier in Figure 6.6 [2], with and without the recombination current density contributions at 300 K.

6.5. Conclusion

From the results in this chapter it was concluded nextnano++ can reproduce experimentally measured dark currents in InAs/GaSb and InAs/GaAsSb structures.

Simulations of different PIN devices with the same thickness of InAs and GaAsSb layer show that the dark current increases at a similar rate with increasing temperature across designs with 7 ML InAs/7 ML GaAsSb (MWIR diode) to 20 ML InAs/20 ML GaAsSb (VLWIR diode). The activation energy analysis suggests that the generation-recombination is dominant in the MWIR diode while diffusion is more dominant in the VLWIR diode.

Changing the thickness of InAs was found to have a more pronounced effect on the bandgap and hence the dark current too. However in structures compared the dark current increases at a similar rate with increasing temperature, even when the cutoff wavelengths are different.

When two structures with similar cutoff wavelength are compared, they produce similar dark currents independent of temperature. However structures with a more similar thickness of InAs and GaAsSb have higher absorption coefficients and hence can produce higher signal to noise ratios. This trend is observed in devices with cutoff wavelengths of 10, 13 and 18.5 μm at 77 K. The simulated results suggest that it is possible to achieve a dark current density of 10^{-5} Acm^{-2} at 77 K in MWIR structures. However to achieve this level of dark current density in the VLWIR structures, lower operating temperature is predicted. The recombination current was found to be a major dark current mechanism, leading to ~ 2 orders of magnitude reduction when

removed. This implies that accurate parameters for generation-recombination are important to model the dark current in InAs/GaAsSb T2SL detectors. Based on the simulated results, reduced generation-recombination current is required so that VLWIR operating at 77 K can be achieved.

References

-
- ¹ S. Birner, T. Zibold, et al. "nextnano: General Purpose 3-D Simulations," *IEEE Trans. Electron Dev.* 54, 2137 (2007)
 - ² W. E. Tennant, D. Lee, M. Zandian, E. Piquette, and M. Carmody, "MBE HgCdTe Technology: A Very General Solution to IR Detection, Described by 'Rule 07', a Very Convenient Heuristic," *J. Electron. Mater.*, vol. 37, no. 9, pp. 1406–1410, 2008,
 - ³ Pin Jern Ker, A. R. J. Marshall, A. B. Krysa, J. P. R. David, and Chee Hing Tan, "Temperature Dependence of Leakage Current in InAs Avalanche Photodiodes," *IEEE J. Quantum Electron.*, vol. 47, no. 8, pp. 1123–1128, 2011, doi: 10.1109/JQE.2011.2159194
 - ⁴ E. Plis *et al.*, "Type-II InAs/GaSb strained layer superlattices grown on GaSb (111)B substrate," *J. Vac. Sci. Technol. B Microelectron. Nanometer Struct.*, vol. 31, no. 3, p. 3, 2013, doi: 10.1116/1.4798650.
 - ⁵ F. Wang, J. Chen, Z. Xu, Y. Zhou, and L. He, "Performance comparison between the InAs-based and GaSb-based type-II superlattice photodiodes for long wavelength infrared detection," *Opt Express*, vol. 25, no. 3, p. 1629, 2017, doi: 10.1364/OE.25.001629.
 - ⁶ I. Vurgaftman, J. R. Meyer, and L. R. Ram-Mohan, "Band parameters for III–V compound semiconductors and their alloys," *J Appl Phys*, vol. 89, pp. 5815-5875, 2001.
 - ⁷ D. Caughey, R. Thomas, "Carrier Mobilities in Silicon Empirically Related to Doping and Field," *Proc. IEEE* 55, 2192, 1967

7 Fabrication and blackbody response of InAs/GaAsSb superlattice

7.1 Introduction

Having simulated the cutoff wavelength, absorption coefficient and dark current in the previous chapters, a feasibility study of growth, fabrication and characterisation of InAs/GaAsSb T2SL was carried out. A PIN structure was designed and grown with a 50 period superlattice i-region with barriers of GaAsSb and InAs in the p-region and n-region respectively, as shown in Figure 7.1. The superlattice chosen for the i-region was 15 ML InAs/16 ML GaAsSb design which would have a cutoff wavelength of $9.5 \mu\text{m}$ at 77 K. The relatively wide bandgap barriers are designed to reduce the dark current in the structure by blocking one type of carrier from moving in one direction. One of the best dark current density results published for a LWIR device was achieved by a InAs/InAs_{0.5}Sb_{0.5} superlattice with a barrier [1]. This device achieved a dark current density of $6.3 \times 10^{-6} \text{ A cm}^{-2}$ which is ~ 1 order lower than a typical LWIR device [2].

Key results in this chapter are:

- The fabricated wafer shows diode rectifying behaviour and dark current level at 0 V at 77K to be comparable to that reported in a literature [1].
- The photoresponse to a wide range of wavelengths from MWIR to VLWIR. The peak response is when using the 9-11 μm bandpass filter.
- XRD fitting suggests that the superlattice grown was different from expected (15 ML InAs/16 ML GaAs_{0.14}Sb_{0.86})
- The response from VLWIR was attributed to a room temperature blackbody radiation signal that was reflected by the VLWIR, leading to the detected photocurrent.

7.2 Wafer details

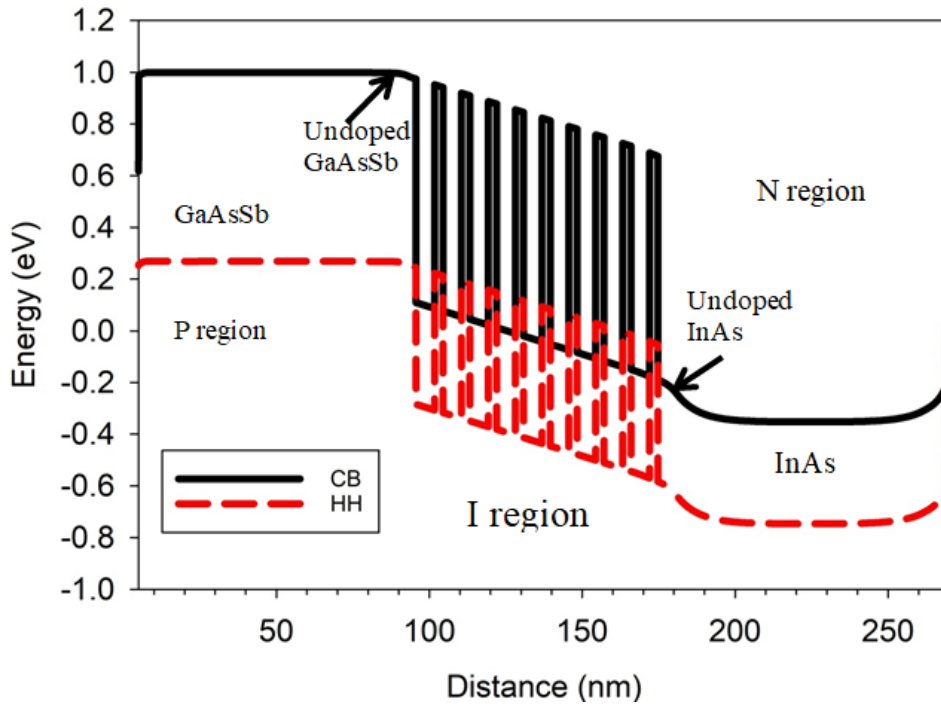


Figure 7.1: Band diagram of the barrier wafer with a superlattice in i-region and the complementary barriers in the p and n-regions at 0 V.

The wafer grown has 50 periods of 15 ML InAs/16 ML GaAsSb, the wafer structure and doping is shown in Table 7.1.

Table 7.1: Wafer design for SF1625 15 ML InAs/16 ML GaAsSb

Thickness (nm)	Material	Doping type	Doping level (cm ⁻³)
100	GaAs(0.09)Sb	P	1x10 ¹⁷ (error in the growth request)
500	GaAs(0.09)Sb	P	5x10 ¹⁷
100	GaAs(0.09)Sb	Undoped	0
4.54/4.85	InAs/GaAs(0.09)Sb x50 repeats	Undoped	0
100	InAs	Undoped	0
500	InAs	N	5x10 ¹⁷

This design aimed to reduce the dark current by reducing the intrinsic carrier concentration and hence the diffusion current in the InAs n-region and the GaAsSb p-region. The doping of the top 100 nm GaAsSb layer was low due to an error in the growth request and this may have caused some issues for creating p-type ohmic contacts.

First growth conditions to achieve a lattice matched GaAsSb on InAs, with 9 % of As, were developed. A low As condition was used for GaAsSb, but this will require switching of the As valve position when growing InAs. These conditions were used to grow the preliminary wafer grown at 460 °C. The initial superlattice PIN, SF1611, has As content of approximately 13.7 %, deduced from XRD, which is higher than the intended 9 %. This reduced Sb incorporation in the superlattice leads to lattice mismatch to the InAs substrate. In order to improve the lattice matching, to achieve the correct alloy of GaAsSb, a Sb soak was included. A Sb soak is where the Sb source was left open to grow a Sb rich interface between the layers to improve the interface. The XRD results which can be seen in Figure 7.2 and show the superlattice with the Sb soak (SF1616) has much better lattice matching, the fringe peaks are narrower unlike the peaks in SF1611.

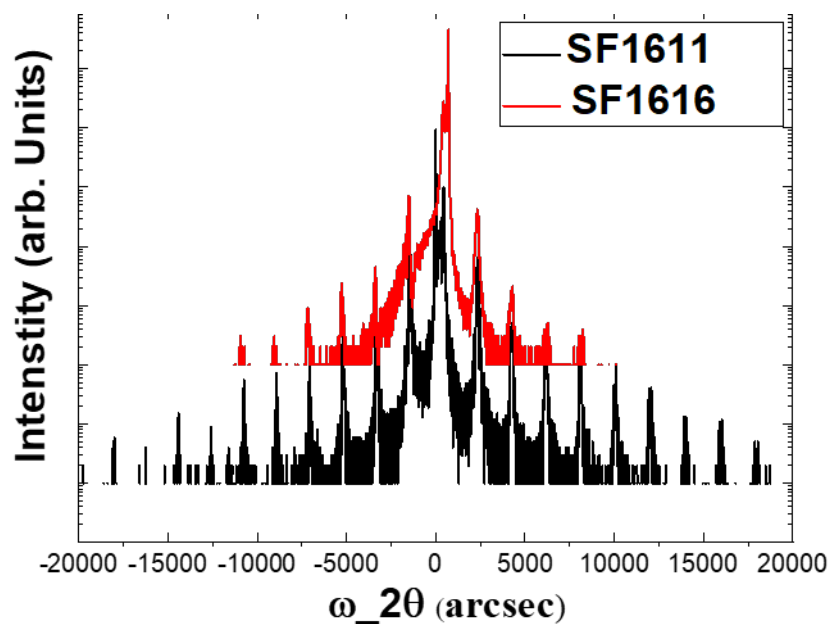


Figure 7.2: The XRD results for an InAs/ GaAsSb superlattice growth with a Sb soak (SF1616) and without (SF1611) results have been positioned to match 0th peak positions.

However, as seen in Figure 7.3 the Normanski microscopy of wafer SF1616 shows a very rough surface with “bumps” on the surface of the wafer. The roughness is thought to be metal droplets of Sb. For this reason subsequent wafers were grown without the Sb soak step.

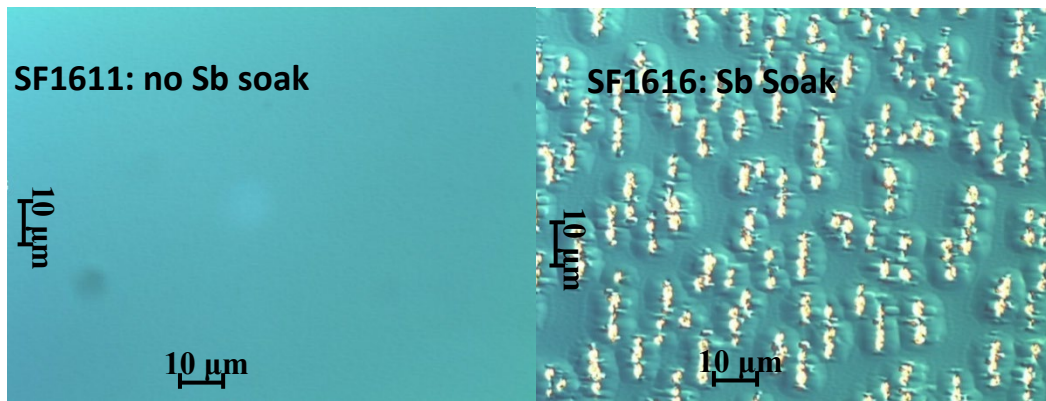


Figure 7.3: The Normarski microscopy image x 50 magnification, for wafers SF1611 grown with no Sb soak and SF1616 grown with Sb soak

A set of wafers were grown without the Sb soak method, but with increased Sb during growth of the superlattice, to compare to the wafer grown with a Sb soak. In Figure 7.4 the XRD profiles are from structures grown with the Sb soak. The XRD peak fitting of the spectrum shows there is less As in the GaAsSb in the superlattice. The surface of these structures also shows the roughness seen previously with the Sb soak grown structures shown in Figure 7.5 (a) and (b) for wafers with 100 and 50 periods of superlattice, respectively.

The XRD, for wafers grown without Sb soak but with a higher Sb flux, in Figure 7.4 (bottom graph) shows narrow satellite peaks suggesting an improved quality of the superlattice in the wafers with 50 periods of superlattice (SF1625) and 100 periods of superlattice (SF1627). A higher Sb flow was supplied for the wafer SF1625 (shown as red line) to achieve high Sb composition. 0^{th} peak shift confirms the increased Sb composition. The surface of the wafers is also smoother as seen in Figure 7.5 (c) and (d).

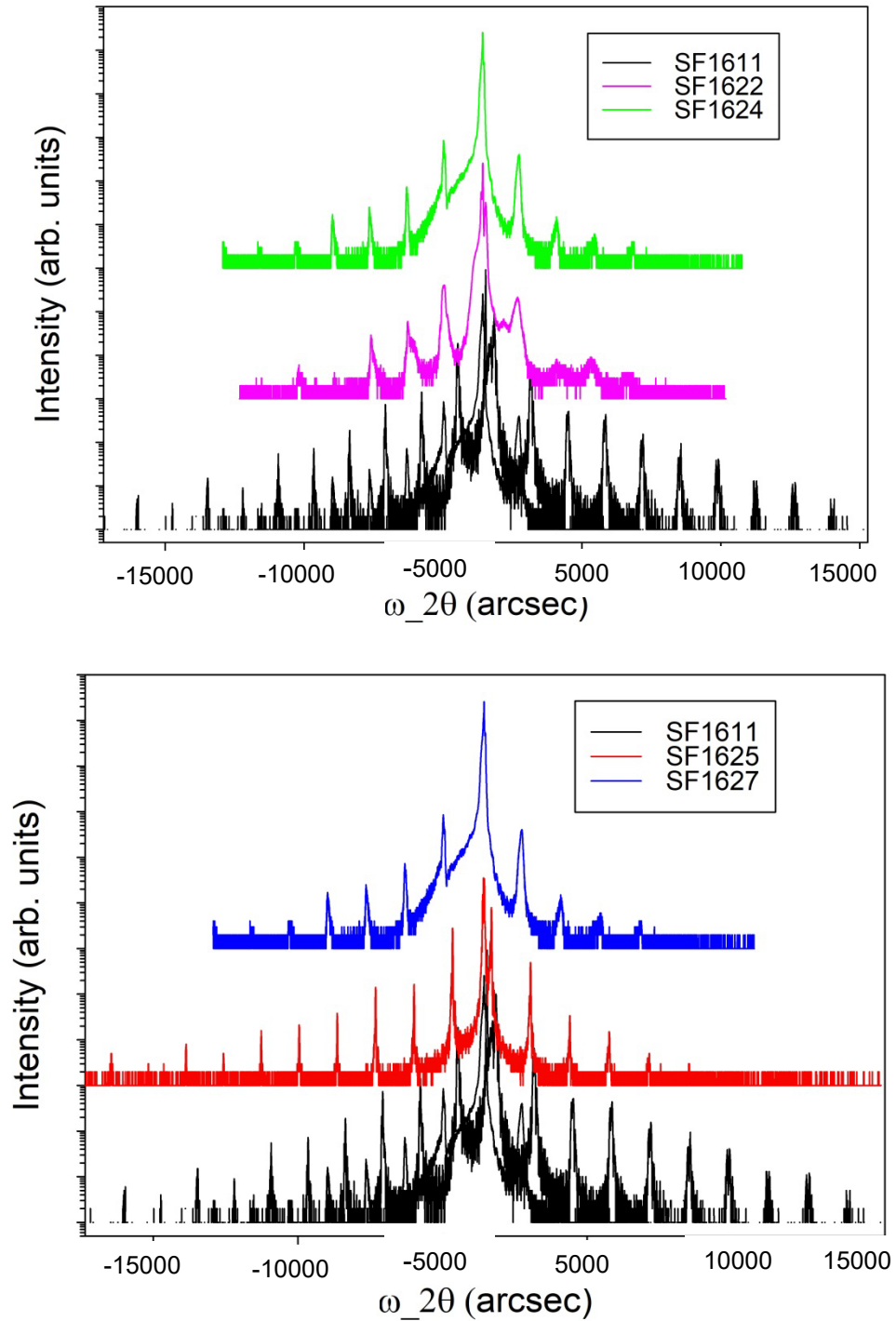


Figure 7.4: Top: The XRD spectrum for 15 ML InAs/16 ML GaAsSb structures, wafer SF1622 grown with Sb soak, and with 50 period repeats (pink) and wafer SF1624 100 period repeats (green). Bottom: The XRD spectrum for wafers grown without Sb soak but with increased Sb flux, wafer SF1625 with 50 periods (red) and wafer SF1627 with 100 periods (blue).

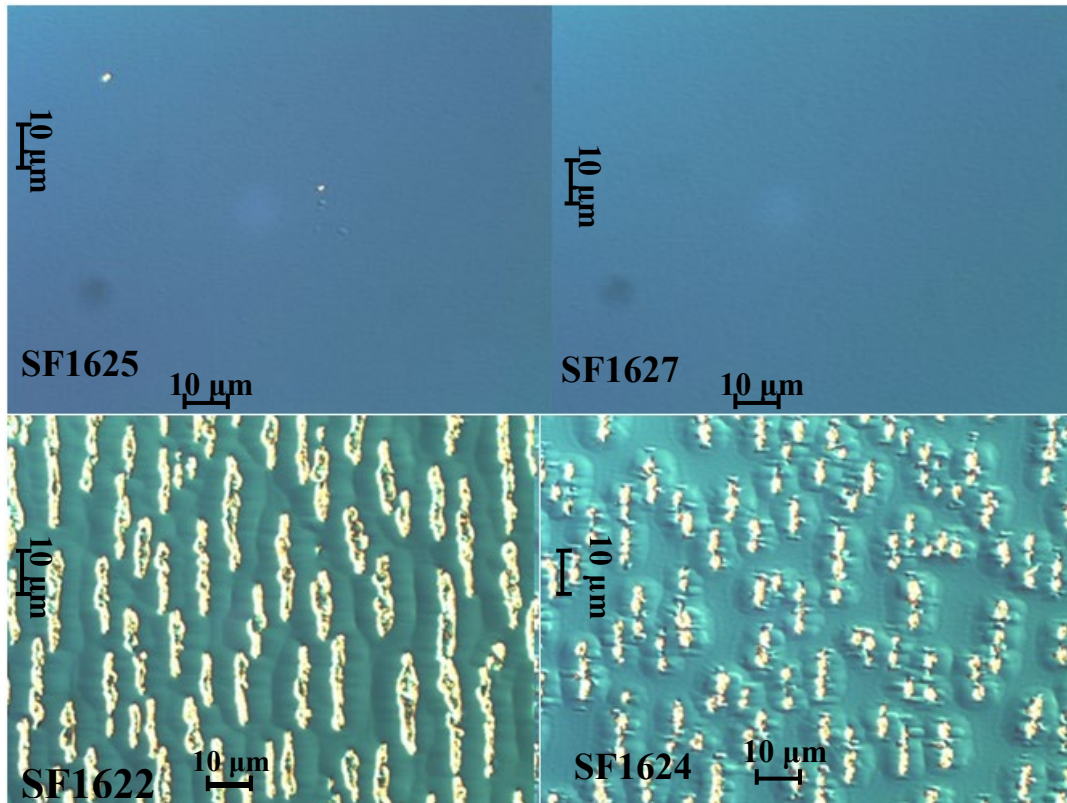


Figure 7.5: Nomarski microscopy (50x magnification) for 4 structures in Figure 7.4 c and d wafers are the green and pink XRD spectrums for the wafers SF1622 and SF1624 grown with and Sb soak and SF1625 and SF1627 (the red and blue lines in Figure 7.4) with no Sb soak respectively.

7.3 XRD simulations of wafer SF1625

XRD simulations on the wafer were carried out to confirm the structure of the superlattice inside the wafer, using Sergey Setepanov's free X-ray server [3,4]. The XRD simulations suggest there is some lattice mismatch in the superlattice part of the structure, the error in the MBE machine used to grow this wafer is 0.05 %.

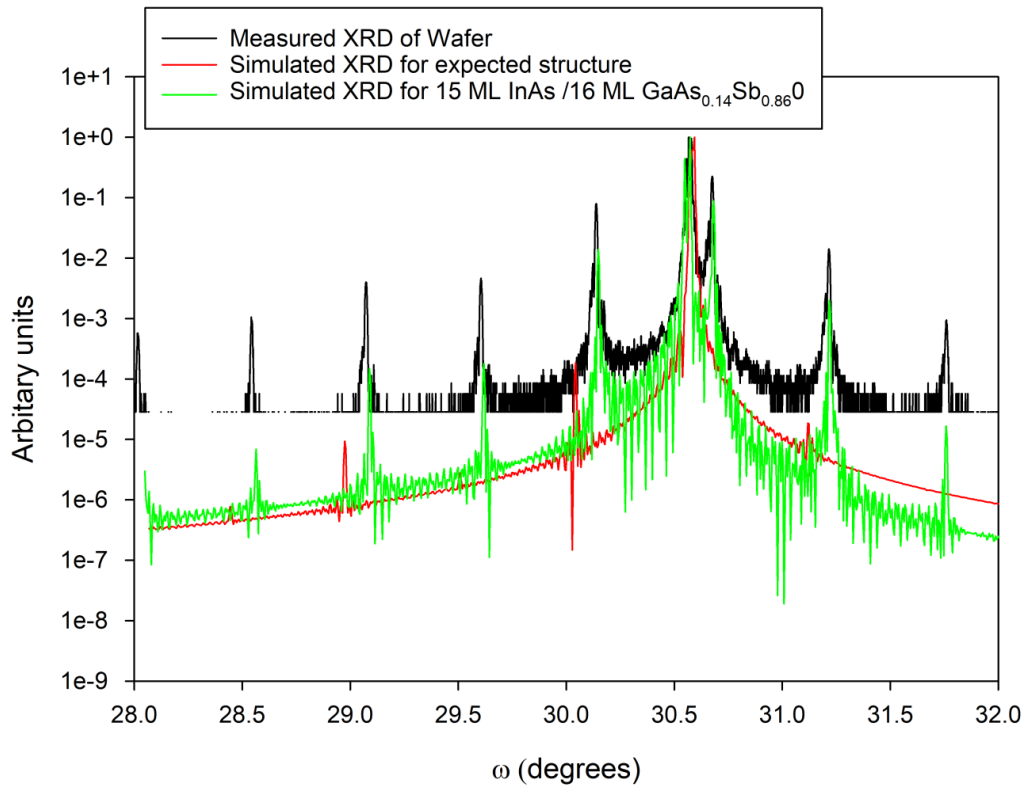


Figure 7.6: The measured XRD data for wafer SF1625, black, plotted against the simulated XRD data for the structure in SF1625 (15 ML InAs/16 ML GaAs_{0.09}Sb_{0.91}), red. The green line shows the fitted XRD for the measured XRD. The fitted data is for a 15 ML InAs/16 ML GaAs_{0.14}Sb_{0.86} structure.

The results in Figure 7.12 suggest a superlattice of 15 ML InAs/16 ML GaAs_{0.14}Sb_{0.86} was grown instead of the 15 ML InAs/16 ML GaAs_{0.09}Sb_{0.91} expected. The difference in the GaAsSb alloy Sb percentage causes lattice mismatch in the superlattice introducing strain into the superlattice. The new superlattice has a cutoff wavelength of 10.2 μm this is 0.7 μm longer than the original design. The strained structure would still respond in the LWIR which is what is shown by the blackbody measurements.

7.3.1 Fabrication of wafer SF1625

SF1625 (with 50 periods of superlattice) was fabricated using the standard procedure described in section 3.4. First, 20 nm/220 nm Ti/Au contacts were deposited by thermal evaporation. Then the sample was wet etched to a depth of 1250 nm with an etch solution of Phosphoric acid: Citric acid: H₂O₂: Deionised water (1:1:4:16) which left clean surfaces as can be seen in Figure 7.6.

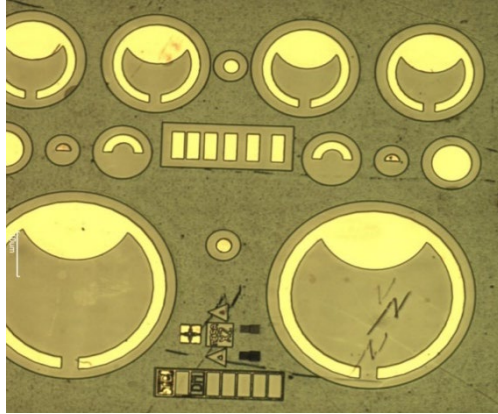


Figure 7.7: Image of wafer SF1625 after being etched for a depth of 1250 nm

7.4 *Low Temperature current voltage measurements*

Several fabrication runs were completed in an effort to improve the quality of the photodiode. The current density of each fabrication run was measured in a Janis probe station. This has the benefit of enabling low temperature current density measurements without the need to package the sample, which can damage the sample.

The first fabrication campaign used the procedures described in section 3.4. The phosphoric and citric acids combination was used for wet etching. The current density voltage results are shown in Figure 7.7.

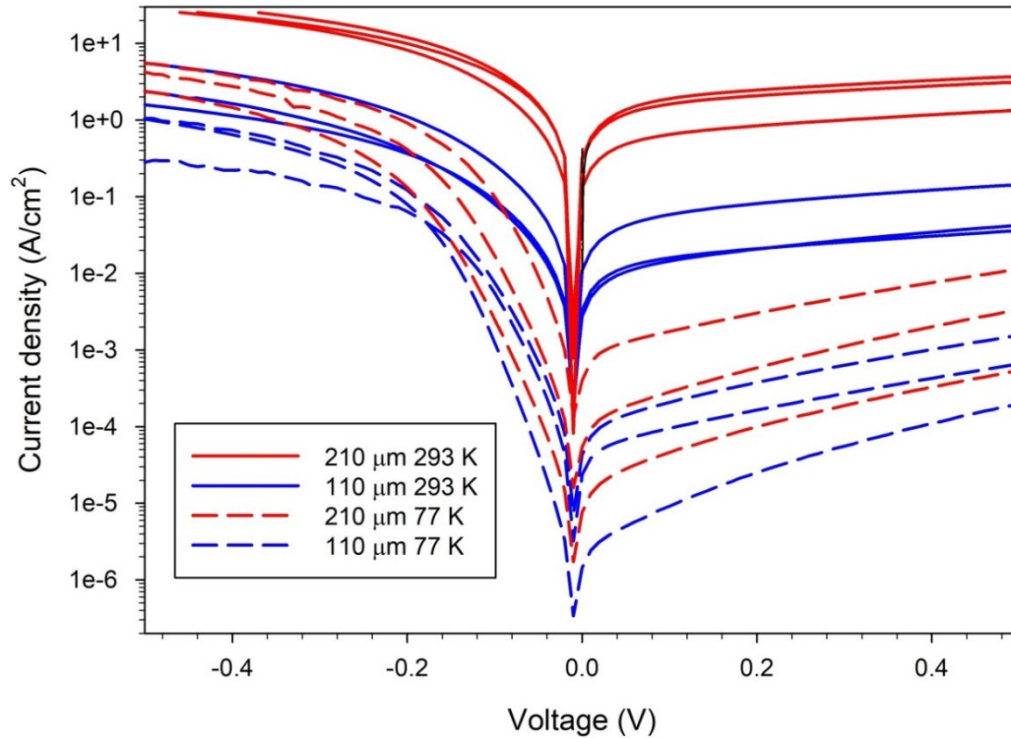


Figure 7.8: The current density against voltage plot for 15 ML InAs/16ML GaAsSb sample standard fabrication procedures, two different sized devices (radius 210 μm and 110 μm) at 77K (dashed lines) and 293 K (solid lines)

The results, from devices with radius of 210 and 110 μm , show some saturation of current density in the forward and the reverse bias which is especially clear at 77 K. The forward bias for both sizes at 77 K stays below $1.1 \times 10^{-2} \text{ Acm}^{-2}$ whereas the reverse bias current density rises to 5.8 Acm^{-2} . Though, as expected the large devices have high current density at both temperatures, the results do not show clear scaling with device area or with temperature. At 77 K with the current density of both sizes are spread across two orders of magnitude. There appears to be some current blocking mechanisms that prevent the forward current from increasing. The lower doping concentration of the top p layer of the wafer could have prevented the P contacts being ohmic. Non-ohmic contacts on the device can contribute to the current blocking indicated by the results.

To improve the dark current density in the second fabrication campaign the top 100 nm of the wafer was etched away before depositing gold contacts.

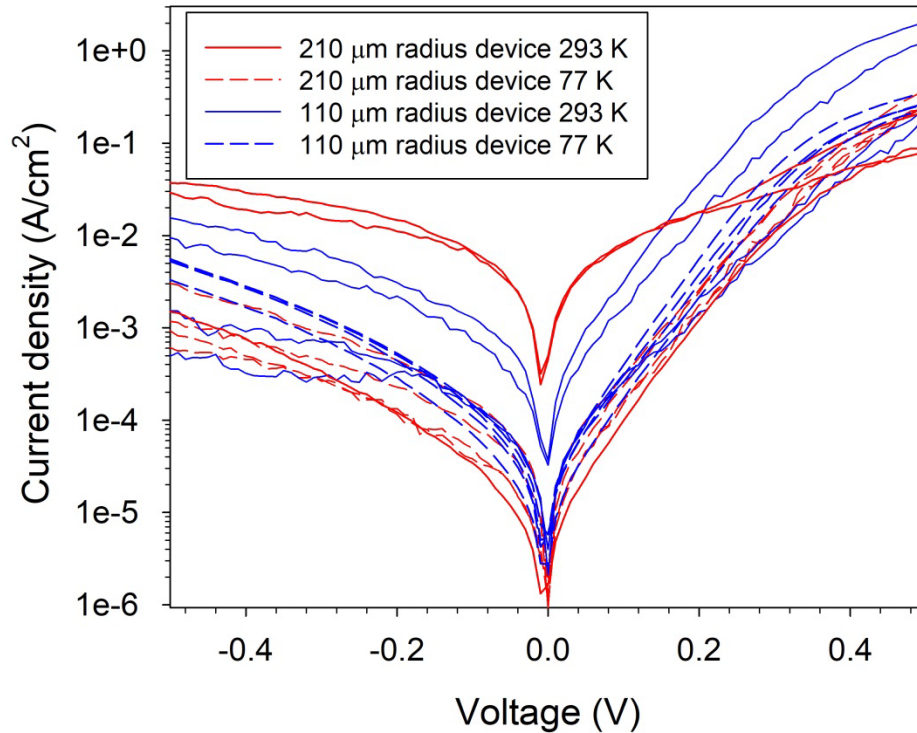


Figure 7.9: The current density against voltage plot for 15 ML InAs/16ML GaAsSb sample, two different sized devices (radius 210 μm and 110 μm) at 77 K (dashed lines) and 293 K (solid lines), top 100 nm of wafer etched off sample etched 50 nm into n-region.

The results in Figure 7.8 show improved current densities of approximately $2 \times 10^{-6} \text{ Acm}^{-2}$ for the two devices sizes at 0 V at 77 K. This current density at 0 V is similar to the values in campaign 1 but with improved bulk diode behaviour. This value of current density is in the same order of magnitude as those reported [1] at 77 K. The devices also show diode behaviour, with the current density in the forward bias increasing with bias. As the structure has a small bandgap diode behaviour (due to high dark current) is not expected at room temperature. However the smaller device appears to show current rectifying behaviour at room temperature. The devices are also mostly grouped by size which indicates close to bulk dark current behaviour.

In the forward bias of a 210 μm radius device, the current density at 0.2 V reduces from $2 \times 10^{-4} \text{ Acm}^{-2}$ for to $8 \times 10^{-3} \text{ Acm}^{-2}$. This suggests the removal of the top GaAsSb has helped to remove the current blocking behaviour in the forward bias that was observed in the first fabrication campaign. Packaging of the devices was attempted. Unfortunately, only one device was successfully packaged from batch of devices. It is possible that the etching of the top GaAsSb layer produces a poorer surface that causes the adhesion of the Ti/Au contact to be poor.

7.5 Blackbody emitter photoresponse

Selected devices from fabrication campaign 2 were packaged and cooled to 77 K and then exposed to a Blackbody source at a temperature of 1000 °C. Bandpass filters for several wavelength ranges were placed in front of the blackbody source, one at a time, to measure the change in the voltage on a lock-in amplifier. These values were then used to calculate the photocurrent of the device in each wavelength range. The range of wavelength the bandpass filters transmitted is depicted in Figure 3.5 in chapter 3.

Results in Figure 7.10 show the sample can respond to a wide range of wavelengths peaking at the LWIR with the bandpass filter 9-11 μm . From this peak it can be inferred that the strongest transmission happens in this range of wavelengths. The simulations for a 15 ML InAs/16 ML GaAsSb superlattice predicted a cutoff wavelength at 77 K of 9.5 μm . Though, as the signal at the cutoff wavelength would be weak, it would be expected that the strongest photocurrent would be seen when using the 7.3-9.45 μm filter. The photocurrent for the VLWIR filter is higher than expected, as most of the light passing through the filter has a smaller energy than E_g of the sample. However, this signal is also contributed to by blackbody radiation from the filter at room temperature, artificially boosting the photocurrent.

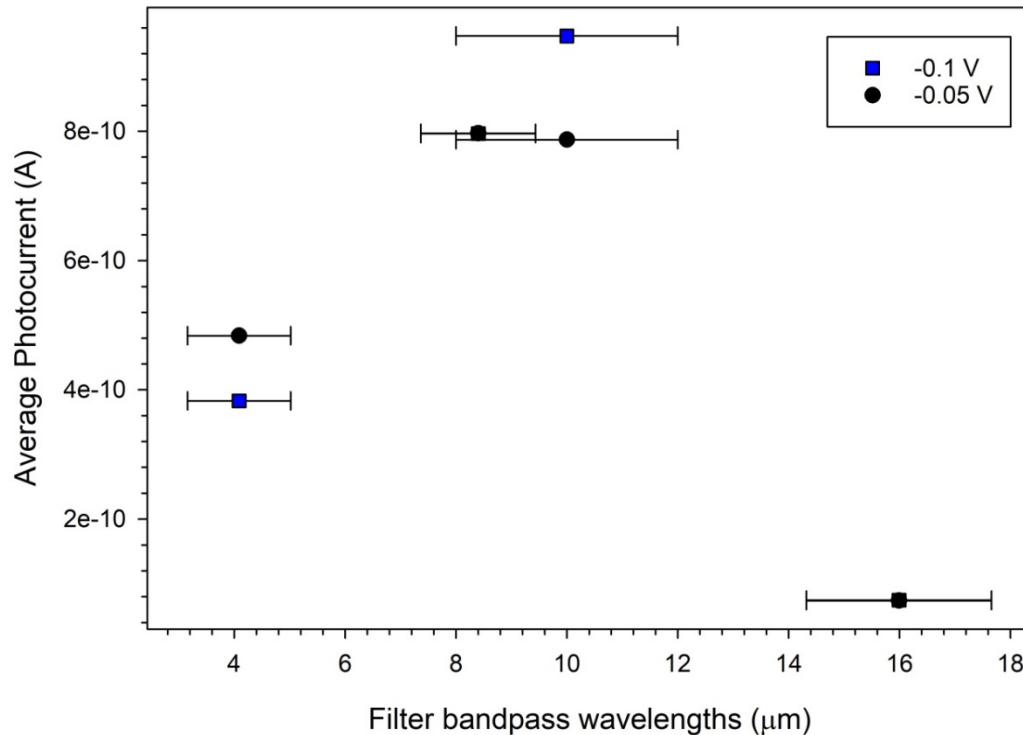


Figure 7.10: The photocurrent of 15 ML InAs/16 ML GaAsSb sample at 77 K exposed to blackbody at 1000 °C with bandpass filters at -0.03 V and -0.5 V. The error bars indicated the wavelengths the filter passes.

Three sets of results were taken over 2 days a week apart. As there is no way to gradually cool down the device in the dewar, and results were similar on the different measurement days, the device has some resistance to thermal degradation. The photoresponse of the photodiode shows the peak response for the 9-11 μm bandpass filter. This is not expected in the nominal design which is expected to have a cutoff wavelength of 9.5 μm at 77K. The wavefunctions of the nominal design are shown in Figure 7.11. The cutoff wavelength, given by the transition between E1 and HH1, indicates lack of absorption at wavelengths beyond 9.5 μm . Typically absorption coefficient decays significantly as the cutoff wavelength is approached, causing photocurrent low at those wavelengths. A structure with cutoff wavelength of 9.5 μm is unlikely to produce the highest response in the 9-11 μm , as measured. There are two possible contributions that could explain the higher response in the 9-11 μm band. From the XRD measurements in section 7.3, it is possible that the GaAsSb has a different composition that leads to a longer cutoff wavelength of 10.2 μm . In addition to this, a room temperature object will produce radiation with a peak at the wavelength of ~ 9.5 μm . Therefore it is possible that the detector has a longer cutoff wavelength and has reasonable background induced photocurrent.

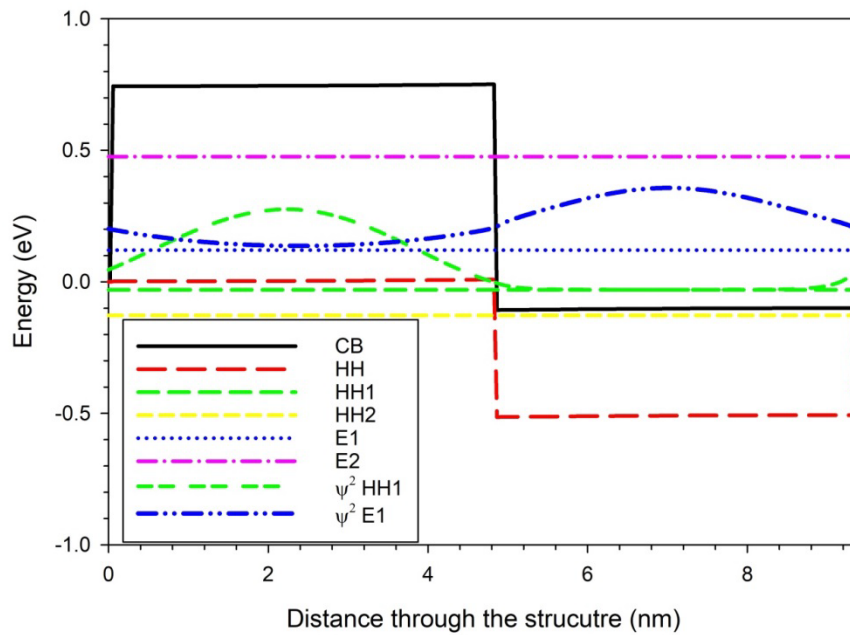


Figure 7.11: The energy level diagram of the 15 ML InAs/16 ML GaAsSb superlattice

To estimate of the quantum efficiency the following approach is taken, because the typical way measure the quantum efficiency was not available. Usually the spectral response of the device would be detected using an FTIR spectrometer and the quantum efficiency would be calculated using responsivity equation below,

$$R(\lambda) = \frac{\eta q}{hc}$$

(3.15 repeated)

where η is the quantum efficiency of the photodiode at wavelength λ . However, as the signal was too weak for the responsivity to be measured by a FTIR spectrometer, it was assumed that the quantum efficiency is constant at all the wavelengths of the bandpass filter. Then the quantum efficiency can be calculated using equation 3.14 repeated below.

$$i_{ph} = \int_{\lambda_1}^{\lambda_2} R(\lambda)P(\lambda).d\lambda$$

(3.14 repeated)

where $P(\lambda)$ is the power the blackbody is emitting at a certain wavelength. The assumption causes the responsivity term $R(\lambda)$ to become a constant. Therefore, using the measured photocurrent (i_{ph}) and integrating $P(\lambda)$ across the wavelengths covered by the bandpass filters the quantum efficiency can be calculated.

Using this method quantum efficiency for the device with each of the filters is shown in Table 7.2. Results show low values of quantum efficiency, which is not a surprise given the difficulties in obtaining the spectral response using the FTIR spectrometer.

The device has the highest quantum efficiency in the LWIR. To investigate whether room temperature blackbody radiation is the main source of the photocurrent detected, an optical chopper was placed in front of the device and the photocurrent was calculated for the signal when the blackbody emitter was switched on and switched off.

The quantum efficiency in the VLWIR is higher than would be expected. The larger value could be explained by LWIR signals, originating from room temperature blackbody radiation, reflected by the VLWIR filter. Overall the quantum efficiency of the sample is low, literature regularly reports 30 % efficiency [5,6], and suggesting fabrication of the sample still needs to be improved. The low quantum efficiency, 3 % at the target wavelengths 9-11 μm , could be due to several reasons, including the low wavefunction overlap of the samples, surface roughness and the lack of anti-reflection coating. As previously simulated in chapter 4, this InAs/GaAs_{0.09}Sb_{0.91} superlattice system has a low wavefunction overlap and low absorption, relative to the more conventional InAs/InGaSb superlattice. A simulated InAs/GaAs_{0.09}Sb_{0.91} superlattice with a cut-off wavelength of 7.63 μm has a cut-off wavelength of 8.3 %, this low wavefunction overlap directly effects the absorption of the sample as stated in chapter 1. Due to the low doping in the top layer, the top 100 nm of the sample needed to be etched off before fabrication could begin. This etch resulted in an increased surface roughness, which will increase light scattering at the sample surface and also reduced contact adhesion (reducing the bonding yield to 1 device). The lack of anti-reflection coating will further limit the absorption. All of the above will limit absorption and thus reduce the measured quantum efficiency.

Therefore to enhance the quantum efficiency of InAs/GaAsSb higher number of superlattice repeats and incorporation of absorption enhancement features. This could be an optical cavity using mirrors, crystal geometry or a large difference in refractive index to reflect light back into the absorption region allowing the light multiple passes through the structure before leaving.

A report from a recent paper [7] suggested that it was possible to achieve a quantum efficiency of 65 % at 8.9 μm at 77 K using 800 periods of 22 ML InAs/19 ML GaAsSb for the absorption region. This was attributed the use of an optical cavity. A highly doped InAs Buffer layer was grown between the superlattice and the substrate. The large difference in refractive index between the InAs and the superlattice caused the light to be reflected, and pass through the absorption region multiple times, increasing the photocurrent caused by the light.

Table 7.2: The estimated the quantum efficiency that based on measured photocurrent

Filter range (μm)	Calculated Quantum efficiency (%)	Average photocurrent measured (nA)
3.85-3.94	0.12	0.306
7.37-9.44	0.9	0.719
9.0-11.05	3	0.870
15.14- 16.81	0.9	0.152

7.6 Conclusion

A wafer consisting of a PIN design with a GaAsSb p-region, a 50 repeat of 15 ML InAs/16 ML GaAsSb superlattices in the i-region and an InAs n-region. Theoretical simulations predicted this superlattice structure which has a cutoff wavelength of 9.5 μm at 77 K. The sample was etched to a depth of 1250 nm with an etch solution of Phosphoric acid: Citric acid: H_2O_2 : Deionised water (1:1:4:16).

Dark current measurements suggested that diode rectifying behaviour was observed. The dark current at 0 V and 77 K is comparable to that published in the literature. Photocurrent measurements showed the sample had a photoresponse to a wide range of wavelengths

from 3 μm to 15 μm . The results peak at 9-11 μm , suggesting the cutoff wavelength of this sample is longer than 9.5 μm . The XRD fitting simulation suggested a strained 15 ML InAs/16 ML GaAs_{0.14}Sb_{0.86} superlattice with a cutoff wavelength of 10.2 μm has been grown rather than the structure expected. Response from the VLWIR was not expected and was interpreted to be room temperature radiation that is reflected by the VLWIR filter. In summary growth and fabrication of a LWIR InAs/GaAsSb superlattice detector was demonstrated. However the deduced quantum efficiency is low, suggesting that an increased absorption region and absorption enhancement features will need to be incorporated.

References

- ¹ R.chavallier, A. Haddi, and M. Razeghi, "Dark current reduction in microjunction-based double electron barrier type-II InAs/InAsSb superlattice long-wavelength infrared photodetectors," *Scientific Reports*, vol. 7, p. 12617, 2017
- ² F. Wang, J. Chen, Z. Xu, Y. Zhou, and L. He, "InAs-based InAs/GaAsSb type-II superlattices: Growth and characterization," *Journal of Crystal Growth*, vol. 416, pp. 130-133, 2015/04/15/ 2015.
- ³ X-Ray Server URL: <https://x-server.gmca.aps.anl.gov>
- ⁴ S. Stepanov, "X-ray server: an online resource for simulations of X-ray diffraction and scattering". *Proceedings SPIE* vol.5536, pp.16-26, (2004).
- ⁵ F. Wang, J. Chen, Z. Xu, Y. Zhou, and L. He, "InAs-based InAs/GaAsSb type-II superlattices: Growth and characterization," *J. Cryst. Growth*, vol. 416, pp. 130-133, 2015/04/15/ 2015.
- ⁶ M. Huang, J. Chen, J. Xu, F. Wang, Z. Xu, and L. He, "ICP etching for InAs-based InAs/GaAsSb superlattice long wavelength infrared detectors," *Infrared Phys Technol*, vol. 90, pp. 110-114, 2018/05/01/ 2018.
- ⁷ M.Huang, J. Chen, Y. Zhou, Z. Xu, and L.He, "light-harvesting for high quantum efficiency in InAs-based InAs/ GaAsSb type-II superlattices long wavelength infrared photodiodes," *App Phys Lett*, vol. 114, p. 141102, 2019.

8. Conclusions and future plans

Type II superlattices (T2SL) are a promising alternative to mercury cadmium telluride for LWIR and VLWIR photodiodes. A lattice matched T2SL superlattice can be grown with fewer defects, improving the crystal structure, which improves the overall quality of the photodiodes. However, growth and fabrication of superlattice photodiodes can be expensive. Therefore, modelling the material system, before growth, to ascertain the best structure for the desired wavelengths is beneficial. From the simulations in this thesis, it can be concluded that the nextnano++ software is an effective tool to design and model T2SL photodiodes.

8.1. Conclusions

8.1.1. Cutoff simulations

Simulations of cutoff wavelengths for InAs/GaAsSb superlattices, showed nextnano++ could accurately simulate the bandgap and cutoff wavelengths (λ_c) of InAs/GaAsSb T2SLs. Simulated results agree with reported experimental results. A range of λ_c from 5 μm to 18 μm was achieved using wells and barrier thicknesses ranging from 7 ML to 22 ML. The simulations showed VLWIR was achievable with InAs wells >16 ML and barriers >12 ML, and the LWIR was achievable with wells >12 ML. Investigations into the dependence of the λ_c on the thickness of the well and barrier materials showed that the well has a significantly larger effect on the λ_c of the superlattice. An increase of 13 ML in the well thickness for a structure with a barrier thickness of 7 ML increased the λ_c from 4.7 to 17 μm . Whereas, for a superlattice with a set well thickness of 7 ML, a barrier thickness increase of 13 ML λ_c only increases by 1.1 μm . This is seen consistently with superlattices with wells and barrier thicknesses ranging from 7 ML to 20 ML. It can be concluded InAs (well) thickness has a larger effect on the λ_c of the superlattice.

8.1.2. Absorption coefficient simulations

Nextnano++ was able to reproduce reported experimental results. Optical simulations of InAs/GaAsSb T2SLs showed that more symmetrical superlattice designs had higher absorption coefficients. 16 ML InAs/10 ML GaAsSb which has a cutoff wavelength of 10.3 μm , yielded a higher absorption coefficient, 177.94 cm^{-1} , compared to 20 ML InAs/7 ML GaAsSb which has an absorption coefficient of 31.57 cm^{-1} . A similar result was seen for designs with λ_c 13 μm , 17 ML InAs/16 ML GaAsSb yields a 170.2 cm^{-1} higher absorption coefficient than 26 ML InAs/7 ML GaAsSb, 200.4 to 30.2 cm^{-1} . From these simulations it can be concluded for superlattice designs with the same λ_c , more symmetrical structures are favourable due to higher absorption

coefficients. This higher absorption coefficient was attributed to more symmetrical structures having a larger overlap of the first electron energy level and highest hole energy level wavefunctions. However, it is noted that the absorption coefficient is lower than that in the strained InAs/GaSb superlattices. Therefore thicker InAs/GaAsSb, which should be possible because of the lattice matched layers, together with absorption enhancement features such as multi-pass absorption, will be needed to achieve high quantum efficiency.

8.1.3. Temperature dependence of bandgap and absorption simulations

The temperature dependence of E_g and absorption coefficient of InAs/GaAsSb simulations was investigated. Simulations into whether the barrier or well material had a stronger dependence on temperature, showed InAs well thickness had a larger dependence on temperature. Though this was attributed partly to the larger effect of InAs thickness on E_g . The results also show that structures with longer cutoff wavelength exhibit larger change in bandgap when temperature changes.

The results for structures with the same cutoff wavelength at 77 K tracked in a similar way with temperature. This suggests the structure of the superlattice is not a major factor in the temperature dependence of E_g . The results also show that structures with longer cutoff wavelength exhibit larger change in bandgap when temperature changes. Optical absorption of the same structures showed that the structures with close to symmetrical superlattice periods have larger absorption coefficients at all temperatures. It can be concluded that a more symmetrical is more beneficial at all temperatures.

8.1.4. Current-density

A series of current density simulations were performed for InAs/GaAsSb photodiodes. The nextnano++ simulations were able to reproduce reported dark current density values. Simulations of different period superlattice PIN devices suggested that InAs thickness has the strongest effect on the current-density of the photodiode. However, this was credited to the larger effect InAs thickness has on the E_g .

From simulations of superlattice periods with similar cutoff wavelengths, it was concluded that there was a weak dependence on the structure of the superlattice, with no significant difference in the current densities. The close to symmetrical structures have a small increase in current density but this is not large enough to be a consideration when choosing a superlattice structure.

Based on existing material parameters and generation-recombination parameters, simulations also suggested that VLWIR structures will need to operate at temperature below 77 K to achieve low dark current. The generation-recombination was shown to be a dominant dark current mechanism.

This suggests that reducing the generation-recombination current is necessary to achieve operation at 77 K. This will require improved carrier lifetime through improved growth, or use of photodiodes with barriers, such as an nBn structure, where the generation-recombination component is reduced due to the wider bandgap used in the depletion region

8.2. Future Plans

The main focus of the future plans for this work would be on adjusting the designs to improve the absorption coefficients and the current density.

8.2.1. Recombination mechanism parameters

As seen in Figure 6.17 the recombination mechanisms make a significant contribution to the total current density simulations. However, simulations showed that the current parameters were based on fitting to a single set of reported results in InAs/GaAsSb. More data across different designs will be needed to verify how the parameters will change.

8.2.2. Extended structure size

One disadvantage to InAs/GaAsSb photodiodes the simulations indicated is the low absorption coefficient values. The absorption coefficient (α) could be improved by extending the thickness of the device; this would reflect the trend in published results to use thicker devices. Increasing the device thickness would also increase the quantum efficiency (η) as the equation dictates where the L is the thickness of the device.

$$\eta = 1 - e^{-\alpha(\lambda)L}$$

8.2.3. Including barriers

One common way used to reduce the current-density of a photodiode is to include barriers in the p and n regions to block carrier movement in one or both directions. A disadvantage to barrier structures is large barriers could absorb light in the p and n region, which would not be of the operating wavelength and contribute to the dark current of the structure. As shown in Figure 8.1 adding a bulk material region decreases the current density especially at low bias. The step in current density for the dual barrier structure could be due to tunnelling current. The large step in the current-density could also be due to the bias bending the conduction and valence bands causing the barriers to become easier to overcome. This would be a promising area for further study as reducing the dark current can improve the signal to noise ratio of the device.

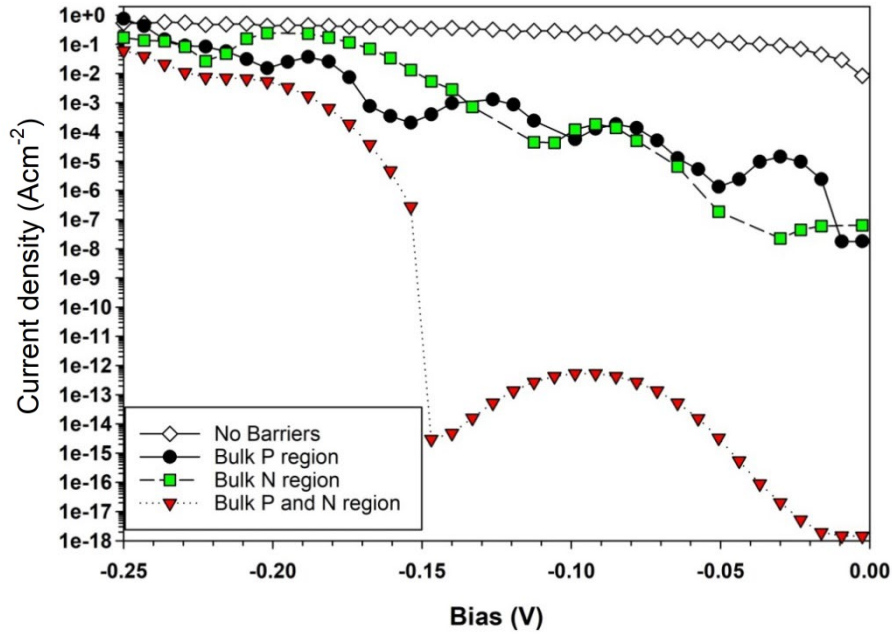


Figure 8.1: 20 ML InAs/9 ML GaAsSb PIN ($\lambda_c = 10 \mu\text{m}$) structure with bulk material regions to act as barriers to the superlattice at 150 K

8.2.4. Including small amount of strain

While absorption simulations showed that more symmetrical superlattice period designs are favourable due to higher absorption coefficients, the absorption values are still lower than strained T2SL superlattices such as InAs/GaSb. InAs/GaSb T2SLs are strained and have a broken T2SL band structure whereas InAs/GaAsSb has a staggered T2SL band structure. So a small amount of strain could be introduced into the structure to improve the absorption coefficients. Strain changes the positions of the band edges, causing smaller well and barrier structures to achieve the same λ_c as larger lattice matched ones. The smaller wells and barriers mean the wavefunctions overlap will be greater, which causes the likelihood of a transition to increase, increasing the absorption coefficient. The strain on the materials also changes the position of the energy levels, compressive strain increases the E_g of the material and tensile strain decreases the E_g . Strained structures also have the benefit of the strain causing the HH and LH to separate, reducing Auger contributions to dark current.

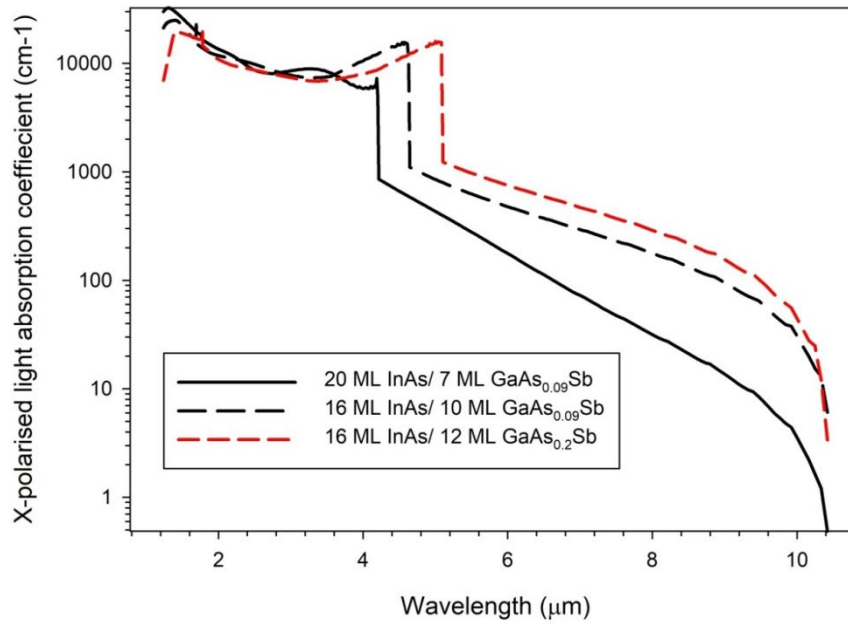
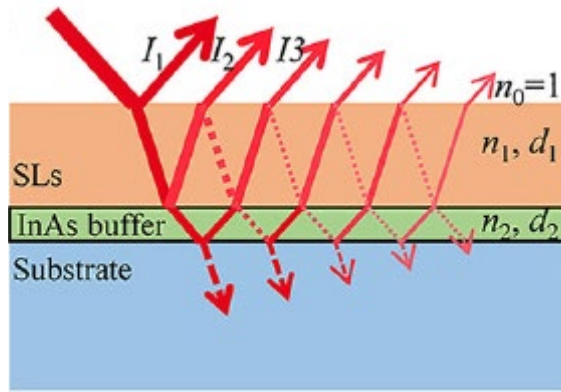


Figure 8.2 shows structures with the same cutoff wavelength at 77 K, the 20 ML InAs/7 ML GaAs_{0.09}Sb_{0.91}, 16 ML InAs/10 ML GaAs_{0.09}Sb_{0.91} and 16 ML InAs/12 ML GaAs_{0.2}Sb_{0.8}. The lattice matched superlattices both have lower absorption coefficient than the strained superlattice (16 ML InAs/12 ML GaAs_{0.2}Sb_{0.8}). This implies further investigation could improve the absorption coefficient results.

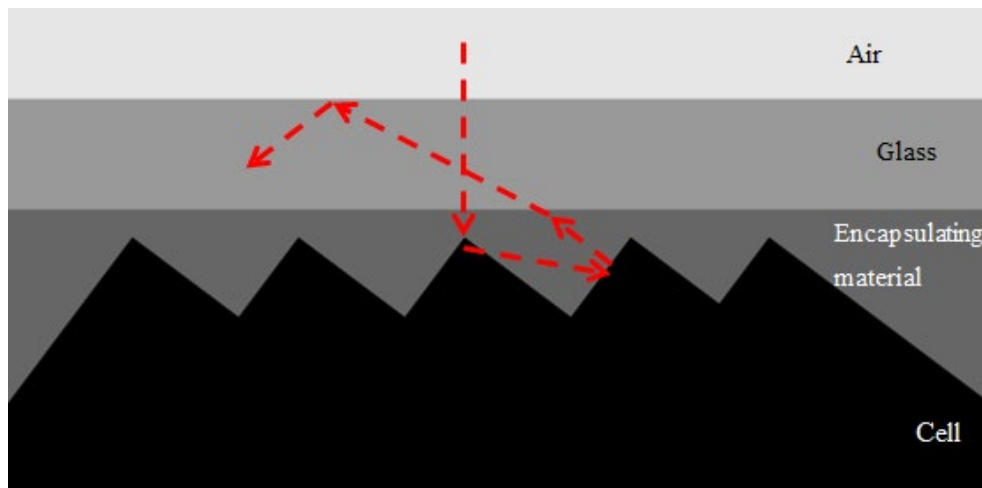
8.2.5. Resonant cavity structures

Another method for improving absorption is by passing the light through the sample multiple times. This has been achieved in InAs/GaAsSb superlattices for a photodiodes in the LWIR [1]. In [1] a LWIR resonant cavity photodiode achieved a quantum efficiency of 65 % at 8.9 μm at 77 K. The high quantum efficiency was achieved by a PBIBN structure with a 22 ML InAs/19 ML GaAsSb absorption region and with hole and electron barriers. The resonant cavity of the structure uses a large difference in refractive index to reflect the light back into the absorption region shown in Figure 8.3. The superlattice refractive index was estimated to be $n_1= 3.5$, the InAs buffer refractive index (n_2) is estimated to be between 2 and 3.5, though based on literature InAs refractive index is likely to be closer to $n_2=3.5$ [2]. The InAs buffer was highly n-doped to achieve reflection, this allowed light to travel through the absorption region several times increasing the quantum efficiency.



The same resonant cavity method was utilised in [3] for a LWIR InAs/InAs_{0.70}Sb_{0.30} superlattice photodiode. The device had a quantum efficiency of 14 % which is lower than other LWIR photodiodes reported. However the calculated quantum efficiency of the superlattice structure without the resonant cavity design is 3.7 %, suggesting resonant cavity designs could improve quantum efficiency by as much as 26 %.

Solar cells also use reflection to increase quantum efficiency and absorption. This is achieved by using pyramid geometry to encourage reflections [4]. The path the light travels is demonstrated in Figure 8.4.



References

¹ M.Huang, J. Chen, Y. Zhou, Z. Xu, and L.He, “light-harvesting for high quantum efficiency in InAs-based InAs/ GaAsSb type-II superlattices long wavelength infrared photodiodes,” *App Phys Lett*, vol. 114, p. 141102, 2019.

² S. Adachi, “Optical dispersion relations for GaP, GaAs, GaSb, InP, InAs, InSb, Al_xGa_{1-x}As, and In_{1-x}Ga_xAs_yP_{1-y},” *J. Appl. Phys.*, vol. 66, no. 12, pp. 6030–6040, 1989, doi: 10.1063/1.343580.

³ V. Letka, A. P. Craig, A. Bainbridge, and A. R. J. Marshall, “A superlattice-based resonant cavity-enhanced photodetector operating in the long-wavelength infrared,” *Appl. Phys. Lett.*, vol. 117, no. 7, p. 73503, 2020,

⁴ S. C. Baker-Finch and K. R. McIntosh, “Reflection of normally incident light from silicon solar cells with pyramidal texture,” *Prog. Photovolt.*, vol. 19, no. 4, pp. 406–416, 2011, doi: 10.1002/pip.1050.

Appendix A- The parameters in nextnano++ simulations

Below is a table of the key properties used in the simulations the parameters in bold are the parameters changed from the default database to the values from Vurgaftman parameter paper.

Parameters	InAs	GaAs	GaSb	GaAsSb
Lattice constant (at 300 K)	6.0583	5.65325	6.0959	
Bandgap	0.417	0.067	0.812	1.43
Electron effective mass	4.79159	-2.88	-2.25165	
Kane's momentum matrix element (eV)	21.5	28.8	27.0	
Inversion symmetry parameter	3.596	7.979	13.079	
L	15.695	2.74	-7.85	
M	-4.0	-3.86	-5.0	
N	-15.89	1.38	-10.656	
Kappa	1.129	-1.74	-1.044	
Valence band offset	1.390	1.346	1.777	-1.06
Mobility electrons (cm ² /Vs)	32500	8500	5300	
Mobility holes (cm ² /Vs)	510	800	1000	
SRH acceptors doping scattering time (s) and doping concentration (cm ⁻³)	1.0e-9 1.0e19	1.0e-9 1.0e19	1.0e-9 1.0e19	
SRH donors doping scattering time (s) and doping concentration (cm ⁻³)	1.0e-9 1.0e18	1.0e-9 1.0e18	1.0e-9 1.0e18	
Auger constants for Acceptors and Donors (cm ⁶ /s)	1.0e-31 1.0e-31	1.0e-30 1.0e-30	5.0e-30 5.0e-30	
Radiative (cm ⁶ /s)	7.5e-10	7.2e-10	1.0e-9	

Appendix B- The parameter script used in nextnano++ simulations

Below is the parameters for each material used in this thesis as they appear in the nextnano script,

A. InAs material parameters

```

binary_zb { #stating that the material is zinblende (cubic crystal structure)
name      = InAs
valence   = III_V

lattice_consts{a      = 6.0583          # units [Angstrom] lattice constant at 300 K
a_expansion = 2.74e-5          } # units Angstrom/K, The temperature dependent lattice
constants
dielectric_consts{
static_a = 15.15          # Landolt-Boernstein epsilon(0)
optical_a = 12.25        # Landolt-Boernstein epsilon(infinity) used in laser calulations

elastic_consts{
c11 = 83.29 c12 = 45.26 c44 = 39.59      } # units are GPa elastic constants
piezoelectric_consts{
e14 = -0.044      } # units C/m2
conduction_bands{ # material parameters at Gamma in conduction band
Gamma{
mass          = 0.026
bandgap       = 0.417      # units eV result at 0 K
bandgap_alpha = 0.276e-3   # units eV/K for temperature dependent bandgap alpha in
Varshni equation
bandgap_beta  = 93        # units K for temperature dependent bandgap beta in Varshni equation
defpot_absolute = -6.66   # units eV the absolute deformation potential of gamma conduction
band          g          = -14.9      # g factor (for Zeeman splitting in magnetic fields)
}
L{ # material parameters at L point in Brillouin zone in conduction band
mass_l        = 0.64
mass_t        = 0.05
bandgap       = 1.133
bandgap_alpha = 0.276e-3
bandgap_beta  = 93
defpot_absolute = -3.89
defpot_uniaxial = 11.35   # units eV the deformation potential of conduction band at L in
all directions
}
X{ # material parameters at x point in Brillouin zone in conduction band
mass_l        = 1.13
mass_t        = 0.16
bandgap       = 1.433      # at (0 K)
bandgap_alpha = 0.276e-3
bandgap_beta  = 93
defpot_absolute = -0.08    #
defpot_uniaxial = 3.7      #
}
}
valence_bands{# material parameters at gamma point in Brillouin zone in Valence band

```

```

bandoffset      = 1.390 #different definition in nn+ than elsewhere average energy of the three valence
band edges  $E_{v,av} = (E_{hh} + E_{lh} + E_{so}) / 3$ 
HH{ mass      = 0.41 g = -45.2 } # heavy hole mass
LH{ mass      = 0.026 g = -15.1 } # light hole mass
SO{ mass      = 0.14 }
defpot_absolute = -1.00      # units eV the deformation potential of valence band aveaged over a 3
bands
defpot_uniaxial_b = -1.8 defpot_uniaxial_d = -3.6
delta_SO        = 0.39      # split off energy units eV
}
kp_8_bands{
    S = -4.79159      # electron effective mass
    E_P = 21.5 #Kane's momentum matrix element unit eV
    B = 3.596 # inversion symmetry paparameter
        L = -15.695 M = -4.0 N = -15.895
    kappa = 1.129
}
}

mobility_constant{
    electrons{ mumax = 32500 exponent = 1.7 } #bulk electron phonon mobility units  $cm^2/Vs$  ,
electrons temperature dependence exponent
    holes{ mumax = 510 exponent = 2.3 } #same as above but for holes

    recombination{
        SRH{ tau_n = 1.0e-9 nref_n = 1.0e19 #units s, electrons no doping scattering time, electrons
doping concentration reference units  $cm^{-3}$ 
tau_p = 1.0e-9 nref_p = 1.0e18 #same as above for holes
        }
        Auger{ c_n = 1.0e-31 c_p = 1.0e-31 #  $cm^6/s$  auger constant for acceptors and donors
        }
        radiative{ c = 7.5e-10 #radiative constant units  $cm^6/s$ 
        }
    }
}
}

```

B. GaAs material parameters

```

binary_zb {
    name = GaAs
    valence = III_V

    lattice_consts{
        a = 5.65325
        a_expansion = 3.88e-5
    }

    dielectric_consts{
        static_a = 12.93
        optical_a = 10.89
    }

    elastic_consts{
        c11 = 122.1 c12 = 56.6 c44 = 60.0
    }

    piezoelectric_consts{
        e14 = -0.160
    }
}

```

```

conduction_bands{
  Gamma{
    mass      = 0.067
    bandgap   = 1.519
    bandgap_alpha = 0.5405e-3
    bandgap_beta  = 204
    defpot_absolute = -9.36
    g          = -0.30
  }
  L{
    mass_l     = 1.9
    mass_t     = 0.0754
    bandgap    = 1.815
    bandgap_alpha = 0.605e-3
    bandgap_beta  = 204
    defpot_absolute = -4.91
    defpot_uniaxial = 14.26
  }
  X{
    mass_l     = 1.3
    mass_t     = 0.23
    bandgap    = 1.981
    bandgap_alpha = 0.460e-3
    bandgap_beta  = 204
    defpot_absolute = -0.16
    defpot_uniaxial = 8.61
  }
}

valence_bands{
  bandoffset = 1.346
  HH{ mass = 0.51 g = -7.86 }
  LH{ mass = 0.082 g = -2.62 }
  SO{ mass = 0.172 }

  defpot_absolute = -1.21
  defpot_uniaxial_b = -2.0 defpot_uniaxial_d = -4.8
  delta_SO = 0.341
}

}

kp_8_bands{
S = -2.88
E_P = 28.8
B = 7.979
L = 2.73984 M = -3.86 N = 1.3798
Kappa -1.74
}

mobility_constant{
  electrons{ mumax = 8500 exponent = 2.2 }
  holes{ mumax = 800 exponent = 0.9 }
}

recombination{
  SRH{ tau_n = 1.0e-9 nref_n = 1.0e19
        tau_p = 1.0e-9 nref_p = 1.0e18
      }
  Auger{ c_n = 1.0e-30 c_p = 1.0e-30
        }
}

```

```

    radiative{ c = 7.2e-10
    }
  }
}

```

C. GaSb material parameters

```

binary_zb {
name   = GaSb
valence = III_V

lattice_consts{
  a      = 6.0959
  a_expansion = 4.72e-5
}

dielectric_consts{
  static_a = 15.69
  optical_a = 14.44
}

elastic_consts{
  c11 = 88.42  c12 = 40.26  c44 = 43.22
}

piezoelectric_consts{
  e14 = -0.172
}

conduction_bands{
  Gamma{
    mass      = 0.039
    bandgap    = 0.812
    bandgap_alpha  = 0.417e-3
    bandgap_beta   = 140
    defpot_absolute = -9.33
    g          = -9.2
  }
  L{
    mass_l      = 1.3
    mass_t      = 0.10
    bandgap     = 0.875
    bandgap_alpha  = 0.597e-3
    bandgap_beta   = 140
    defpot_absolute = -4.38
    defpot_uniaxial = 15.0
  }
  X{
    mass_l      = 1.51
    mass_t      = 0.22
    bandgap     = 1.141
    bandgap_alpha  = 0.475e-3
    bandgap_beta   = 94
    defpot_absolute = -0.20
    defpot_uniaxial = 6.46
  }
}
}

```

```

valence_bands{
  bandoffset = 1.777

  HH{ mass = 0.34 }
  LH{ mass = 0.0447 }
  SO{ mass = 0.12 }

  defpot_absolute = -1.32
  defpot_uniaxial_b = -2.0 defpot_uniaxial_d = -4.7

  delta_SO = 0.76
}

kp_8_bands{
  S = -2.25165
  E_P = 27.0
  B = 13.079
  L = -7.85 M = -5.0 N = -10.656
  kappa = -1.044
}
mobility_constant{
  electrons{ mumax = 5300 exponent = 1.9 }
  holes{ mumax = 1000 exponent = 1.2 }
}

recombination{
  SRH{ tau_n = 1.0e-9 nref_n = 1.0e19
        tau_p = 1.0e-9 nref_p = 1.0e18
    }
  Auger{ #c_n = 1.0e-31 c_p = 1.0e-31
          c_n = 5.0e-30 c_p = 5.0e-30
    }
  radiative{ #c = 8.0e-11
             c = 1.0e-9 # ?
    }
}
}

```

D. GaAsSb material parameters

```

ternary_zb {
  name = "GaAs(1-x)Sb(x)"
  valence = III_V
  binary_x = GaSb
  binary_1_x = GaAs

  conduction_bands{
    Gamma{ bandgap = 1.43 } # Vurgaftman1
    L { bandgap = 1.2 } # Vurgaftman1
    X { bandgap = 1.2 } # Vurgaftman1
  }

  valence_bands{
    bandoffset = -1.06
  }
}

```



```
mobility_constant{  
  electrons{ mumax = 0 }  
  holes      { mumax = 0 }  
}
```